Department of

Physics "Giuseppe Occhialini"

PhD program Physics and Astronomy   Cycle 33rd

Curriculum in Plasma Physics and Biophysics

Two-photon assisted direct laser writing of proteinaceous microarchitectures containing plasmonic nanoparticles; characterization and optimization

Surname: Zeynali   Name: Amirbahador

Registration number: 827258

Supervisor: Prof. Giuseppe Chirico

Co-tutor: Prof. Maddalena Collini

Coordinator: Prof. Marta Calvi

"Two-photon assisted direct laser writing of proteinaceous microarchitectures containing plasmonic nanoparticles; characterization and optimization"

Amirbahador Zeynali
PhD Thesis

Supervisor: Prof. Giuseppe Chirico

October 2020

Approved examiners:

     Prof. Niels B. Larsen, *Denmark Technical University (DTU)*

     Prof. Pietro Ferraro, *Institute of Applied Science & Intelligent Systems - CNR*

Approved final evaluation committee:

     Prof. Giulio Cerullo, *Politecnico di Milano*

     Prof. Paolo Radaelli, *Oxford University*

     Prof. Carla Andreani, *Università degli Studi di Roma Tor Vergata*

     Prof. Maria Farsari, *FORTH, Institute of electronic structure and laser*

Abstract

Metallic nanoparticles, due to their fascinating optical and electrochemical properties, attract the attention of different science and engineering research disciplines. Among these properties, the plasmonic photothermal effect is a notable and exclusive feature of noble-metal nanoparticles that, by today, are exploited through lots of research activities for various purposes, especially for biomedical applications. This optically-tunable phenomenon uniquely increases the flexibility of the optical response of host matrices, by allowing to induce highly localized temperature increases that can be triggered via simple external stimulation device like a light source. Such matrices can be valuable tools in the field of cell treatments and, in general, tissue engineering.

In the present study, the two-photon-assisted direct laser writing (DLW) technique was employed to fabricate microarchitectures with the different elastic modulus (80kPa to 800kPa) from a proteinaceous ink composed of bovine serum albumin (BSA), rose Bengal (RB), or methylene blue (MB), and non-spherical symmetric gold nanoparticles (GNPs), with the ability to generate local temperature increase by stimulation in the near-infrared spectral region. The recorded photothermal efficiency measured using focused continuous wave (CW) laser irradiation at 800nm on microstructures loaded with GNPs at low gold atom concentration (0.01%w/w) reached $12.2 \pm 0.4 °C/W$, that is a record photothermal effect induced from a printed proteinaceous feature.

This photo-thermal functionality arising from the GNPs embedded within the fabricated proteinaceous microstructures can then be applied for studying responses of living systems like cells and bacteria cultures under an externally triggered highly localized heat release.

Abstract Italiano

Le nanoparticelle metalliche, grazie alle loro affascinanti proprietà ottiche ed elettrochimiche, attirano l'attenzione di diverse discipline scientifiche e di ricerca ingegneristica. Tra queste proprietà, l'effetto fototermico indotto dalle risonanze plasmoniche, è una caratteristica notevole ed esclusiva delle nanoparticelle di metalli nobili che, ad oggi, vengono già sfruttate per vari scopi, sia per ricerca che, soprattutto, per applicazioni biomediche. Il fenomeno della risonanza plasmonica superficiale, caratterizzato da bande ben definite, fornisce a queste nanoparticelle una notevole la flessibilità nella risposta ottica che si può vantaggiosamente trasferire a matrici polimeriche in cui queste vengano disperse. In particolare, la possibilità di indurre un aumento di temperatura altamente localizzato che può essere attivato tramite un dispositivo di stimolazione esterno come una sorgente di luce, renderebbe tali matrici strumenti preziosi nel campo dei trattamenti cellulari e, in generale, dell'ingegneria dei tessuti

In questa tesi, la tecnica di scrittura (photo-cross-link) laser diretta (DLW), attivata da assorbimento a due fotoni, è stata impiegata per fabbricare micro-architetture con il diverso modulo elastico (da 80kPa a 800kPa) a partire da un inchiostro proteico composto da albumina di siero bovino (BSA), un foto-iniziatore (Rose Bengale o blu di metilene) e nanoparticelle d'oro a simmetria non sferica (GNP). Mostriamo qui che la presenza di queste ultime, se opportunamente schermate dall'interazione con il foto-iniziatore, fornisce alle microstrutture foto-polimerizzate la capacità di generare un aumento della temperatura locale mediante stimolazione nella regione spettrale del vicino infrarosso. L'efficienza fototermica misurata sotto l'effetto di radiazione laser focalizzata a 800 nm (in continua) su microstrutture caricate con una bassa concentrazione di atomi d'oro (0.01% w/w) ha raggiunto 12.2 ± 0,4 $°C/W$, che costituisce un record di effetto fototermico indotto su una microstruttura a base proteica proteinica stampata tramite DLW.

La funzionalità foto-termica derivante dalle GNP incorporate nelle microstrutture proteiche fabbricate riveste una notevole potenzialità nello studio delle risposte di sistemi viventi, come cellule e colture di batteri, al rilascio di calore altamente localizzato e controllato sia per quanto riguarda il tempo di irraggiamento che la dose rilasciata.

Foreword

The present thesis is a collection of research efforts during 2017 to 2020 in Biophysics and Biophotonics research group, at Department of Physics, University of Milano-Bicocca. Many professors, colleagues and friends have helped in compiling this doctoral thesis, and I would like to thank them for all their efforts at this moment.

I would like to express my acknowledgment to all those who stayed beside me and accompanied me to fulfill this task. Tremendous gratitude to my supervisor, Prof. Giuseppe Chirico, who has consistently supported me, not only as an inspiring academic mentor but also as a person who deeply cares for you. It was fascinating how open and accurate you were during the discussions and the experiments that gave me the belief in a quote: "Give it a try, starting has nothing to do with finishing, like the rivers, some of those reach the sea, and some don't."

I do not have even a word to thank Prof. Maddalena Collini, Prof. Laura D'Alfonso, and Prof. Laura Sironi for their generous help during this project. Deepest thanks to my colleagues Margaux, Mario, and Riccardo for the kind assistance and that always friendly and positive vibe you have carried inside and outside the lab. I am also grateful to Nicolo' and Mykola, my former colleagues, who grabbed my hand at the very early stages of being in Italy.

During this research approach, I met Prof. Niels B. Larsen, who trained me during the internship period, and accepted me for months in his incredible group, PolyCell group at Denmark Technical University (DTU). It was a turning point in my research career, the way you see the multidisciplinary research topics, how you organize the path through personal and group meetings and solve the problems. I appreciate this more than you will ever know.

And last but not least, I am immensely thankful for my beloved parents, who have always shed light on my path, raised me in their arms with love, and to make me an independent person. I am thankful for my one and only younger brother, Amirbahman, because of his tolerance, his courage, and his support to balance everything with the family during my periods of absence.

The emergence of this research product, which had followed by ups and downs, has been instructive and memorable for me. However, life is still on, and I am ready to conquer the next step, with full respect to a Persian poem that says:

"زندگی...

زندگی صحنه یکتای هنرمندی ماست

هرکسی نغمه خود خواند و از صحنه رود

صحنه پیوسته بجاست

خرّم آن نغمه که مردم بسپارند به یاد"

"Life…

Life is a unique scene of art.

You sing your song and depart,

The scene is eternal.

Pleasant that song, which stays in the people's memory to infinity."

"Vita…

È un'unica opera d'arte.

Tu canti la tua canzone e diparti,

la scena è eterna.

Piacevole è quella canzone, che permane eterna nella memoria della gente"

Amirbahador Zeynali

October 21st, MILANO
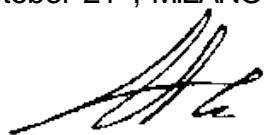
List of abbreviation

AM	Additive Manufacturing
CAD	Computer-aided Design
CAM	Computer-aided Manufacturing
FDM	Fused Deposition Modeling
SLM	Selective Laser Melting
SLA	Stereolithography
DIW	Direct Inkjet Writing
LIFT	Laser Induced Forward Transfer
MPS	Multiphoton Stereolithography
TPS	Two-Photon Stereolithography
TPA	Two Photon Absorption
TPE	Two Photon Excitation
TPC	Two-Photon Crosslinking
GM	Göppert Mayer
NLA	Non-Linear Absorption
NLR	Non-Linear Refraction
SPA	Single Photon Absorption
SPE	Single Photon Excitation
DOF	Depth of Focus
ev	Electron volt
MO	Molecular Orbital
AO	Atomic Orbital
UV	Ultra Violet
IR	Infra-Red
NIR	Near-Inifra-Red
PI	Photo-Initiator
PS	Photo-Sensitizer
HA	Hydrogen Acceptor
HD	Hydrogen Donor
PAG	Photo-Acid Generator

N.A	Numerical Aperture
PSF	Point Spread Function
DLW	Direct Laser Writing
SA	Serum Albumin
BSA	Bovine Serum Albumin
MB	Methylene Blue
RB	Rose Bengal
GNP	Gold NanoParticle
GNR	Gold NanoRod
GNS	Gold NanoStar
GBNP	Gold-Branched NanoParticle
LSPR	Localized Surface Plasmon Resonance
EM	ElectroMagnetic
fs	FemtoSecond
ps	PicoSecond
DMD	Digital Micro-Mirrors
Ti:S	Titanium Sapphire
CW	Continuous Wavelength
SW	Short-Wave
LW	Long-Wave
PTI	PhotoThermal Imaging
FOV	Field of View
IFOV	Instantaneous Field of View
NETD	Noise Equivalent Temperature Difference
PVP	PolyVinylPyrrolidone
PFA	ParaFormAldehyde
FRET	Fluorescence Resonance Energy Transfer
PDT	PhotoDynamic Therapy

List of symbols

Chapter 2.

$\psi^{(n)}$ nth order wave function of perturbation

ω Frequency of excitation

g Ground state

e Excited state

v Virtual state

q Electrical charge

A_0 Amplitude of electromagnetic wave

$\vec{e}$ Vector of complex polarization

ξ Damping factor

S_{xy} Transition probability between states x and y

$\kappa^{(2)}$ Two photon transition rate

δ Two photon cross-section

F Photon Flux

α_f Structural constant

N_{mol} Number of molecules

N_{ph} Number of photons

μ^* Transition dipole moment

$\chi^{(n)}$ nth order susceptibility

E Electric field

$P^{(n)}$ nth order Induced polarization

ε Dielectric constant

α Linear absorption factor

α_2 Non-linear absorption factor

n Refractive index (real part)

n_2 Refractive index (imaginary part)

k Wave number

S_n nth Singlet state

T_n nth Triplet state

E_n Energy level of state n

σ_{xy} Absorption cross-section between states of x and y

f Fluence

I Laser intensity

$\hbar$ Planck constant

w_0 Beam waist

λ Wavelength

R Beam radius

$\mathbb{P}_0$ Laser power

Chapter 3.

ε Extinction coefficient

C Molar concentration

I Light intensity

l Sample thicknes

(I) Initiator molecule

R^o Radical

k_x Rate factor of the x process

M Monomer

f Initiation efficiency

$\mathbb{R}$ Gas constant

T Temperature

η Viscosity

D Exposure dose

E_p Peak power

d Spot size

J_n nth order Bessel function

f_R Repetition rate

t Illumination time

G_0 Photo-initiator constant factor

V Scanning speed

d_f Focal spot diameter

$\mathbb{D}$ Diffusion coefficient

z Axial resolution of the focal spot

r Radial resolution of the focal spot

a Objective parameter (aperture radius)

f Objective parameter (focal length)

Chapter 4.

ϕ_O Singlet oxygen quantum yield

σ_{abs} Absorption cross-section

σ_{sca} Scattering cross-section

ε_m Dielectric constant

V Nanoparticle's volume

$k^{(i)}$ Depolarization factor

R Aspect ratio

r_s Nanoparticle radius

D Thermal diffusivity

τ Relaxation period

σ Surface tension

ΔT Temperature increase

I_0 Laser intensity

A Absorbance factor

c_p Heat capacity

C Concentration

G Thermal conductance

Q_n Energy

θ Temperature factor

η_T Efficiency of thermal energy

ϵ Emissivity factor

ξ Stephan-Boltzman constant

a Area cross-section

h Heat transfer coefficient

M Emmitance factor	$\mathbb{R}$ Bolometric resistance	

Chapter 5.

τ Time-scale	C Compound concentration	d_{focus} Beam focus domain size
χ_{resin} Resin thermal diffusivity	ε Gray body emissivity	T Temperature
R Stephan-Boltzman constant	f Frequency	$F(\delta)$ Force
δ Indentation	E' Reduced Young's Modulus	μ Poisson ratio

x

Table of Contents

Chapter 4. Materials and Methods

Chapter 5. Results and Discussion

Appendix-I

Appendix-II

Chapter 1.

Introduction

1.1. Two-photon additive manufacturing

Optical manufacturing techniques are typically split into two distinct procedures: subtractive and additive. The subtractive methods are based on procedures in which bulk materials are removed, while the *Additive Manufacturing* (AM) is the term that defines layer-by-layer fabrication of a feature, often employing a *Computer-Aided Design* (CAD). Within the well-established AM-based techniques, optical 3D-printing allows to create features with resolutions down to tens of nanometer using different materials (e. g., polymers, ceramics, metals, and biological-based compounds). Stepping out from traditional manufacturing and printing technologies, nowadays advanced optical *Additive Manufacturing* makes it possible to fabricate complex features that are highly valuable in various fields, from optics and electronics to experimental medicine and tissue engineering. The wide variety of optical, or optically assisted, *Additive Manufacturing* techniques spans from *Selective Laser Melting* (SLM), Fused Deposition Modeling (FDM), Direct Laser Writing (DLW), Stereolithography (SLA), Direct Inkjet Writing (DIW), inkjet printing to Laser induced Forward Transfer (LIFT), and microcontact printing, depending on the different source and layer-to-layer transfer method and the 3D-writing capability. These various processes are named time-by-time 3D-printing, rapid prototyping, photo-polymerization or simply additive manufacturing, with a variability that has brought a range of confusion. However, from a general point of view, laser 3D-printing is considered as a rapid prototyping or additive manufacturing method. DLW, SLA, and photo-polymerization are by all means part of the AM techniques, and each of them can be assisted by single-, two- or multiphoton processes. Actually, following the protocols of CAD, computer-aided manufacturing (CAM), and layer-by-layer printing strategies (bottom-up, or top-down), the terms multiphoton stereo-lithography (MPS) or specifically two-photon stereolithography (TPS) can be universally used for these procedures.

In her published Ph.D. thesis, Maria Göppert-Mayer in 1930 characterized, from the theoretical point of view, the possibility of materials to undergo two-photon absorption (TPA). This effort remained for more than a decade an academic deduction, until the lasers came into play and allowed the experimental studies of the TPA phenomenon. Already in 1961, TPA-based processes were observed by Kaiser and Garret [1]. The first experimental two-photon polymerization (TPP[1]) fabrication proof was presented by Maruo et al. in 1997 and was followed by Kawata et al. who fabricated a micro-bull with a feature size around 120nm (sub-diffraction limit). From this point on, year after year, along with the rapid improvement of the laser and thermal sources, a wider set of experimental tests of the TPA and multiphoton absorption (MPA) was performed, leading to technological achievements like high-resolution

---

[1] Polymerization is definition of the general concept. However, the procedure of condensation of some materials like proteins is better defined by the term, crosslinking.

microscopy imaging and 3D optical laser writing. It is the non-linearity of the MPA effect, with the consequent small (diffraction limited) focal or active zone *volume*, and the use of Near Infrared radiation with its ability to penetrate deep into different media (e.g., living-systems), that allowed to reach three-dimensional resolution both in AM techniques or imaging. These advancements have had wide impacts in a very wide range of application fields, like photonic crystals, microfluidics, regenerative medicine, tissue engineering, microoptics, dielectrics, metamaterials, and so forth.

Multiphoton Absorption (MPA) is a process in which two or more photons of lower energy are absorbed simultaneously (i.e., as a single quantum event) by the molecular system, as it is thoroughly discussed in next chapters of the present thesis. This phenomenon leads to relaxations very similar to those occurring after a single photon absorption process, in which a single, higher energy, photon in direct resonance with the energy gap of the molecular system leads to photo-excitation by delivering in a single quantum event all the required excitation energy.
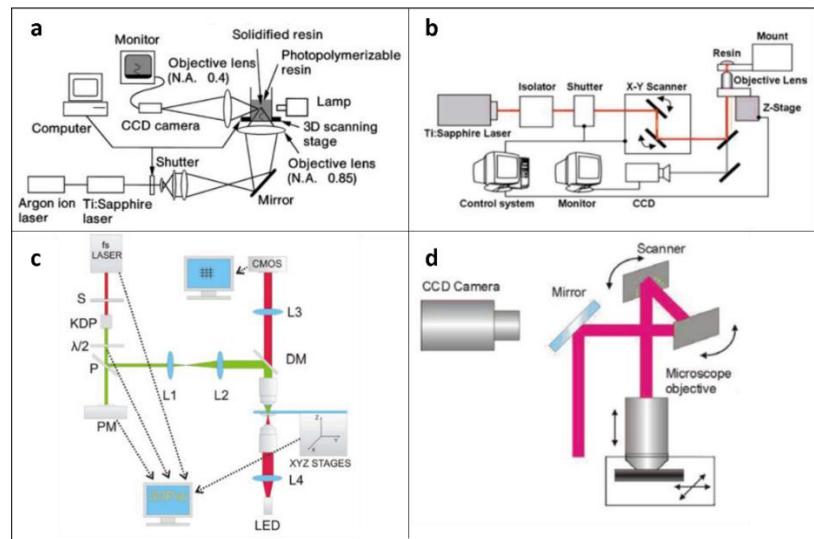

Figure 1.1 Example of different two-photon setups with emphasis on the scanning instrumentation a) Mauro et al. setup with the 3D piezo-stage [3], b) a setup with dual scanning strategy via coupling of galvanometer and 3D piezo-stage [17], c) 3D linear stage used for printing large-scale features [18], d) a dual scanning setup with coupling of galvanometer and 3D linear stage [19].

Multi-photon stereo-lithography allows to build microstructures by photo-curing a resin with an ultrafast focused laser beam scanned on the sample plane. Under the irradiation of a tightly focused and pulsed laser beam, with a pulse duration in the range of hundreds of femtosecond, the target photo-responsive medium (i.e., resin, photoresist, here also called generally "ink") undergoes multi-photon absorption. This phenomenon is limited to the focal volume (a voxel, approximately on the order of tens of nanometer, depending on the numerical

aperture, NA, of the focusing objective) where the resin solidifies or, better, diminishes its solubility due to a variety of possible photochemical processes. Employing different concepts of computer aided manufacturing, by moving either the beam or the sample stage, the desired feature (here is addressed with different terminologies like microstructure, micropattern, and microarchitecture) is fabricated via a spot-by-spot curing process. Importantly, the smoothness of the structure depends mainly on the laser spot size (related to the optical resolution of the setup) and the sample scanning rate. Since multi-photon stereo-lithography is a layer-by-layer fabrication technique, the resolution in the z-direction (the setup optical axis) depends on the step motion along this axis of the scanner.

Regarding the micro-structure features spatial characterization, we emphasize that there is a difference between resolution and feature size. The first is determined by the optical resolution of the setup, namely the laser beam spot size that, for non-linear excitation processes, directly determines the minimum voxel size. The feature size refers to the minimum spacing of two adjacent yet separated structures, which depends, as cited above, on the scanning algorithm and also on photo-physical processes, like local heating, that may take place in the ink during writing. In summary, the main advantage of multi-photon stereo-lithography over stereo-lithography and other techniques is the possibility of achieving nanometer resolution to the expenses of the speed of writing. The steep (quadratic or higher) dependence of the multiphoton excitation probability on the photon density leads to a rapid decay of the molecular excitation rate along the optical axis and to an effective excitation volume smaller (one order of magnitude) than the single-photon excitation one. An additional advantage of multi-photon stereo-lithography is that, by employing multi-photon absorption, one can fabricate tiny features priming polymerization or crosslinking in the photoresist by means of lower energy photons that are minimally invasive for the processed material.

1.2. Applications

The ability of two-photon or multi-photons assisted AM (to which we refer here in general as Multiphoton Stereo-lithography, MPS) to produce very fine, arbitrary shaped, and tiny structures attracts the interest of the scientific and industrial communities from a broad range of disciplines. These 3D-printing methods fostered dramatic improvements in optics and electronics-related technologies by allowing the fabrication of electro-optical components for higher bandwidth transmission and faster data processing [6-8], including waveguides, micro-optical elements, and ultracompact objectives. Besides, the MPS technique has been employed to fabricate moveable micro-machines that find useful applications in the fields of microscopy and microfluidics [12]. Complex features like nano-tweezers, micro-gears, and microfluidic nozzles are among the most promising examples [10-12]. Despite the vast

application of two-photon-assisted AM in solid state Physics and Optics, it is widely recognized that the most promising breakthrough is happening in the biological and biomedical fields. MPS can be used to generate micro-architectural environments for culturing cells and micro-organisms. The use of these devices allow to investigate in an unprecedented way different
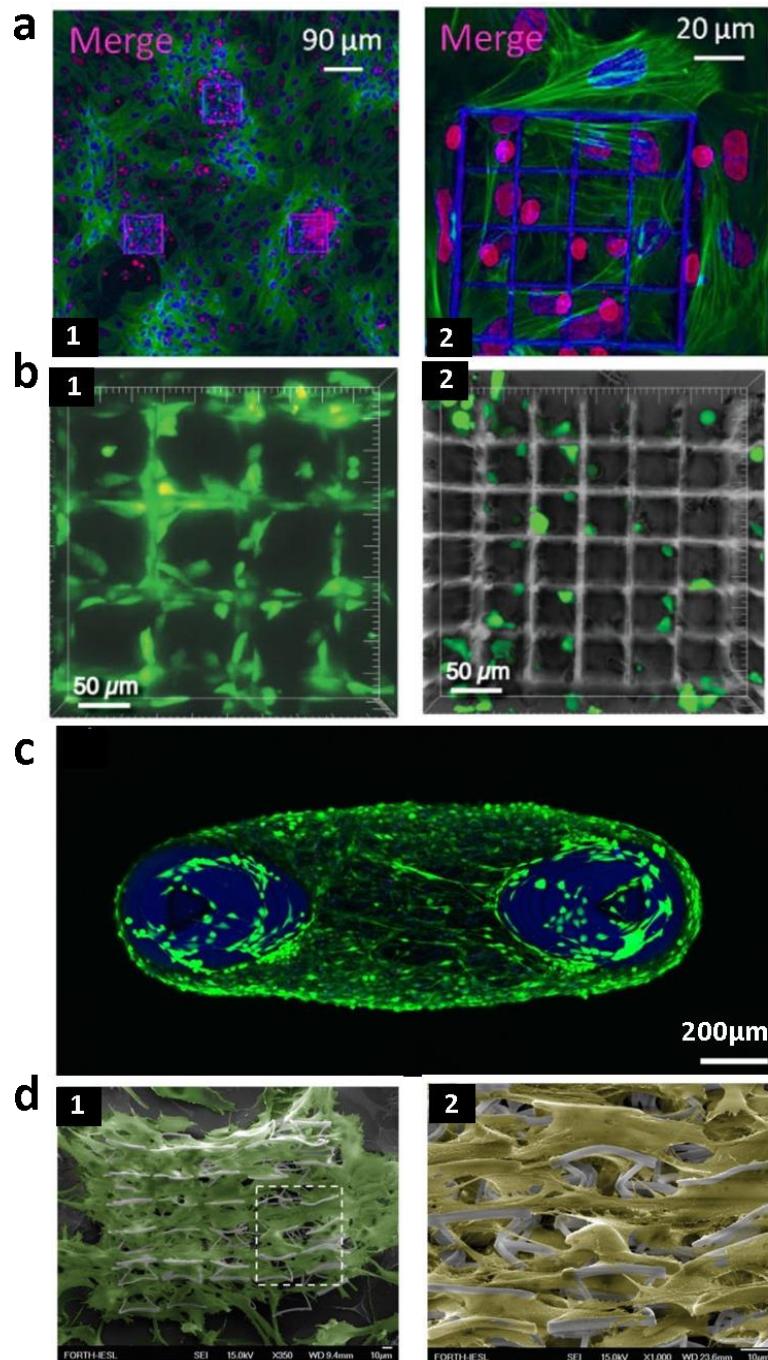
Figure 1.2. (a1-a2) Mesenchymal stem-cell seeded on TPP engineered niches made of SZ2080 resin at 6 culture days, Raimondi et al. 2013 [15]; (b1-b2) HT1080 cell line seeded on viscose triacrylate scaffold, Tayalia et al. 2008 [14]; (c)C2C12 cell microtissue cultured between two PEGDA SLA printed cantilevers (blue channel), Christensen et al. 2019 [13]; (d1-d2) NIH-3T3 cell line cultured on auxetic SZ2080 scaffolds, Flamourakis et al. 2020 [57].

functionalities and behaviors of living systems, like cell adhesion, migration and differentiation, mimicking features of the extracellular matrix (ECM) and allowing to investigate parameters that characterize the cell-cell and cell-ECM interactions. These submicron structures, also known as scaffolds in the field of nano-medicine, are becoming wide spread as 3D spatially controllable culturing environment that overcome some of the most severe limitations of the traditional 2D and bulk cell culturing environments. In addition to this, the ability of MPS to be applied to a wide range of polymers, ceramics, and biological-based materials, together with the possibility of doping, staining, and functionalizing the printed scaffolds, during and after laser writing, make these microstructured environments easily tunable for sophisticated biological studies. Examples of these experiments can be found in the recent literature and span from engineered contractile tissue model [13], cancer migration in engineered scaffolds [14], stem-cell homing [15] to regulation of bacterial growth and development [16] and others [21, 51, 53, 55-57] that are summarized visually in Figure 1.2.

1.3. Photoresist

The primary requirement for photo-polymerization or photo-crosslinking is a precursor solution containing a photo-initiator (PI) and a functional monomer or oligomer along with a light source able to trigger initiation of the cross-linking. Recent developments in the fields of polymer materials and chemistry have introduced a variety of novel materials with features that can be exploited in different research areas and applications. These polymeric materials and the photo-polymerization procedure are now well characterized also for biomedical studies with applications in drug delivery, tissue engineering, regenerative medicine, and medical devices [48-51]. Biomedical applications are flourishing as the available polymer chemistries and processing techniques have matured, enabling the creation of materials that exploit biomolecules as monomers and biologically compatible photo-initiators and that are suitable for use in life science. In this field, AM has been based on the accurate spatio-temporal control photo-polymerization which generally comprises a wide class of reactions that transforms solutions of low molecular weight monomers or pre-polymers into high molecular weight species or crosslinked networks upon exposure to visible, ultraviolet (UV), or infrared (IR) light.

Photo-polymerization allows to reach high reaction rates under ambient conditions with relatively low energy input in non-aqueous and aqueous solutions without too large heat load on the sample. To exploit the high spatial 3D capabilities of AM technologies in life science it is essential to develop new biocompatible photoresists and characterize in this sense commercially available ones, like OrmoComp, SZ2080, PEGDA, and SU-8. Toxicity issues arise in most cases from the photo-initiator molecule rather than the polymer matrix. For many applications, the properties of commercial products do not match well the requirements for

applications in the medical field. In particular, newly developed resins should address a careful control of their mechanical characteristics and the issue of degradability. Focusing on biodegradability, Claeyssen et al. proposed a triblock copolymer containing ε-caprolactone, small PEG chains, and trimethylenecarbonate [20]. Despite the limited resolution of this printed system mainly arising from the shrinking issue upon polymerization, reasonable cell-proliferation and biodegradation time (1 month) was observed when the polymerized structures were put in contact with the cells. Terzaki et al., by using a modified resin comprising methacryloxypropyl trimethoxysilane, zirconium propoxide, and (dimethylamino) ethyl methacrylate, studied the mechanical and cell-adhesion properties. The printed structures showed biocompatibility up to 3 days [21]. Käpylä et al., with the purpose to maximize the potential of biomimetic microstrucutres, designed polyaminoacids based on methacryloylated and acryloylated poly[N(5)-(2-hydroxyethyl) l-glutamine] [22]. These materials are comparable with the PEGDA but with broader processing alternatives.

It has been a while that the emerging field of AM finds its way toward human health technologies, as discussed and referenced earlier in chapter 1. In this sense, employing highly biodegradable, and biocompatible printed architecture plays a relevant role. Natural and synthetically developed biological-based substances show adequate responses to be used as substrates or replicas of living systems and tissues [48-51]. Several labs have focused on 3D-bioprintng technologies, either *ex-vivo* or using intravital techniques, using reagents or resins composed of natural proteins, like bovine serum albumin (BSA), gelatin [58], and avidin [59, 60] or in general those macromolecules with crosslinkable amino acid side chains (here BSA) that can be activated from reactions (Type I or II) that are triggered by the interaction of light and photo-sensitizer (PS) molecules (e.g., RB and MB; for detailed information see chapter 2 and 5) [61]. By tightly focusing of an ultrafast-pulsed laser beam in highly concentrated proteinaceous (normally, ~200-400 mg.mL^{-1}) small volume of PS (up to millimolar) containing resin, dense proteinaceous networks can be generated that are also known as photo-crosslinked matrices or hydrogels.

These biologically-graded matrices created via 3D-priniting technologies (hereafter called TwoPhoton-Crosslinking, TPC) can present properties similar to networks similar of living system substances like the extracellular matrix. The protein-based hydrogels, show many properties of natural ones, like high water content, controllable swelling degree, and tunable stiffness. Moreover, many studies report that printed proteinaceous architectures can save at least some degree of native functionality after being crosslinked. For example, hydrogels printed using avidin maintain significant biotin-binding capacity [59], cross-linked enzymes can retain catalytic activity [62], and cross-linked gelatin (a polypeptide derived from collagen, an extracellular matrix protein) promotes significant cell adhesion. From the perspective of

biomaterials science, the fabricated proteinaceous 3D-matrices are now taken as versatile and reliable benchmark in which different types of living system studies (e.g., cell interactions) can be investigated in a biologically relevant and tunable manner [63]. In this thesis work, a conventional proteinaceous resin containing BSA protein is used for laser TPC of photo-thermally active microarchitectures loaded with gold-nanoparticles. The proteinaceous ink was built up here by tuning the ratio of BSA, Rose Bengal or Methylene Blue as PS molecules and gold-nanoparticles to obtain the desired photo-thermal efficiency.

Existing proteins in ECM like collagen, elastin, and fibronectin have the ultimate properties to mimic the real cellular environment, but the structuration of these materials, following the photo-crosslinking condition, usually results in weak and coarse architectures. By mixing polymers and proteins, in a hybrid polymer-protein ink, one can obtain photo-polymerized/crosslinked structures with the mechanical stability of the polymers and the cell-affinity of proteins. The hybrid approach in photoresist preparation results in general in new functionalities and a broader range of controls like pH and ionic strength actuation, morphology control, and analytes sensing. A recent review analyzes the use of biomaterials in TPP in detail [22]. Bovine serum albumin is listed among the most employed proteins in the field of AM because of its well-studied functionalities, low cost, stimuli-responsive, and similarities to the human serum albumin [23]. Examples of two-photon crosslinking (TPC) of BSA, like photo-crosslinking of BSA using Rose Bengal dye as the photoinitiator, brought to the formation of a biocompatible and pH-responsive 3D microstructures [25]. Of course, it is possible to increase the biological functionality of each protein-based resin by adding another functional protein, as exemplified in studies where mixed resins based on fibronectin and collagen [26, 27] were tested.

The choice of BSA as a monomer for the photo-resist was also led by the fact that BSA is a water-soluble, globular protein that is relatively abundant and low-cost. This protein is a single polypeptide chain, folded into a globular structure. BSA is mainly (68%) in α-helical structure and contains 17 disulfide bonds, with a net negatively charged surface that helps the protein resist aggregation [64, 65]. Despite the high molecular weight of BSA, ~66.5 kDa, the protein's globular shape and negatively charged surface endows it with an extremely high solubility in water (up to ~40% w/v) and low intrinsic viscosity relative to other linear polymers of similar molecular weight. BSA is particularly advantageous as a protein scaffold because it does not dramatically self-assemble or aggregate at increasing concentrations. For example, at room temperature, gelatin methacrylate, a commonly used protein for 3D printing, forms a gel at

concentrations above ~2 wt %, which limits its printability in a vat photopolymerization[2] process.

Depending on the type of initiating mechanism (type I or II, see chapter 5) that is directly determined by the ink composition, the photo-responsive molecule can act like as a photoinitiator motif or as a photosensitizer. Rose Bengal (RB) has been used as a photoinitiator for the TPC of protein biopolymers such as BSA or fibrinogen [52] or for the fabrication of compartments and barriers directly from endogenous cytoplasmic proteins inside live starfish oocytes [67]. The two main photo-initiation mechanisms (see also chapter 5) of initiation are called type I and type II. In type II photo-initiation, electron transfer from the protein to the triplet excited dye is followed by hydrogen transfer and formation of radical sites on the protein that will start the crosslinking process. In type I photo-initiation, the mechanism starts from oxygen sensitization that results in producing singlet oxygen and other reactive oxygen species that will react with oxidizable amino acids, like the epsilon-N of amines in lysine, in the protein backbone, thereby initiating the crosslinking reaction. In the first reaction mechanism, the dye is consumed, while it would act as a sensitizer in the second reaction scheme. Which mechanism is dominant will depend on the structure of the protein and its ability to act as a co-initiator. While no detailed investigations on these mechanisms are available, in the present thesis the fellow and his group orient their efforts to clearly depict the probable crosslinking mechanism. The dependence of the curing efficiency on the Rose Bengal concentration in the crosslinking of bovine serum albumin or fibrinogen was interpreted as evidence for a reaction sequence involving hydrogen abstraction [52]. The observed quenching of the crosslinking process due to ascorbic acid observed in the case of cytoplasmic protein cells [67], on the other hand, pointed to singlet oxygen as a crucial intermediate for the crosslinking process.

Efforts to create a biocompatible micro-environment had not been limited to the use of proteins. Hyaluronic acid (HA), the major component of connective tissues, is another biological-based compound that has dragged attention to be used as a macromer for TPC due to its biocompatibility and easy functionalizing procedures with other materials like methacrylate, glicylmethacrylate, and Tyrosine [28-30]. These materials are typically softer and more biocompatible than PEGDA-based compounds, are biodegradable and can swell by adsorbing water as much as 1000%. Gelatin is a biopolymer, extracted from collagen, that shows a promising hydration process (hydrogel formation), is biocompatible and biodegradable by the human body, and is a valuable alternative candidate to be employed for

---

[2] VAT photopolymerization is a technique which a vat of liquid photoresist is used for layer-by-layer photopolymerization.

AM applications [30, 31]. Its peptide chain can be easily modified to insert (metha)acrylate functionalities that can undergo TPC in the presence of a photoinitiator. There are trials developed by different groups that have printed 3D structures using only modified Gelatin, as a blend with a cross-linker (to achieve a better resolution) [36, 37], or even as a composite matrix [32]. The scaffolds produced with such methodologies retained their biocompatibility and promoted cell attachment and differentiation. Similarly to these systems, many other proteins and bio-macromolecules were implemented in TPC, such as chitosan [33], avidin, biotin [34], dextrane, fibrinogen [35], and others. A practical overview of materials used for TPP is presented in Table 1.1.

Table 1.1. A general example of materials used for TPP, reprinted with permission from reference [56].

Type	Hydrogel	Compound	Photoinitiator	Reference
Nondegradable	No	ORMOCER/Ormocomp	Irgacure 369	[37-39]
	No	SR368+SR499	Lucirin TPO-L	[13, 40]
	Yes	PEGda	Irgacure 369	[41-43]
	Yes	PEGda	WSPI	[44]
	No	AccuraSl10	N/A	[45]
	No	Ti- and Zr-based	Irgacure 369	[46, 47]
	No	Chitosan-based	Lucirin TPO-L	[48]
	No	UDMA	Irgacure 369	[49]
Biodegradable	No	PCL-based	Michlers ketone	[54]
	Yes	gelMOD	Irgacure 2959	[29, 30]
	NO	OLMA	Irgacure 369	[49]
	No	PLA-based	Michlers ketone	[50]
	Yes	BSA and Fibrinogen	Rose Bengal	[51]
	Yes	Biotinylated BSA	Flavin Mononucleotide	[52]
	Yes	Collagen	Benzophenone dimer	[53]

1.4. Project description

The research experience and background of the Biophysics and Biophotonics research group at the Department of Physics "Giuseppe Occhialini" of University of Milano-Bicocca is mainly on the nanoscopy and non-linear microscopy of living-systems, coupled to nanotechnology.

In this latter field, the group is active in the development and use of plasmonic nanoparticles as tools for bio-imaging of cells, bacteria, also in tissues, and in the application of external chemical and physical stimuli as it is the case of localized thermal loads obtained by means of photo-thermal noble metal anisotropic nanoparticles.

The need to apply such stimuli at the single cell level on a spatially resolved platform urged the group to develop a research plan to fabricate miniaturized photothermally active patches to the micron-scale (i.e., microstructures, or microarchitectures) suitable for *in-vitro* culturing cells/bacteria and to perturb the cell growth and differentiation by means of tiny local temperature increases, arising from embedded photo-thermal nanoparticles. The present PhD project grows along this path, with the specific aim to fabricate microstructures loaded with gold nanoparticles (i.e., photothermally active micro-architectures) to study cell/bacteria growth and differentiation under the photo-induced local temperature increase due to the excitation, with visible or near infrared light, of the local surface plasmon resonance (LSPR) of the embed nanoparticles.

The project was supervised by Prof. Giuseppe Chirico and the author as the lead investigator. In order to exploit the highest biocompatibility, but with an eye on defining a novel, low-cost research approach, Bovine Serum Albumin (BSA) and different organic dyes (e.g., Methylene Blue and Rose Bengal) were tested as basic components of inks for TPC procedure. Despite some existing reports on nanoparticles embedded within micro-architecture by means of AM-based techniques, there had not been serious efforts to fabricate nanoparticle doped microstructures using two-photon stereo-lithography starting from nanoparticles doped liquid photoresists. This is the main goal of the present project.

Concerning the nowadays R&D actions towards a reduction of the immune reaction to organ implantation and towards engineering of tissues or implantable device with therapeutic capabilities, the 3D fabrication of micron-scale biocompatible substrates that can be externally triggered by light irradiation can play a role for future low-invasive human therapies. Plasmonic nanoparticles and their vast biomedical applications, mainly based on the localized surface plasmon resonance (LSPR) effect, can be physico-chemically modified to be activated externally with light sources working in the visible to infrared region of the spectrum. On specifically tailored nanoparticles, this activation is followed by a local temperature increase that can be employed for medical therapy and as a cellular stimulus, even in vivo [66]. Current research in the laboratory, along a parallel PhD program, has indeed shown that the differentiation and activation (raise in the base level of neurophysiological activity) can be triggered by repeated exposure to tiny, well controlled, increase of temperature. In the case of the current project, loading spatially well-defined micro-architectures with photo-thermal

nanoparticles will help to study how living systems (e.g., cells and bacteria) grow and differentiate under that above mentioned local temperature increase and to assess what could be the interaction of stimulated and native cells for the grow of organized tissues.

Obviously, for such a project, the characterization of the localized photothermal effect induced by the plasmonic nanoparticles, at a resolution relevant for the size of the fabricated micro-structures (i.e. tens of micrometers) was of paramount importance. To this purpose, a high resolution thermal imaging technique based on a commercial thermo-camera was developed to record the photothermal activity of the fabricated proteinaceous microstructures. Due to the one order of magnitude increase of wavelength in the thermal wave range compared to the visible range, to the large pixel size (on the sample) of the commercial thermo-cameras and to the intrinsic broadening of the signal due to the in-plane heat diffusion, the typical resolution of a commercial thermo-camera is only about 1 mm, definitely too large to map temperature increase of sub-micron size systems. This severely limited the possibility of thermographic mapping of the microstructures that we planned to fabricate. Inspired by several methods that have been developed in recent years that led to tremendous achievements in the spatial resolution of optical microscopies, like Stimulated emission depletion microscopy (STED) and Photo-activated localization microscopy (PALM), the group overcame the above mentioned limitations and reached the desired sub-wavelength resolution by implementing a raster scanning photo-activated thermal imaging of the samples.

These efforts led the group of Biophysics and Biophotonics of the University of Milano-Bicocca (author's institution) to develop a high resolution photo-activated thermal imaging setup that overcome the diffraction limitations imposed by the large value of the wavelength of the thermal radiation and that could be further employed to study several *in-vitro* photothermal effects of different samples include the proteinaceous microstructures. The outputs of these achievements in sub-diffraction resolution thermal imaging and fabrication of photothermally active proteinaceous microstructures are published (as referenced above) in two of top-tier peer reviewed journals: *Nature Communication (2019)[3], and Advanced Optical Materials (2020)[4]*, respectively.

---

[3] Bouzin, M., Marini, M., Zeynali, A., Borzenkov, M., Sironi, L., D'Alfonso, L., Mingozzi, F., Granucci, F., Pallavicini, P., Chirico, G., & Collini, M. (2019). Photo-activated raster scanning thermal imaging at sub-diffraction resolution. *Nature Communications, 10*(1).

[4] Zeynali, A., Marini, M., Chirico, G., Bouzin, M., Borzenkov, M., Sironi, L., D'Alfonso, L., Pallavicini, P., Cassina, V., Mantegazza, F., Granucci, F., Marongiu, L., Polli, D., De la Cadena, A., & Collini, M. (2020). Multiphoton fabrication of proteinaceous Nanocomposite microstructures with Photothermal activity in the infrared. *Advanced Optical Materials, 8*(13), 2000584.

All these briefly reviewed information are discussed in details in five chapters as detailed in below.

In *Chapter 2. Fundamental of multi-photon absorption*, as the title of the chapter indicates, I tried to collect the essential information of the light-matter interaction which leads to the system photo-excitation with an emphasis on the multi-photon (especially two-photon) absorption concept from both quantum and classical points of view. The reader could find some condensed details on the photophysics and selection rule phenomenon besides a quick introduction to the laser physics and Gaussian beam profile.

Chapter 3. The principle of two-photon polymerization/crosslinking starts by introducing the building blocks of the photo-polymerization/crosslinking procedure and includes more in-depth details of crucial processes like photo-initiation, radical-mediated polymerization, and polymerization limiting factors. The chapter provides the reader with more information about the laser optics and microfabrication related to the two-photon polymerization/crosslinking. Reaching to the final point of the chapter, there are notes on laser processing, heat accumulation, and a simple introduction of the project microfabrication two-photon setup that helps the reader to gain fundamental understandings to read the following chapters.

After these chapters, written to provide the fundamental and principle insights of the present project, *Chapter 4, "Materials and methods",* describes the materials used and methods developed in the project. This discussion is guided by sections that contain information about plasmonic effects of nanoparticles and that is followed by an introduction to one of important characterization methods that has been used throughout this study, high resolution thermal imaging.

In the last chapter of this thesis, *Chapter 5, "Results and Discussion"*, all the experimental findings and results, data analysis, and characterization methods are gathered and discussed, starting from protocols of proteinaceous ink preparations to DLW experiments. This chapter collects and analyzes critically the technical knowledge that has acquired during the whole project to employ TPC assisted DLW method to prepare gold nanoparticles (GNPs)-doped proteinaceous microstructures and to study living-systems behaviors (e.g., adhesion, and differentiation) under photothermal effect arising from the embedded GNPs.

1.5. References

[1] W. Kaiser and C. G. B. Garrett. Two-Photon Excitation in CaF2: Eu2+. Phys. Rev. Lett. (1961) 7, 229.

[2] Wollhofen, R., Katzmann, J., Hrelescu, C., Jacak, J., & Klar, T. A. (2013). 120 nm resolution and 55 nm structure size in STED-lithography. *Optics Express*, *21*(9), 10831.

[3] Maruo, S., Nakamura, O., & Kawata, S. (1997). Three-dimensional microfabrication with two-photon-absorbed photopolymerization. *Optics Letters*, *22*(2), 132.

[4] Kawata, S., Sun, H., Tanaka, T., & Takada, K. (2001). Finer features for functional microdevices. *Nature*, *412*(6848), 697-698.

[5] Zhou, X., Hou, Y., & Lin, J. (2015). A review on the processing accuracy of two-photon polymerization. *AIP Advances*, *5*(3), 030701.

[6] Zolfaghari, A., Chen, T., & Yi, A. Y. (2019). Additive manufacturing of precision optics at micro and nanoscale. *International Journal of Extreme Manufacturing*, *1*(1), 012005.

[7] Xinyuan, D., Wang, X., Lin, X., Ding, D., Pan, D., & Chen, R. (2010). Highly flexible polymeric optical waveguide for out-of-plane optical interconnects. *Optics Express*, *18*(15), 16227.

[8] Bogliacino, F., Piva, M., & Vivarelli, M. (2012). R&D and employment: An application of the LSDVC estimator using European microdata. *Economics Letters*, *116*(1), 56-59.

[9] Gissibl, T., Thiele, S., Herkommer, A., & Giessen, H. (2016). Two-photon direct laser writing of ultracompact multi-lens objectives. *Nature Photonics*, *10*(8), 554-560.

[10] Maruo, S., Ikuta, K., and Korogi, H. (2003) Force-controllable, optically driven micromachines fabricated by single-step two-photon micro stereolithography. *J. Microelectromech. Syst.*, 12, 533–539.

[11] Maruo, S., Ikuta, K., and Korogi, H. (2003) Submicron manipulation tools driven by light in a liquid. *Appl. Phys. Lett.*, 82, 133–135.

[12] Knoška, J., Adriano, L., Awel, S., Beyerlein, K. R., Yefanov, O., Oberthuer, D., Peña Murillo, G. E., Roth, N., Sarrou, I., Villanueva-Perez, P., Wiedorn, M. O., Wilde, F., Bajt, S., Chapman, H. N., & Heymann, M. (2020). Ultracompact 3D microfluidics for time-resolved structural biology. *Nature Communications*, *11*(1).

[13] Christensen, R. K., Von Halling Laier, C., Kiziltay, A., Wilson, S., & Larsen, N. B. (2019). 3D printed Hydrogel Multiassay platforms for robust generation of engineered contractile tissues. *Biomacromolecules*, *21*(2), 356-365.

[14] Tayalia, P., Mendonca, C. R., Baldacchini, T., Mooney, D. J., & Mazur, E. (2008). 3D cell-migration studies using two-photon engineered polymer scaffolds. *Advanced Materials*, *20*(23), 4494-4498.

[15] Raimondi, M. T., Eaton, S. M., Laganà, M., Aprile, V., Nava, M. M., Cerullo, G., & Osellame, R. (2013). Three-dimensional structural niches engineered via two-photon laser polymerization promote stem cell homing. *Acta Biomaterialia*, *9*(1), 4579-4584.

[16] Otuka, A., Corrêa, D., Fontana, C., & Mendonça, C. (2014). Direct laser writing by two-photon polymerization as a tool for developing microenvironments for evaluation of bacterial growth. *Materials Science and Engineering: C*, *35*, 185-189.

[17] T. W. Lim et al. Microelectronic Engineering 77 (3-4), 382 (2005).

[18] M.-A. Maher et al. 7204, 72040C (2009).

[19] S. Passinger et al., in Nanotechnology III, Vol. 6591, pp. 59104.

[20] You, S., Li, J., Zhu, W., Yu, C., Mei, D., & Chen, S. (2018). Nanoscale 3D printing of hydrogels for cellular tissue engineering. *Journal of Materials Chemistry B*, *6*(15), 2187-2197.

[21] Terzaki, K., Kissamitaki, M., Skarmoutsou, A., Fotakis, C., Charitidis, C. A., Farsari, M., Vamvakaki, M., & Chatzinikolaidou, M. (2013). Pre-osteoblastic cell response on three-dimensional, organic-inorganic hybrid material scaffolds for bone tissue engineering. *Journal of Biomedical Materials Research Part A*, *101A*(8), 2283-2294.

[22] Käpylä, E., Sedlačík, T., Aydogan, D. B., Viitanen, J., Rypáček, F., & Kellomäki, M. (2014). Direct laser writing of synthetic poly(amino acid) hydrogels and poly(ethylene glycol) diacrylates by two-photon polymerization. *Materials Science and Engineering: C*, *43*, 280-289.

[23] Torgersen, J., Qin, X., Li, Z., Ovsianikov, A., Liska, R., & Stampfl, J. (2013). Hydrogels for two-photon polymerization: A toolbox for mimicking the Extracellular matrix. *Advanced Functional Materials*, *23*(36), 4542-4554.

[24] Wei, S., Liu, J., Zhao, Y., Zhang, T., Zheng, M., Jin, F., Dong, X., Xing, J., & Duan, X. (2017). Protein-based 3D microstructures with controllable morphology and pH-responsive properties. *ACS Applied Materials & Interfaces*, *9*(48), 42247-42257.

[25] Serien, D., & Takeuchi, S. (2017). Multi-component Microscaffold with 3D spatially defined proteinaceous environment. *ACS Biomaterials Science & Engineering*, *3*(3), 487-494.

[26] Da Sie, Y., Li, Y., Chang, N., Campagnola, P. J., & Chen, S. (2015). Fabrication of three-dimensional multi-protein microstructures for cell migration and adhesion enhancement. *Biomedical Optics Express*, *6*(2), 480.

[27] Berg, A., Wyrwa, R., Weisser, J., Weiss, T., Schade, R., Hildebrand, G., Liefeith, K., Schneider, B., Ellinger, R., & Schnabelrauch, M. (2011). Synthesis of Photopolymerizable hydrophilic Macromers and evaluation of their applicability as reactive resin components for the fabrication of three-dimensionally structured Hydrogel matrices by 2-Photon-Polymerization. *Advanced Engineering Materials*, *13*(9), B274-B284.

[28] Loebel, C., Broguiere, N., Alini, M., Zenobi-Wong, M., & Eglin, D. (2015). Microfabrication of photo-cross-Linked Hyaluronan Hydrogels by single- and two-photon tyramine oxidation. *Biomacromolecules*, *16*(9), 2624-2630.

[29] Kufelt, O., El-Tamer, A., Sehring, C., Schlie-Wolter, S., & Chichkov, B. N. (2014). Hyaluronic acid based materials for scaffolding via two-photon polymerization. *Biomacromolecules*, *15*(2), 650-659.

[30] Ovsianikov, A., Deiwick, A., Van Vlierberghe, S., Pflaum, M., Wilhelmi, M., Dubruel, P., & Chichkov, B. (2011). Laser fabrication of 3D gelatin scaffolds for the generation of Bioartificial tissues. *Materials*, *4*(1), 288-299.

[31] Ovsianikov, A., Deiwick, A., Van Vlierberghe, S., Dubruel, P., Möller, L., Dräger, G., & Chichkov, B. (2011). Laser fabrication of three-dimensional CAD scaffolds from photosensitive gelatin for applications in tissue engineering. *Biomacromolecules*, *12*(4), 851-858.

[32] Field, R. D., Anandakumaran, P. N., & Sia, S. K. (2019). Soft medical microrobots: Design components and system integration. *Applied Physics Reviews*, *6*(4), 041305.

[33] Kufelt, O., El-Tamer, A., Sehring, C., Meißner, M., Schlie-Wolter, S., & Chichkov, B. N. (2015). Water-soluble photopolymerizable chitosan hydrogels for biofabrication via two-photon polymerization. *Acta Biomaterialia*, *18*, 186-195.

[34] Kaehr, B., & Shear, J. B. (2008). Multiphoton fabrication of chemically responsive protein hydrogels for microactuation. *Proceedings of the National Academy of Sciences*, *105*(26), 8850-8854.

[35] Basu, S., & Campagnola, P. J. (2004). Properties of crosslinked protein matrices for tissue engineering applications synthesized by multiphoton excitation. *Journal of Biomedical Materials Research*, *71A*(2), 359-368.

[36] Brigo, L., Urciuolo, A., Giulitti, S., Della Giustina, G., Tromayer, M., Liska, R., Elvassore, N., & Brusatin, G. (2017). 3D high-resolution two-photon crosslinked hydrogel structures for biological studies. *Acta Biomaterialia*, *55*, 373-384.

[37] Engelhardt, S., Hoch, E., Borchers, K., Meyer, W., Krüger, H., Tovar, G. E., & Gillner, A. (2011). Fabrication of 2D protein microstructures and 3D polymer–protein hybrid microstructures by two-photon polymerization. *Biofabrication*, *3*(2), 025003.

[38] Klein, F., Striebel, T., Fischer, J., Jiang, Z., Franz, C. M., Von Freymann, G., Wegener, M., & Bastmeyer, M. (2010). Elastic fully three-dimensional microstructure scaffolds for cell force measurements. *Advanced Materials*, *22*(8), 868-871.

[39] Ovsianikov, A., Schlie, S., Ngezahayo, A., Haverich, A., & Chichkov, B. N. (2007). Two-photon polymerization technique for microfabrication of CAD-designed 3D scaffolds from commercially available photosensitive materials. *Journal of Tissue Engineering and Regenerative Medicine*, *1*(6), 443-449.

[40] Kiyan, Y., Limbourg, A., Kiyan, R., Tkachuk, S., Limbourg, F. P., Ovsianikov, A., Chichkov, B. N., Haller, H., & Dumler, I. (2012). Urokinase receptor associates with Myocardin to control vascular smooth muscle cells phenotype in vascular disease. *Arteriosclerosis, Thrombosis, and Vascular Biology*, *32*(1), 110-122.

[41] Tayalia, P., Mazur, E., & Mooney, D. J. (2011). Controlled architectural and chemotactic studies of 3D cell migration. *Biomaterials*, *32*(10), 2634-2641.

[42] Ovsianikov, A., Malinauskas, M., Schlie, S., Chichkov, B., Gittard, S., Narayan, R., Löbler, M., Sternberg, K., Schmitz, K., & Haverich, A. (2011). Three-dimensional laser micro- and nano-structuring of acrylated poly(ethylene glycol) materials and evaluation of their cytoxicity for tissue engineering applications. *Acta Biomaterialia*, *7*(3), 967-974.

[43] Klein, F., Richter, B., Striebel, T., Franz, C. M., Freymann, G. V., Wegener, M., & Bastmeyer, M. (2011). Two-component polymer scaffolds for controlled three-dimensional cell culture. *Advanced Materials*, *23*(11), 1341-1345.

[44] Ovsianikov, A., Gruene, M., Pflaum, M., Koch, L., Maiorana, F., Wilhelmi, M., Haverich, A., & Chichkov, B. (2010). Laser printing of cells into 3D scaffolds. *Biofabrication*, *2*(1), 014104.

[45] Torgersen, J., Ovsianikov, A., Mironov, V., Pucher, N., Qin, X., Li, Z., Cicha, K., Machacek, T., Liska, R., Jantsch, V., & Stampfl, J. (2012). Photo-sensitive hydrogels for three-dimensional laser microfabrication in the presence of whole organisms. *Journal of Biomedical Optics*, *17*(10), 1.

[46] Hsieh, T. M., Benjamin Ng, C. W., Narayanan, K., Wan, A. C., & Ying, J. Y. (2010). Three-dimensional microstructured tissue scaffolds fabricated by two-photon laser scanning photolithography. *Biomaterials*, *31*(30), 7648-7652.

[47] Psycharakis, S., Tosca, A., Melissinaki, V., Giakoumaki, A., & Ranella, A. (2011). Tailor-made three-dimensional hybrid scaffolds for cell cultures. *Biomedical Materials*, *6*(4), 045008.

[48] Danilevicius, P. (2012). Micro-structured polymer scaffolds fabricated by direct laser writing for tissue engineering. *Journal of Biomedical Optics*, *17*(8), 081405.

[49] Correa, D. S., Tayalia, P., Cosendey, G., Dos Santos, D. S., Aroca, R. F., Mazur, E., & Mendonca, C. R. (2009). Two-photon polymerization for fabricating structures containing the Biopolymer Chitosan. *Journal of Nanoscience and Nanotechnology*, *9*(10), 5845-5849.

[50] Weiß, T., Schade, R., Laube, T., Berg, A., Hildebrand, G., Wyrwa, R., Schnabelrauch, M., & Liefeith, K. (2011). Two-photon polymerization of Biocompatible photopolymers for Microstructured 3D Biointerfaces. *Advanced Engineering Materials*, *13*(9), B264-B273.

[51] Melissinaki, V., Gill, A. A., Ortega, I., Vamvakaki, M., Ranella, A., Haycock, J. W., Fotakis, C., Farsari, M., & Claeyssens, F. (2011). Direct laser writing of 3D scaffolds for neural tissue engineering applications. *Biofabrication*, *3*(4), 045005.

[52] Pitts, J. D., Campagnola, P. J., Epling, G. A., & Goodman, S. L. (2000). Submicron Multiphoton free-form fabrication of proteins and polymers: Studies of reaction efficiencies and applications in sustained release. *Macromolecules*, *33*(5), 1514-1523.

[53] Turunen, S., Käpylä, E., Terzaki, K., Viitanen, J., Fotakis, C., Kellomäki, M., & Farsari, M. (2011). Pico- and femtosecond laser-induced crosslinking of protein microstructures: Evaluation of processability and bioactivity. *Biofabrication*, *3*(4), 045002.

[54] Basu, S., Cunningham, L. P., Pins, G. D., Bush, K. A., Taboada, R., Howell, A. R., Wang, J., & Campagnola, P. J. (2005). Multiphoton excited fabrication of collagen matrixes cross-linked by a modified Benzophenone dimer: Bioactivity and enzymatic degradation. *Biomacromolecules*, *6*(3), 1465-1474.

[55] Claeyssens, F., Hasan, E., Gaidukeviciute, A., Achilleos, D., Ranella, A., Reinhardt, C., Ovsianikov, A., Shizhou, X., Fotakis, C., Vamvakaki, M., Chichkov, B., & Farsari, M. (2009). Three-Dimensional Biodegradable Structures Fabricated by Two-Photon Polymerization. *Langmuir*, *25*(5), 3219–3223.

[56] Ovsianikov, A., Mironov, V., Stampfl, J., & Liska, R. (2012). Engineering 3D cell-culture matrices: Multiphoton processing technologies for biological and tissue engineering applications. *Expert Review of Medical Devices*, *9*(6), 613-633.

[57] Flamourakis, G., Spanos, I., Vangelatos, Z., Manganas, P., Papadimitriou, L., Grigoropoulos, C., Ranella, A., & Farsari, M. (2020). Laser-made 3D auxetic Metamaterial scaffolds for tissue engineering applications. *Macromolecular Materials and Engineering*, *305*(7), 2000238.

[58] J.L. Connell, E.T. Ritschdorff, M. Whiteley, J.B. Shear, 3D printing of microscopic bacterial communities, Proc. Natl. Acad. Sci. USA. (2013) 110.

[59] B. Kaehr, R. Allen, D.J. Javier, J. Currie, J.B. Shear, Guiding neuronal development with *in situ* microfabrication, Proc. Natl. Acad. Sci. USA. (2004) 101.

[60] E.C. Spivey, E.T. Ritschdorff, J.L. Connell, C.A. Mclennon, C.E. Schmidt, J.B. Shear, Multiphoton lithography of unconstrained three-dimensional protein microstructures, Adv. Funct. Mater. (2013) 23.

[61] S.F. Christopher, Type I and type II mechanisms of photodynamic action, in: Light - Activated Pesticides, American Chemical Society, Washington, DC, 1987, p. 22.

[62] R. Allen, R. Nielson, D.D. Wise, J.B. Shear, Catalytic three-dimensional protein architectures, Anal. Chem. (2005) 77.

[63] J.L. Connell, J. Kim, J.B. Shear, A.J. Bard, M. Whiteley, Real-time monitoring of quorum sensing in 3D-printed bacterial aggregates using scanning electrochemical microscopy, Proc. Natl. Acad. Sci. USA. (2014) 111.

[64] Reed, R. G.; Feldhoff, R. C.; Clute, O.; Peters, T. Fragments of Bovine Serum Albumin Produced by Limited Proteolysis. Conformation and Ligand Binding. Biochemistry 1975, 14, 4578- 4583.

[65] Ueki, T.; Hiragi, Y.; Kataoka, M.; Inoko, Y.; Amemiya, Y.; Izumi, Y.; Tagawa, H.; Muroga, Y. Aggregation of Bovine Serum Albumin Upon Cleavage of Its Disulfide Bonds, Studied by the TimeResolved Small-Angle X-Ray Scattering Technique with Synchrotron Radiation. Biophys. Chem. 1985, 23, 115-124.

[66] Urciuolo, A., Poli, I., Brandolino, L., Raffa, P., Scattolini, V., & Laterza, C. et al. (2020). Intravital three-dimensional bioprinting. *Nature Biomedical Engineering*, *4*(9), 901-915.

[67] S. Basu, V. Rodionov, M. Terasaki and J. Campagnola Paul, Opt. Lett., 2005, 30, 159–161.

Chapter 2.

Fundamentals of multi-photon absorption

2.1. Theory of light-matter interaction

2.1.1. Quantum view

The two-photon absorption (TPA) phenomenon consists of the simultaneous absorption of two photons in a single quantum process. The theoretical description of TPA as a non-linear effect (second-order) is based on the semi-classical treatment of the radiation matter interaction by means of the time dependent perturbation theory. Within this method, the perturbed molecular wave-function under the action of an electromagnetic wave can be written as [1]:

$$\psi_g^{(2)}(r,t) = \psi_g^{(1)}(r,t) + \frac{q^2 A_0^2 \omega^2}{\hbar} \sum S_{ge} \, \psi_e^0(r) \left(\frac{1-\exp[-i(\omega_{eg}-2\omega)t]}{\omega_{eg}-2\omega} \right) + \cdots \quad (2.1)$$

Where $\psi_g^{(1)}(r,t)$ is the ground-state wave-function of quantum system, ω is the excitation angular frequency, ω_{eg} is the transition frequency between ground-state g and excited-state e, and S_{ge} is a factor that depends on the transition dipoles among different vibronic states and determines the transition probability. A_0 is the amplitude of the electromagnetic wave and q is the electric charge. As it will be explained later on this chapter, the two-photon absorption (TPA) promotes of the electronic system of a molecule from ground state to the excited-state by passing through an intermediate vibronic state.

$$S_{ge} = \sum \left(\frac{<g|\vec{e}r|v><v|\vec{e}r|e>}{\omega_{gv}-\omega-\xi} \right) \quad (2.2)$$

The summation in equation (2.2) over the intermediate vibronic state v represents the two-photon transition probability with ω_{gv} as the transition frequency between ground-state and virtual state, ξ as the damping factor (where in usual approximation is constantly given by the value 0.1ev), and $\vec{e}$ stands for the complex polarization vector affecting the two-photon excitation process. In addition to the factors, the terms $< g \left| \vec{e}r \right| v >$ and $< v \left| \vec{e}r \right| e >$ are the transition densities from ground state to the vibronic state and from the vibronic state to the excited-state respectively. The aforementioned equation works properly in the single-color (equal frequencies for absorbed photon) regime. It is worth noting that Eq.2.1 and Eq.2.2 are the result of the application of the time dependent perturbation theory to the second order that implies a coupling of the ground and excited state with an intermediate state that is a real eigenvalue of a vibronic state of the system. An alternative, qualitative, picture of the two-photon or multiphoton approach can be obtained by means of the virtual states that can be

thought as states whose energy is highly undetermined due to the very low residence time (about 1 fs).

The square of this probability behavior is proportional directly to the two-photon cross section δ. The S_{ge} (if $\neq 0$) coupled with some physical constants of the material and light-source parameters determines the two-photon transition rate $\kappa_{ge}^{(2)}$ (s^{-1}).

$$\kappa_{ge}^{(2)} = 8\pi(\frac{qA_0\omega}{\hbar})^4 |S_{ge}(\omega)|^2 g_M(2\omega) = 128\pi^3 \alpha_f^2 \omega^2 F^2 |S_{ge}(\omega)|^2 g_M(2\omega) \qquad (2.3)$$

The square of the amplitude of the electromagnetic wave (here is coming from the laser/light source) is proportional both to the photon flux F and the frequency ω ($A_0^2 \sim F/\omega^2$), indicating that the TPA process scales with the square of the photon flux. The α_f is a dimensionless fine structure constant, and the g_M is the spectral line profile of the material. From this, the TPA cross section can be computed as:

$$\delta = \frac{\kappa_{ge}^{(2)}}{F^2} = 128\pi^3 \alpha_f^2 \omega^2 |S_{ge}(\omega)|^2 g_M(2\omega) \qquad (2.4)$$

This equation shows the dependency of the δ ($cm^4.s.molecule^{-1}.photon^{-1}$) with the molecular parameters of a material. The two-photon cross-section factors are normally given in units of Göppert Mayer [GM] ($1 GM = 10^{-50} cm^4 s$). Hence the total number of TPE events per unit time occurring with N_{mol} molecules hit by the radiation with flux F, in a single pulse duration, will be:

$$\frac{dN_{ph}}{dt} = N_{mol} \kappa_{ge}^{(2)} = N_{mol} \delta F^2 \qquad (2.5)$$

2.1.2. Continuum description

It is possible to describe the TPA process in a continuum based model. In this picture, each molecule has an induced transition dipole moment μ_* that comes from the interaction of an electric field (ω) and the electrons. The probability of the molecular excitation via absorption of a single photon scales linearly with the applied electric field (ω). Similarly, under a weak radiation source, the induced polarization (ω) of a molecule linearly relates to the (ω), since it is proportional to the induced dipole moment [7] as:

$$P(\omega) = \varepsilon_0 \chi^{(1)} E(\omega) = |N_{mol}\mu^*| \qquad (2.6)$$

Where N_{mol} is the volume density of chromophores. Here $\chi^{(1)}$ is the linear susceptibility. This value of $\chi^{(1)}$ also appears in the complex refractive index n_c of the medium (and the dielectric constant ε) that acts as important factor in determination of the material optical responses under light irradiations.

$$n_c^2(\omega) = \varepsilon^2(\omega) = 1 + 4\pi\chi^{(1)} \tag{2.7}$$

Where the complex refractive index ($n_c = n + in_2$) has been built up from real n and imaginary n_2 parts. The real part is responsible for the dispersion and the imaginary part corresponds to the absorption. Eq. 2.6 describes a first order approximation of the medium response to the applied field and it can be expanded to higher orders in the electric field amplitude. For large values of the electric field non-linear light-matter interactions occurs that result in additional polarization terms as it follows:

$$P = \varepsilon_0(\chi^{(1)}E + \chi^{(2)}E \cdot E + \chi^{(3)}E \cdot E \cdot E + \dots) \tag{2.8}$$

$$P = P^{(1)} + P^{(2)} + P^{(3)} + \dots \tag{2.9}$$

Where $^{(n)}$ and $^{(n)}$ are nth order susceptibility and polarization, respectively. For mediums with the inversion symmetry (see Figure 2.1) like liquids and amorphous solids, the electric dipole approximation gives $\chi^{(3)}$ as the lowest non-linear term and all the other even terms following the third-order susceptibility will have vanishing amplitudes (isotropic materials).

Regarding the final state of the two-photon transition and the state from which the chemical reaction of cross-linking may occur, there are two different schemes, as in Fig.2.1. For molecules with a symmetric distribution of charges and for which the first term of the electric potential expansion is the quadruple one, the final state of the two-photon transition cannot be the same S_1 state. However, the system may rapidly relax from the higher energy excited state, S_2, to S_1 from which it may decay or, better it can undergo a chemical reaction (Fig.2.1a). For a molecule with an asymmetric charge distribution, for which a dipole moment exist, the final state of the two-photon absorption can be the very same as S_1 state as we can reach with a single photon excitation (Fig.2.1.b).
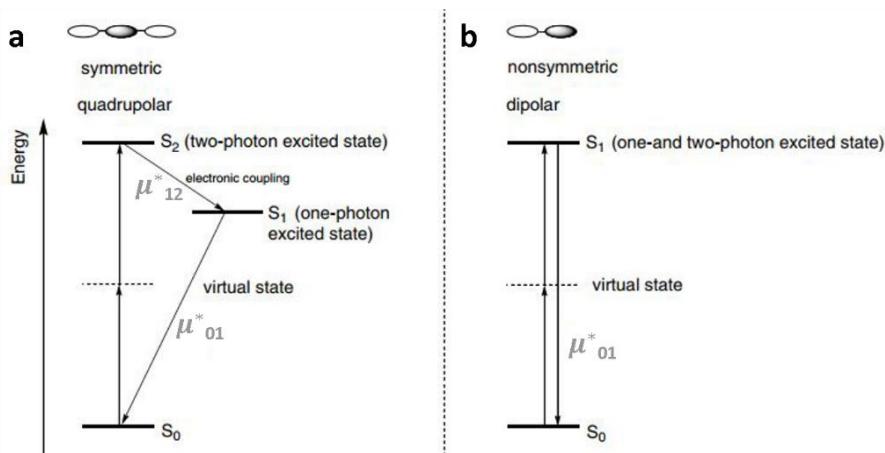

Figure 2.1. Jablonski diagrams of photo=excitation of a) symmetric and b) nonsymmetrical material. μ_{01}^* and μ_{12}^* stand for transition dipole moments between ground state and first singlet excited state and between two excited states, respectively.

Aside from TPA phenomenon, the $\chi^{(3)}$ concerns in description of both Stokes-Raman and anti-Stokes-Raman. Within this formulation, the absorption rate of n photons by a medium/molecule is proportional to $E \cdot P^{(2n-1)}$, which defines the regime for multi-photon absorption in a way includes non-linear polarization or susceptibilies of odd orders. The third order non-linearity results also in non-linear absorption (NLA, α_2) and non-linear refraction (NLR, n_2) that leads to autofocusing. These parameters are respectively proportional to the imaginary and real part of $^{(3)}$, and can be measured by means of a methodology known as Z-scan [11, 12].

Considering a thin sample (comparable with Rayleigh range), these non-linear variables come along together in light irradiance I and phase shift ϕ formulas.

$$\frac{dI(z,t)}{dz} = -\alpha I(z,t) - \alpha_2 I^2(z,t) \qquad (2.10)$$

$$\frac{d\phi(z,t)}{dz} = kn_2 I(z,t) \qquad (2.11)$$

Here α is the linear absorption coefficient, α_2 is the two-photon (first non-linear term) absorption coefficient [8], k is the wavenumber, the imaginary part of refractive index n_2 has defined above, and z is the propagation direction. The above stated equalities are also work in non-linear regimes arisen from ultrafast light propagations (sub-femtosecond) or in another word, pulse width-dependent responses. Equations (2.10) and (2.11) are the basis for the formulation the so-called Z-scan method for characterizing the non-linear responses of materials.

2.2. Light-matter interaction: The role of photons irradiance in TPA

The effect of light on matter can be fully described by the interaction of n photons of energy $\hbar\omega$. In one single quantum event, an electron from the ground state g or S_0 could migrates to the excited levels e or S_n (molecular excitation or excited-state absorption) by means of a linear (single-photon) or of a non-linear (two/multi-photons) absorption. In the below statement the dependency of these processes on the light irradiation is reported. Besides, the analytical dependence of the excitation rate on the irradiance starting from a simplified picture that exploit the concept of virtual state are derive in the following equations.

When employing photons of energy lower than the energy gap, E_g - E_e, which corresponds to the single photon absorption (SPA), the multi-photon absorption is also possible, in the conditions which is stated in the following. In the case of a single color experiment in which a single laser line impinges on the sample, the multiphoton process occurs typically when the photon energy $E_{h\nu}$ is an integer fraction of the energy gap: $E_{h\nu} \cong (E_g - Ee)/n$. The multi-

photon absorption occurs as a subsequent passage through a set of n very short-living ($\cong$ $1fs$) virtual state v with an energy lower than the energy of excited-state E_e and higher than the ground state energy E_g ($E_g < E_v < E_e$). For a vanishing lifetime of the virtual states we obtain the (quantum mechanically equivalent) simultaneous absorption of (n)-photons of energy of $(E_g - Ee)/n$. For a two-photons process there is one single virtual state, and for three-photon absorption there are two virtual states, and so forth. The energy distribution of the virtual states can be degenerate ($E_{vn} - E_g = E_e - E_{vn}$) when two photons of the same energy (and typically the same source) promote the electron to the excited-state from the ground-state, or non-degenerate, if $E_{vn} - E_g \neq E_e - E_{vn}$. In this case, the excitation occurs by absorption of two photons with different energies and sources (Figure 2.2).
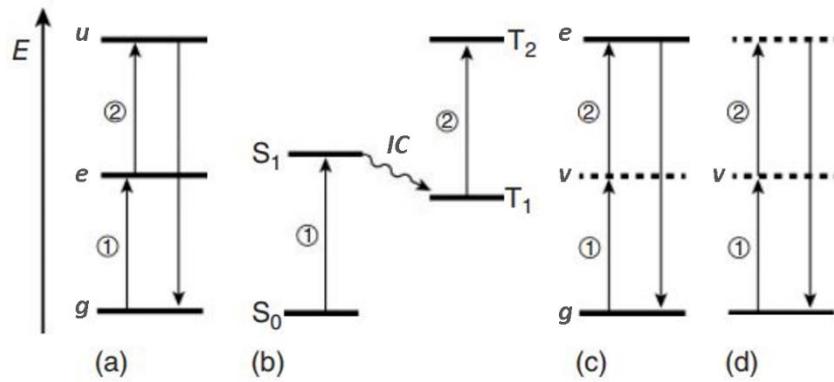
Figure 2.2. Sequential (a & b) and simultaneous (c & b) Jablosnki diagrams of TPA. The virtual state v is depicted with dash lines, and IC term stands for the intersystem crossing phenomenon.

The description of the above described process for the degenerate 2-photons case (The sequential process also follows the same formulation that is the exact mechanism can be observed through photo-excitation of nanoparticles [9]) can be formulated as it is shown below [2]:

$$\frac{dI}{dz} = -\sigma_{gv} N_g I(t) - \sigma_{ve} N_e I(t) \tag{2.12}$$

$$\frac{dN_e}{dt} = \frac{\sigma_{ge}}{\hbar\omega} N_g I(t) \tag{2.13}$$

In above equation, σ_{xy} stands for the absorption cross section between states x and y, N_g and N_e are the population densities of ground and excited-states, respectively. This equations hold if the excited electron does not decay within the pulse-width. The above equations are valid for the case in which the intermediated state lies within the rotational-vibrational (rovibronic) band (therefore not being a virtual state) and also for further triplet-state transitions. Since the two-photon/multi-photon absorptions take place in a regime where ultrafast pulses (laser

sources) are coursing, the approximation could be integrated with the laser fluence (energy per unit area) over time.

$$\frac{df}{dz} = -\sigma_{ge}N_g f - \sigma_{ge}N_g \frac{(\sigma_{ev}-\sigma_{ge})}{2\hbar\omega}f^2 \qquad (2.14)$$

It is worth noting that that by deriving a description of the attenuation of the beam as it propagates through the medium, we find a dependence on the photon fluence and not the irradiance. The fluence f is computed as $f = \int_{-\infty}^{+\infty} I(t)dt$ and it is the optical energy delivered per unit area (J cm^{-2}). Laser intensity (or irradiance) I is the optical power per unit area (W cm^{-2}) and can also be derived as the product of the energy and flux of photons.

In equation 2.14 one can see that the term related to the square of the photon fluence depends on the product of two one-photon cross-sections. Thus, this equation shows the transition from consecutive absorption of two photons when the system jump from the ground state to an intermediate (either virtual or not) state and then the final excited state, to the case of a resonant, two-step, two-photon absorption. This fact can be better appreciated by a treatment reported already in 1974 by Kafri and Kimel [Kafri, O., Kimel, S., Theory of two-photon absorption and emission second order saturation, Chemical Physics 5 (1974) 488-493] in which these Authors derive the rate of excitation as:

$$\frac{dN_e}{dt} = \frac{N_g B_{gv}B_{ve}\tau_v I^2}{1+(B_{gv}+B_{ve})\tau_v I} \qquad (2.15)$$

In the above equation is formulated by using Einstein absorption coefficients, that are inversely proportional to the spontaneous relaxation time of the upper level, and introduced the intermediate (virtual) state lifetime τ_v. In the limit $\tau_v \to 0$, i.e. when the state becomes virtual, we have $B_{ve}\tau_v \to 0$ and $B_{gv}\tau_v \to \sigma_{gv}$ and therefore the second order relation, with saturation, can be written as follows:

$$\frac{dN_e}{dt} = \frac{N_g B_{ve}\sigma_{gv}I^2}{1+\sigma_{gv}I} \qquad (2.16)$$

Similar relations are typically used to fit the fluorescence response of dyes excited by two-photon processes. The example of two consecutive, albeit very close each other, transitions to reach a final excited state is can be found for gold nanopillars [10].

The equation (2.13) could be re-written in term of the number of excited species due to SPA in unit-time and unit-volume with symbol $n^{(1)}$.

$$n^{(1)} = \sigma(\omega)N_g \frac{I}{\hbar\omega} \qquad (2.17)$$

Similarly, the probability of simultaneous absorption of two-photons is proportional to the $n^{(2)}$.

$$n^{(2)} = \frac{1}{2}\,\delta(\omega)N_g\left(\frac{I}{\hbar\omega}\right)^2 \tag{2.18}$$

Where here δ is the TPA cross-section (introduced in eq. 2.4). In most of the organic molecules/dyes the ratio of $n^{(2)}/n^{(1)}$ is small denoting that the TPA is very weak process in comparison with the SPA. Thus, pulsed lasers with high peak power is required to have the two-photon absorption/excitation effectively (although the photon-cross section of the compounds is of importance too).

2.2.1. Photophysics and selection rules

Both singlet and triplet states are involved in the complex photo-dynamics a molecule can undergo. A state is called singlet S_n when it has spin zero. While, states with one pair parallel spin (spin quantum number is 1) are called as triplet states T_n. Multiplicity demonstrates the possible spin quantum numbers. Singlet and triplet states are typically endowed with very different lifetimes, in the range of nanoseconds for singlet and in the range of milliseconds or more for triplets. This is the time available for excited state chemical reactions that are at the basis of the photo-chemistry exploited in laser writing.
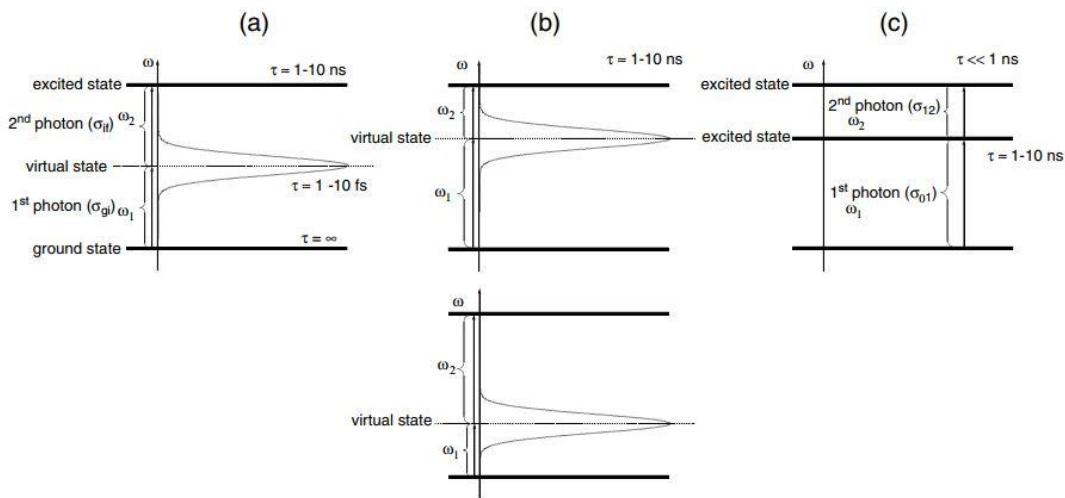
Figure 2.3. Jablonski diagrams of degenerate (a, $\omega_1 = \omega_2$) and non-degenerate (b and c, $\omega_1 \neq \omega_2$) two-photon excitation. Panel (a) and (b) depict simultaneous TPA in which (largely undetermined) virtual state occur while panel (c) demonstrates the stepwise excitation with two-photons where the first excited state (well-determined in energy) acts as the intermediate state. The width of energy levels adapted with permission from reference [1].

Moreover, for SPA and TPA processes the selection rules are different. Considering a molecule with an inversion center (centrosymmetric), the allowed excited-state for single-photon absorption S_1 cannot be populated directly via the TPA. In these situation the lowest available state for TPE has energy higher than that S_1 that also known as S_2 (see Figure 2.1). From this S_2 level, in few tens of picoseconds the molecular system relaxes to the lower

excited-state S_1 (in-direct population). This is the state from which the system undergoes either a radiative decay to the ground-state (fluorescence) or radiation-less processes like inter-system crossing and energy or electron transfer to a neighbor molecular system (categorize in the photo-chemical processes).

A state is called singlet S_n when it has spin zero. While, states with one pair parallel spin (spin quantum number is 1) are called as triplet states T_n. Aside from radiative transitions (e.g., fluorescence), there are three major radiation-less decays (see Figure 2.4) following the molecule photo-excitation: vibrational relaxation, internal conversion, and intersystem crossing. Vibrational relaxation is an ultrafast transition within vibrational single electronic bands. Internal conversion (e.g., $S_2 \rightarrow S_1$) stands for the transition between the states with a same multiplicity (iso-energetic process). Identical to the process of internal conversion, intersystem crossing refers to a transition (with low probability) between states with different multiplicity (e.g., $S_1 \rightarrow T_1$). Multiplicity demonstrates the possible spin quantum numbers. In general, after the photo-excitation of a molecule either via single-photon or multi-photon process, various routes are available for the de-excitation to the excitation species without changing the molecule chemistry, which are called the photo-physical phenomenon. The molecule is excited by a single or two photon absorption process from the singlet state S_0 to the S_1 (after the internal conversion), from this state the molecule can access with some low probability to the excited triplet state T_1. From the first excited singlet state, S_1, a competition take places where system could convert via radiation-less process of intersystem crossing $(S_1 \rightarrow T_1)$ to the triplet state or decay with a radiative process also known as the fluorescence, to the ground singlet state $(S_1 \rightarrow S_0)$. The triplet-state T_1 could relax with longer life-time radiation of photons (phosphorescence) with time-scales orders of magnitude lower than those of fluorescence $(T_1 \rightarrow S_0)$. Other possible effects like the self-quenching $(T_1 + S_0)$ and triplet-triplet annihilation $(T_1 + T_1)$ also all are consider as the photophysical actions of the molecular systems. Alternatively, when the molecule reach the excited states $(S_1$ or $T_1)$ via the aforementioned photophysical processes, a molecule could undergo, within a lifetime of the specific excited state, a chemical modification and chemical intermediate generation which are the primary activities of a process called photochemistry.

In centrosymmetric molecules, electronic transitions are exclusively allowed for single-photon and two-photon excitations (i.e, SPE & TPE), as discussed above. In the SPE regime, the selection rules are limited by a transition either from a gerade-state (a German term for even, means the wave-function's sign is not changed through an electron re-positioning) to an ungerade-state (a German term for odd, means the wave-function's sing is changed through an electron-repositioning) or vice versa. While this selection rule is completely different in TPE, where only transitions from the states of same parity are allowed (gerade to gerade or

ungerade to ungerade). For molecules with no inversion center, the selection rules are not so simply defined for the centrosymmetric molecules but depended on the symmetry of the molecule some states are not allowed to populate at the same quantum event with both excitation processes.
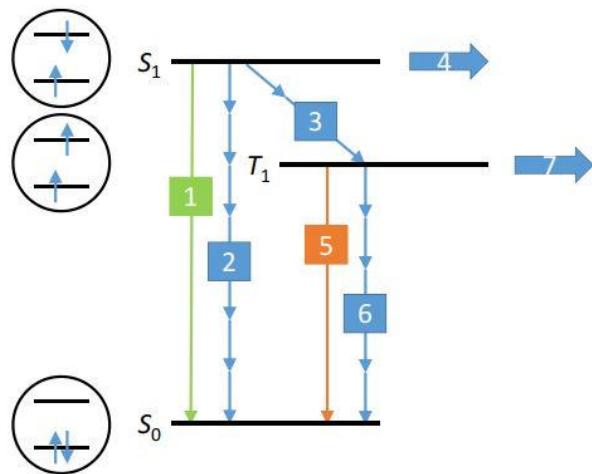

Figure 2.4. Diagram of photo-absorption, excitation, intersystem crossing, and decay processes. Routes #.1 depicts the radiative decay (fluorescence), #.2 is the non-radiative decay after a fast vibrational relaxation in S_1, #.3 non-radiative deactivation or in general the intersystem crossing, #.4 demonstrates the photo-reactive channel leading to the photoproducts, #.5 is the radiative deactivation or the phosphorescence process, #.6 non-radiative decay and another regime which also known as intersystem crossing, #.7 photo reactive channel and the photoproducts for bimolecular reactions. Adapted with permission from reference [3].

2.3. Gaussian beam profile

All the above phenomena requires high laser peak intensity (or irradiance). This can be achieved by using short pulses, possibly pre-chirped in order to compensate for the optics induces broadening, and by spatially focusing the beam. The two things are somehow in opposition since in order to more tightly focus, the beam needs more and more optical elements that induces a broadening in the pulse duration.

In laser physics, the intensity distribution of a laser beam is considered as Gaussian profile or better said, as a Gaussian-Lorentzian function. The time-independent Gaussian-Lorentzian beam intensity is a Gaussian in each plane perpendicular to the optical propagation axis along (z-axis) whose variance $w^2(z)$ describes with below formula as a function of various parameters.

$$w^2(z) = w_0^2 \left[1 + \left(\frac{\lambda z}{n\pi w_0^2}\right)^2\right] = w_0^2 \left(1 + \frac{z^2}{z_0^2}\right) \tag{2.19}$$

$$z_0 = \frac{n\pi w_0^2}{\lambda} \tag{2.20}$$

Here w_0 is the beam waist (beam radius at the focus, see Figure 2.5) and consequently $w(z)$ can be taken as the spot radius in a position along the propagation axis (z). The spatial conformation of the beam profile limits the maximum of the applied field in the position z with the factor of $1/e$ and $1/e^2$ for the intensity (regarding the propagation axis maximum value, usually in $z = 0$). The Rayleigh parameters also define the spread of the light distribution along the optical axis in non-linear excitation (also known as depth-of-focus, DOF). This parameter largely affect the possibility to perform laser stereo-lithography. The value of the diffraction limited $1/e^2$ radius depends on the wavelength and the numerical aperture as $\omega_0 = 0.61\lambda/N.A.$. This value reaches $\omega_0 \cong 0.4\,\mu m$ and Rayleigh range value of $\omega_0 \cong 0.8\,\mu m$ for a medium like water.

In single photon confocal excitation, on the contrary, the confocal parameters depend also on the size of the confocal pinhole. In far-field approximations (Fraunhofer region) the diffraction is described via Fourier transformations which preserves the Gaussian beam shape.
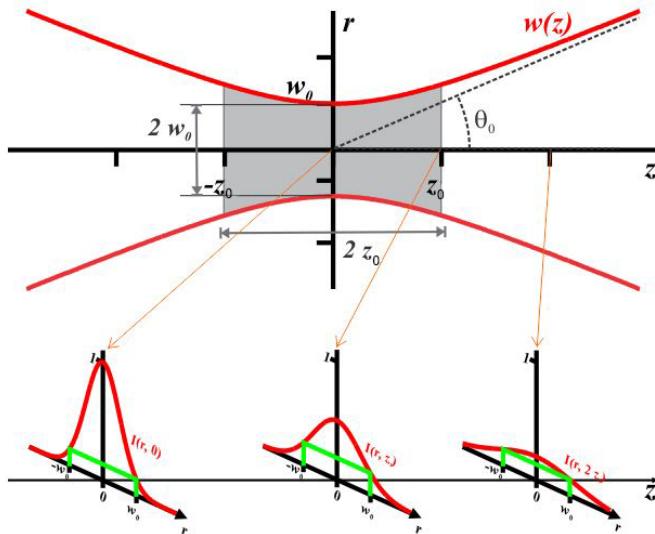

Figure 2.5. Schematic configuration of a Gaussian beam profile propagated along the axis z; w_0 is the beam-waist, z_0 is the on-axis distance of focal region from the central point (z=0), and θ_0 is the opening angle or beam divergence. The secondary plots demonstrate the beam intensity ($I(r,z)$) variation with respect to the distance from the beam central region (z=0). Adapted with permission from reference [6].

A similar situation happens when a Gaussian beam passes through an ideal lens. From all the considerations drawn above, here is possible to derive the optical intensity profile of a Gaussian beam that determines with formulation below.

$$I(r,z) = \frac{2P}{\pi w^2(z)} exp(\frac{-2r^2}{w(z)}) \tag{2.21}$$

In (2.21) P stands for the laser average power (W), and r stands for the couple of coordinates in the plane perpendicular to the optical axis, $r = (x, y)$.
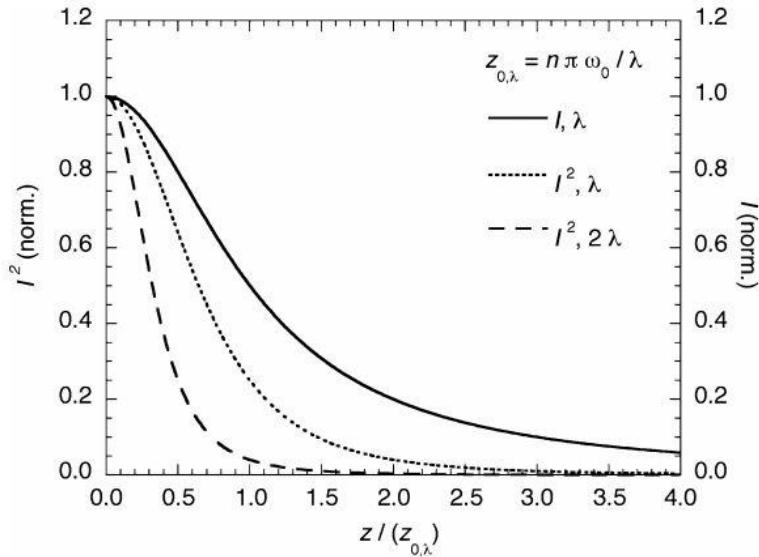

Figure 2.6. Behaviors of SPE and TPE along the beam propagation direction (z). Solid line represents the intensity of an on-axis Gaussian beam of wavelength λ and beam-waist w_0; dotted line shows the square of intensity of an –on axis Gaussian beam with wavelength λ and beam-waist w_0; dashed line is the square of intensity of an on-axis Gaussian beam with wavelength 2λ and beam-waist of w_0. Adapted with permission from reference [5]

The axial ($r = (0,0)$) intensity of a focused beam changes approximately (for $|z| > z_0$) as z^{-2}, where the z is the distance from the focal plane. However, the total power (the integral of the intensity over the r variable on each plane perpendicular to the optical axis), is constant and equal to the light power. This brings the acquisition of a blurred image of thick sample. However, since the TPA process is quadratic with the light intensity, therefore the rate of excited products in two-photon regime approximately changes with the factor of z^{-4} and, more important, the overall signal (photons per time) that comes from a plane at position z along the optical axis (i.e., the integration of the excitation rate over the r coordinate), still depends on z^{-2}. This is the origin of the intrinsic high spatial resolution for the two-photon process within the focal volume.

Contrary to the two-photon case, in SPE (linear excitation) the probability of excitation in a plane is independent of the z (even if the intensity drops along the axis- z). By simplifying the notations and considering a beam with a propagation direction in axis- z and the focal plane in $z = 0$, the propagation is described as that of the field emitted by a classical (non-Gaussian)

point source from which the beam diverges out with a radius R (rough estimation), within a cone whose half-angle tangent is $(a = \frac{\omega_0}{z_0} = \frac{\lambda}{\pi\omega_0})$.
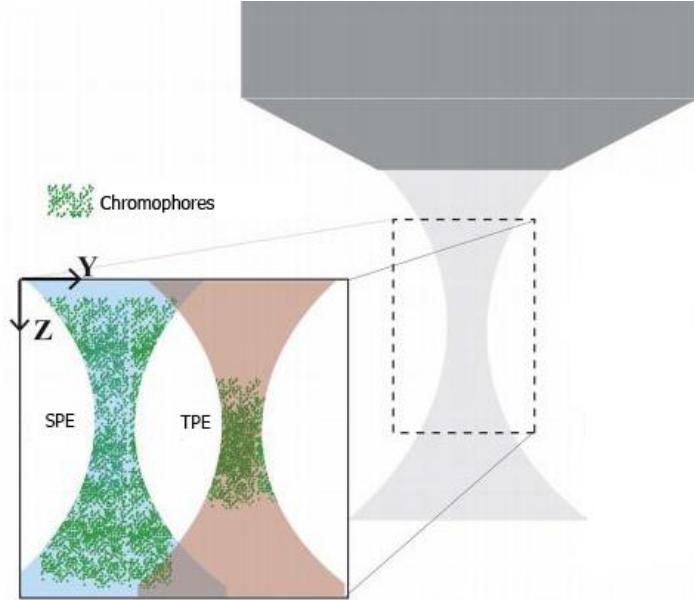

Figure 2.7. Schematic definition of the single-photon and two-photon focal region. Evaluating the imaginary volume of excited chromophores rising from single-photon and two-photon focalized beams; reproduced with permission from reference [4].

$$R(z) = w_0 + a|z| \tag{2.22}$$

Then from here, the beam intensity with respect to the laser power $\mathbb{P}_0$ is defined as below:

$$I(z) = \frac{\mathbb{P}_0}{\pi R^2(z)} = \frac{\mathbb{P}_0}{\pi(w_0+a|z|)^2} \tag{2.23}$$

In n-photon condition the formulation re-configure with $I^n(z)$ term.

$$I^n(z) = (\frac{\mathbb{P}_0}{\pi R^2(z)})^n = \frac{\mathbb{P}_0^n}{\pi^n(w_0+a|z|)^{2n}} \tag{2.24}$$

Supposing an illumination time of t_0 in the focal plane, the illumination time within the z-axis is t.

$$t(z) = \pi(w_0 + a|z|)^2 t_0 \tag{2.25}$$

Thus, finally the effective intensity within a t window of illumination is constructed as:

$$t(z)I^n(z) = \frac{t_0\mathbb{P}_0^n}{\pi^{n-1}(w_0+a|z|)^{2n-2}} \tag{2.26}$$

This equation (which is a rough estimation) claims that in single-photon process (n=1), the effect will be independent of z positioning, Figure 2.7.

2.4. References

[1] Neckers, D. C., Jenks, W. S., & Wolff, T. (2006). *Advances in photochemistry*. John Wiley & Sons.

[2] Stampfl, J., Liska, R., & Ovsianikov, A. (2016). *Multiphoton lithography: Techniques, materials, and applications*. John Wiley & Sons.

[3] Lee, W., McMenamin, T. and Li, Y., 2018. Optical toolkits for in vivo deep tissue laser scanning microscopy: a primer. *Journal of Optics*, 20(6), p.063002.

[4] Rubart, M., 2004. Two-Photon Microscopy of Cells and Tissue. *Circulation Research*, 95(12), pp.1154-1166.

[5] Marder, S. and Barlow, S., 2008. *Photoresponsive Polymers*. Berlin: Springer.

[6] Openspim.org. 2020. *SPIM Optics 101/Theoretical Basics - Openspim*. [Online]

[7] Bhawalkar, J. D., He, G. S., & Prasad, P. N. (1997). Nonlinear multiphoton processes in organic and polymeric materials. *Reports on Progress in Physics*, *60*(6), 689-689.

[8] Sipe, J. E., & Boyd, R. W. (1992). Nonlinear susceptibility of composite optical materials in the Maxwell Garnett model. *Physical Review A*, *46*(3), 1614-1629.

[9] Zavelani-Rossi, M., Polli, D., Kochtcheev, S., Baudrion, A., Béal, J., Kumar, V., Molotokaite, E., Marangoni, M., Longhi, S., Cerullo, G., Adam, P., & Della Valle, G. (2015). Transient optical response of a single gold Nanoantenna: The role of Plasmon detuning. *ACS Photonics*, *2*(4), 521-529.

[10] Biagioni, P., Celebrano, M., Savoini, M., Grancini, G., Brida, D., Mátéfi-Tempfli, S., Mátéfi-Tempfli, M., Duò, L., Hecht, B., Cerullo, G., & Finazzi, M. (2009). Dependence of the two-photon photoluminescence yield of gold nanostructures on the laser pulse duration. *Physical Review B*, *80*(4).

[11] Zhang, J. (2017). Research on experimental accuracy of laser Z-scan technology.

[12] Singh, V., & Aghamkar, P. (2015). Z-scan: A simple technique for determination of third-order optical nonlinearity.

Chapter 3.

Principles of two-photon polymerization/crosslinking

3.1. Photo-initiation

When a beam of monochromatic light passes through a sample of a homogeneous medium of thickness l, a fraction of the energy of the light is absorbed by the medium according to the Lambert-Beer-Bouguer's law (extensively known as Lambert-Beer's law). This law of physics explains the fact that the relative amount of absorbed light is independent of the intensity I of the incident light while the intensity reduces by a factor that is exponentially related to the thickness of the absorbing medium. In another word, the amount of absorbed light is proportional to the absorbing centers (concentration of the absorbance molecules), Beer's law. The Lambert-Beer's formulation combines these observations as it follows:

$$\frac{dI}{dl} = \varepsilon C I \qquad (3.1)$$

Here ε is called the molecular extinction coefficient ($mol^{-1}cm^{-1}$), and C is molar concentration.

The class of materials, either organic, in-organic, biological, or synthetic, that undergo chemical or physical modifications induced by light irradiation are called photo-responsive systems. Light, as a spatio-temporal tunable external stimulus, interacts with specific parts in the photo-responsive system known as photo-active group(s). Following the light absorption of various photon multiplicity, these photo-active moieties undergo a molecular reactions while at the excited state. As seen in Ch. 2, by focusing narrow width laser pulses by means of high numerical aperture optics, we can induce a substantial fraction of photo-active molecules to simultaneously absorb multiple photons and be excited to the upper available energy states. The kind of photochemical reaction does not depend to a large degree, on the multiplicity degree of the absorption since the molecule decay to the lowest excited state within few tens of picoseconds. However, multiphoton excitation brings the huge advantage to allow 3D confinement of the photoactivation process.

Upon multi-photon excitation several photochemical reactions can be initiated; photo-isomerization, cyclo-addition, singlet-oxygen generation, intermolecular charge transfer, intramolecular charge transfer, and bond cleavage. To this purpose, understanding the chemical properties of photo-responsive molecules (photochemistry) is a crucial step towards the assessment of the details of the photo-dynamic pathways. Fundamentally, an electronic state of a molecule is identified by its molecular orbitals (MO) and the energy levels. These molecular orbitals built up from atomic orbitals (AOs). In a molecule, the hybridization of the AOs define the coupling principles in chemical bonding of atoms. Considering a situation when there is an identical orbital across a binding (e.g., C-C), these configurations are known as symmetric couplings, while an un-identical orbitals (e.g., C-O) give asymmetric couplings. In the latter case, the difference in electron density of each atom makes the bonding polarized,

which in consequence results in a partial charge δ in the whole molecule and a permanent dipole moment.

Coupling the electronic point of view with spins, the Pauli's orbitals principle tells that in a singlet state, S_n, the atomic orbitals host only paired electrons (opposite spins) and the spatial wave-function is symmetric. On the contrary, in triplet states T_n the spins are parallel and the spatial wave-function is anti-symmetric, corresponding to a lower energy. Stepping up to describe the molecular orbitals, the bonds are categorized according to the symmetry with respect to the bond axis. In most of the organic molecules, the inter-molecular bonding forms as π and σ bonding and/or anti-bonding ($\pi*$ and $\sigma*$). As the name says, chromophores are molecules that present extensive absorption or electromagnetic radiation with spectral components that fall in various parts of the UV-Vis-NIR spectrum depending on the particular chemical moiety (e.g., carbonyl, nitro group, or aromatic rings). Many aromatic molecules of medium size (pirrole, Flavin or their combination) absorb light in the ultraviolet (UV) to near-infrared (NIR) range of the electromagnetic spectrum and jump on an excited state whose lifetime is typically in the range of nanoseconds. Following this, the molecule can undergo a series of processes as discussed in Ch.2. However, the interest in the present project is the chemical reactions that can occur in the molecule while at its excited state.

3.1.1. Light-induced polymerization/crosslinking process

The Initiation process in a photo-activation mechanism (e.g., photo polymerization/crosslinking) is triggered by the decomposition of photo-responsive molecule (also called initiator or photo-initiator). The decomposed photo-initiating species most often are free radicals able to react with the monomer/oligomer units building up macromolecules or with polymers, thereby leading to the formation of a polymeric or supramolecular network. This photochemical reaction that proceeds by chain propagations and then terminations, results in the formation of polymers or crosslinked networks, known as photo-polymerization/crosslinking products. Photo-polymerization refers to a concept where the photochemical-reaction is initiated by the one or multi-photon absorption of light by one initiating species and in the subsequent reactions by interaction of this activated unit with other units, in a propagation that generates the backbone of polymeric chains.

In some photo-polymerization condition, each monomer may be composed of several moieties (e.g., proteins) which show ability to undergo the propagation process not being limited to the two ends, therefore side-chain reactions or propagations are allowed for these kind of systems. In these cases, the crosslinking process results in the generation of the branched polymers with size much larger than the single polymeric chain. The propagation of the branched polymers that follows the crosslinking basic reaction, leads to a macroscopic

network called the gel. The photo-crosslinking procedure, unlike the photo-polymerization, has propagation and termination reactions limited between nearest neighbors. Like all other crosslinking routes, the light-induced-crosslinking (photo-cross-linking) results in gelation of the medium. An important factor during this process is the gelation extension which closely relates to the quantity of the functional groups existing in the medium.

Most monomers or oligomers, depending on their chemical structures and properties, have limited sensitivity to the available light sources. There are exceptions, like commercially available (designed specifically for an exclusive application) and biological-based materials like proteins whose aromatic amino acids are remarkably sensitive to light. Monomers and oligomers as the building blocks of the final polymerized/crosslinked materials, differs in the quantity of their reactive functional groups and their structures. Monomers are small molecules containing one or several functional groups while oligomers are larger molecules with repetitive structure units hosting several functional groups. In all cases, in order to increase the photo-activation efficiency, presence of highly-responsive molecule(s) (PI) is necessary. In general, upon the exposure of the PI molecule(s) to light with sufficient intensity and appropriate wavelength, depending on its nature and molecular structure, different initiating species are expected to be produced: free radicals, cations (acids), and anions (bases).

$$I \xrightarrow{k_d} 2R\cdot \quad\}\!\!- \text{ decomposition}$$

$$R\cdot + M \xrightarrow{k_i} RM_1\cdot \quad\}\!\!- \text{ initiation}$$

$$RM_1\cdot + M \xrightarrow{k_p} RM_2\cdot$$

$$RM_2\cdot + M \xrightarrow{k_p} RM_3\cdot$$

$$RM_3\cdot + M \xrightarrow{k_p} RM_4\cdot$$

$$\cdot$$
$$\cdot$$
$$\cdot$$
$$\cdot$$

$$\left.\begin{array}{l} \\ \\ \\ \\ \\ \\ \end{array}\right\} \text{ Propagation}$$

$$RM_{(n-1)}\cdot + M \xrightarrow{k_p} RM_n\cdot$$

$$RM_n\cdot + RM\cdot \xrightarrow{k_t} dead\ polymer \quad\}\!\!- \text{ termination}$$
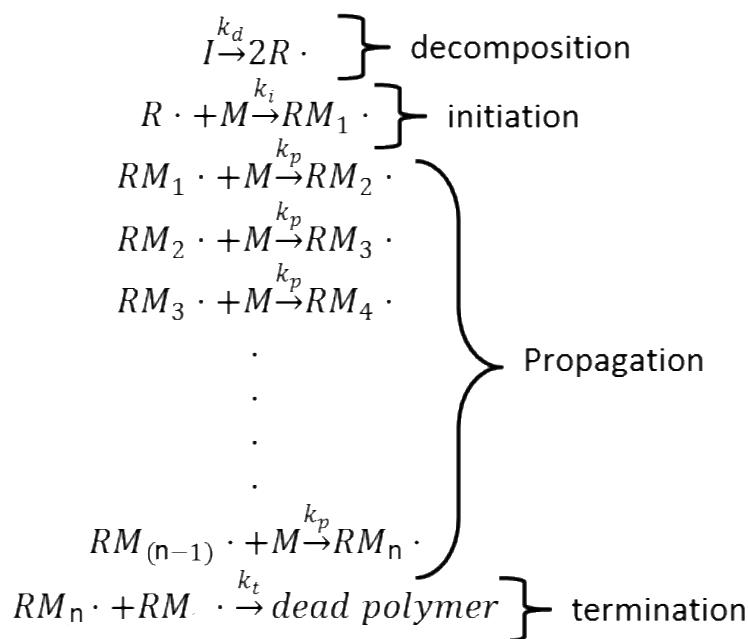
Figure 3.1. Simplified demonstration of free radical polymerization kinetics. Reconfigured from reference [7].

Free radical polymerization/crosslinking consists of four consecutive major steps (Figure 3.1); initiation, propagation, termination, and chain transfer (gelation extension in crosslinking regime), Figure 1. The initiation itself consists of two steps, first is the decomposition of the initiator molecule I into two radicals $2R°$ and the second is the initial reaction of radicals with

the monomer/oligomer M. The rate of decomposition step k_{dec} is considered as an effective factor in the initiation ratio (usually between 10^{-1} to 10^{-6} s^{-1}).

$$I \overset{k_{dec}}{\to} 2R°$$

(3.2)

$$R° + M \overset{k_i}{\to} M_1°$$
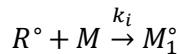
Here k_i is the rate constant of the process that, within initiation, brings to the formation of the monomer-ended-radical[1] $M_1°$. The rate of radical generation can then be expressed as the following equation (3.3):

$$\frac{d[R°]}{dt} = 2k_{dec}.[I]$$

(3.3)

From equation (3.2), the rate of monomer-ended-radical generation $R_i°$ is given by and f as the photo-initiation efficiency:

$$R_i° = 2fk_{dec}.[I]$$

(3.4)

The second step plays crucial role in the kinetic of photo-polymerization/crosslinking that is called monomer additions:

$$M_n° + M \to M_{n+1}°$$

(3.5)
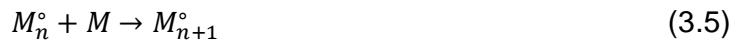
Where $M_n°$ is the sequential generated monomer-ended-radical (e.g., for $n = 1; M_1° + M \to M_2°$). The formulation in (3.5) represents the bimolecular reaction that is the basis of the propagation process. The propagation proceed by joining the already generated radicals with available monomers producing macromolecules species containing active end-groups (monomer ended radicals). The rate constant of the propagation process k_p following the bimolecular reaction is a second-order constant with units of (concentration)$^{-1}$.(time)$^{-1}$. Hence, the propagation rate can be written as the equation reported hereafter:

$$R_p = k_p.[M].[M°]$$

(3.6)

This equation shows that the reaction proceeds with a rate that depends on the concentration of the "monomer" units and the rate of formation of the free radicals that depends on the light properties and the PI efficiency. It is important to consider that the rate of propagation not only depends on the chemical structure of the monomers and radicals active sites but also relates to the local temperature and the viscosity of the matrix which implies an important relation

---

[1] Here in a general, a monomer-ended radical fragment is depicted by the term $M°$

between propagation of pre- polymers entities (polymer backbone), and the medium diffusivity.

As for the termination step that involves the reaction of monomer-radicals end chains, two different types of processes may take places: combination and disproportionation. The combination[2] is a process in which, through a final reaction of the monomer-radical, a single and ultimate polymer chain is generated, called a dead polymer-chain. On the other hand, in the disproportionation path[3] (Figure 3.2), as the result of the direct mutual interaction of two monomer-radical species, one end abstracts hydrogen from the other producing one ultimate polymer chain and another chain carrying a double-bond functionality, Figure 3.2. The lateral active polymer chain undergoes further polymerization to reach the ultimate stage. Like the propagation step, the termination reaction is controlled via the diffusivity of the monomer-radicals through the medium. This dependency is further worsen by the fact that in parallel to the chain growth and monomers-polymer conversions the viscosity of medium increases.
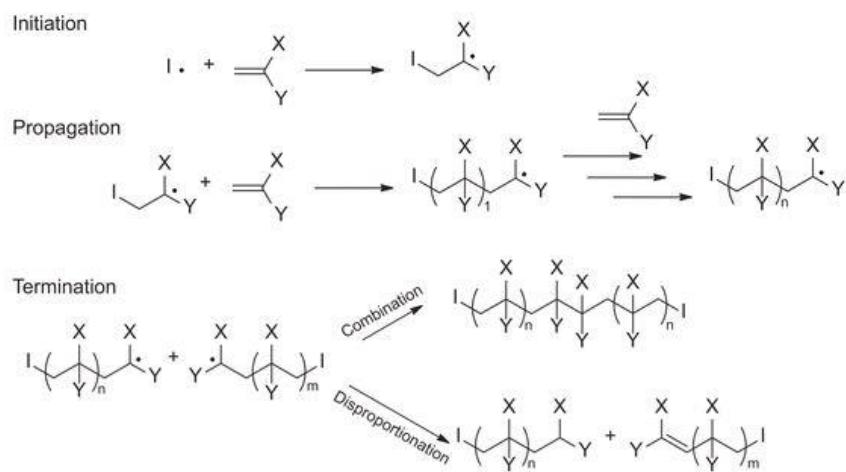
Figure 3.2. A schematic overview of the general radical polymerization, from the initiation step to the termination.

Because of this phenomenon, the polymerization/crosslinking rate in a medium may drop with time. The termination rate constant k_t scales as a second-order kinetic with the $M°$ concentration.

$$R_t = 2k_t.[M°]^2 \tag{3.7}$$

The rate of the whole process can be determined from the consumption of monomers in the polymerization/crosslinking. Hence, the rate of polymerization/crosslinking process follows

---

[2] Termination by combination $M_X° + M_Y° \rightarrow M_{(X+Y)}$
[3] Termination by disproportionation $M_X° + M_Y° \rightarrow M_X + M_Y$

$\frac{d[M]}{dt}$ with a negative sign (i.e., $-\frac{d[M]}{dt}$). In the steady-state condition, the rate of initiation process R_i° must be equal to the rate of termination process R_t. This assumption gives:

$$2fk_{dec}.[I] = 2k_t.[M^\circ]^2 \tag{3.8}$$

From equation (3.7) one can find is the concentration of the monomer-ended-radicals:

$$[M^\circ] = (fk_{dec}.[I]/k_t)^{1/2} \tag{3.9}$$

By identifying the processes in which the monomer concentration involve (i.e., initiation and propagation), the rate of polymerization/crosslinking can be written as:

$$-\frac{d[M]}{dt} = R_p + R_i^\circ \tag{3.10}$$

The equation (3.9) reduces to $-\frac{d[M]}{dt} = R_p$ because the influence of monomer concentration in the initiation process is negligible. By merging equations (3.6) and (3.9) the rate of polymerization/crosslinking:

$$-\frac{d[M]}{dt} = R_p = k_p.[M].[M^\circ] \tag{3.11}$$

$$-\frac{d[M]}{dt} = (k_p/k_t^{\frac{1}{2}})\,[M]\,R_{M^o}^{1/2}$$

The equation (3.11) is a differential equation in moles of monomer per unit volume per unit time (here $[M]$ and $[I]$ are respectively the monomer and initiator concentrations, and the R_{M^o} is the rate of formation of monomer-ended radical). In the final step of the radical-based photo-polymerization/crosslinking, so-called the chain transfer, maximal molecular weight of the polymerized/crosslinked system will be obtained. While unlike the termination process the radical concentration remains constant, the already grown monomer-radical chain is going to be able to transfer the functionality to other host monomer-radical chain producing a new monomer-radical chain $R^\circ M_{n-1}^\circ M^\circ$. This reactivated chain forms via the hydrogen abstraction of the host chain via the functional activity of the primary monomer-radical chain. The result will be a dead polymer chain and a newly activated chain capable of re-initiating the polymerization/crosslinking. Since the radical could be accepted by any species in the medium (i.e., monomer, solvent, initiator), the chain transfer mechanism occurs in random and out of any time-scale-based rates.

A normal solution-based medium for the photo-polymerization/crosslinking consists of a solvent, an initiator, and a monomer/oligomer compartment. In more complex media, in order to increase the efficiency of the photo-induced chain grow process, the addition of a co-initiator or a photo-sensitizer is usually adopted. Co-initiators are molecular compounds with a

minimum participation in the light absorption process. The presence of this compound in the medium helps only in the generation of the initiating species by reacting with the excited photo-initiator molecules. On the contrary, photosensitizers play an important role in the light absorption process. The variety of these compounds, from quantum-dots to natural pigments and dyes, aligned with their highly variable visible-band absorption spectra, makes the use of these compounds widespread in the field of photochemistry. The photosensitizers act as the light-harvesting antennas, absorbing light, being excited mostly to triplet states, and then transferring the excitation to the photo-initiator molecule. There are two available routes for the photosensitizer to pass the excitation to another molecule, either through energy transfer or electron transfer. The energy transfer phenomenon is much more probable to occur because of independency of this procedure to electrically match donor and acceptor molecular sites that are necessary for electron transfer, in addition to the compound physical/chemical structure and properties.

Coming back to the free radical formation, the main processes responsible for the generation of radicals from the photo-excitation of an initiator compound are classified as Homolytic Cleavage, and Hydrogen Transfer. The Homolytic Cleavage, or homolysis, refers to a chemical modification wherein the molecule cleaves (scission or splitting of bonds) in two or more fragments. During the photo-initiation cycle, the absorbed energy of photon(s) leads the excited initiator molecule. In this excited state, the covalent bond of the initiator molecule splits (cleaved) by dividing two electrons equally associated to the two ends. This procedure leads to cleavage of a molecule to two radicals. On the Hydrogen Transfer route, the hydrogen transfer itself may proceed in two different ways mainly controlled either by the hydrogen-acceptor (HA) or the hydrogen-donor (HD) moieties. In the case when the photo-initiator molecule sits near a HD, the photo-initiator abstracts a hydrogen from the donor with the generation of two radicals, a hydrogenated photo-initiator and a radical donor. In the case when a HA interacts with a photo-initiator, a charge transfer occurs in which the HA acts as an electron donor or a proton acceptor and, similarly to the former process, two radicals are generated. In all cases, the energy or charge transfers of the photoinitiator, the initiator molecule typically sits on its first excited-triplet state (T_1).

3.1.2. Singlet oxygen

It is worth mentioning that the above-mentioned light-matter interaction can lead to an additional process, particularly relevant in the biomedical field: single oxygen formation. This is actually among the most noteworthy applications of the multi-photon absorption phenomenon, known in the literature as multi-photon photodynamic therapy. The basis for this therapy is the use of two-photon absorption to generate singlet oxygen that has a marked

cytotoxic effect: being the multiphoton process highly confined spatially, this photo-dynamic therapy can be used to selectively treat cancer cells.

The molecular oxygen unlike many natural molecules in its ground state has triplet multiplicity $O_2(^3\sum_g-)$ that lies $94.2\ kJ.mol^{-1}$ below the lowest excited state which has singlet multiplicity $O_2(^1\Delta_g)$. Typically the generation of singlet oxygen in photo-responsive mediums occurs via energy transfer from the lowest triplet excited state of a dye T_1 to the singlet ground state $O_2(^1\Delta_g)$ of the oxygen molecule (O_2) and, if the transferred energy overcomes the excitation energy of $94.2\ kJ.mol^{-1}$, the $O_2(^1\Delta_g)$ state will be populated leading to the singlet oxygen.

In radical photo-polymerization/crosslinking there are different ways where the singlet oxygen intervenes with the process. In type-I radical photo-polymerization/crosslinking (Homolytic cleavage), as discussed earlier, from the direct interaction of excited photo-initiator molecule (T_1) with a monomer a primary radical (R) is created which, through a chain reaction, could produce a second radical (R') with the possibility to interact with the first radical or the triplet oxygen (Figure 3.3). In type-II (Hydrogen transfer), the interaction of photo-initiator molecule at its excited triplet state (T_1) directly with the oxygen molecule produces singlet oxygen. Since the type-II photo-initiation (hydrogen transfer) is basically a bimolecular reaction, the effect of generated singlet oxygen in this route is limited. The reaction of singlet oxygen with generated radicals during initiating and propagation steps promote formation of peroxy radicals ($R'OO\circ$) in a rate approximately 10^6 times slower than the propagation rate. Although this procedure reduces the efficiency of the normal polymerization/crosslinking pathway, it can also promote indirect polymerization/crosslinking processes by producing initiating the above mentioned peroxy radicals through hydrogen abstraction from any fragment (i.e., monomer, monomer chains, solvent molecules and etc.) and forming hydroperoxides which further results in donor radicals ($D\circ$). This process last till the oxygen concentration drops through surface evaporation or primary radical generation in the medium, Figures 3.3 and 3.4.

Therefore in laser-based additive manufacturing, the presence of excited oxygen molecule(s) should be avoided or minimized due to its detrimental effects on the chain length propagation, and on the polymerization rate. In addition, on laser fabricated structures to be used in the biomedical fields for applications like tissue engineering of cell differentiation stimulation, the singlet oxygen formation should be limited in order to mitigate any possible toxic effect on the living-system functionalities. In these cases, there are numerous ways to prevent this unwanted reaction such as employment of oxygen inhibitors in the photo-polymerization/crosslinking resins. On the contrary, to apply the laser fabricated structures for therapeutic treatments, like photo-dynamic therapy for cancer or for antibacterial treatments, the presence of this highly reactive species (reactive oxygen species: ROS) is to be promoted

in order to obtain an efficient radical generation during the radical-based photo-polymerization/crosslinking, Figure 3.3. In such cases, the photo-initiator trapped within the developed gel matrix or any additional compound, like nanoparticles as it is demonstrated further in this project, is to be preferred.
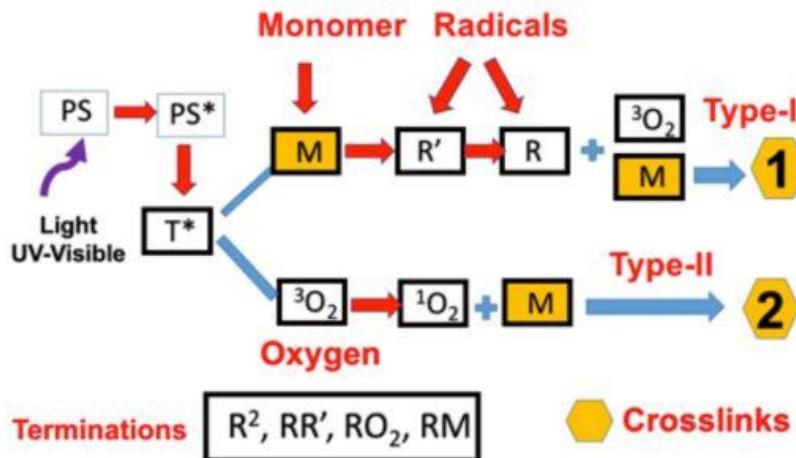

Figure 3.3. Schematic of photochemical pathways leading crosslinking of monomers; absorption of photons by photosensitizer (PS) molecule results in molecular excitation (PS*) follows by the electrons intersystem crossing toward the excited triplet-state (T*). From this point, the excitation could pave two different routes in reaching the final crosslinking condition. The type-I route also known as the radical-mediated crosslinking, and type-II is called oxygen-mediated crosslinking. Adapted with permission from reference [3].
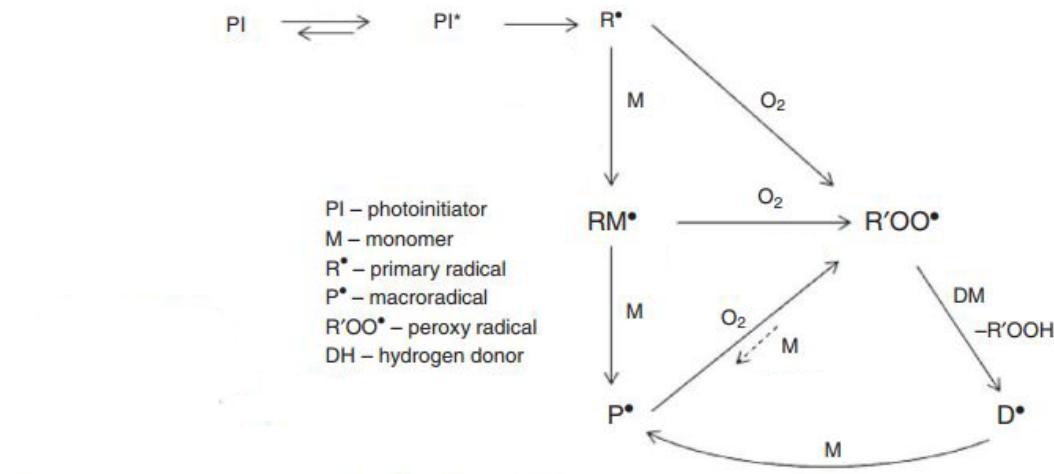
Figure 3.4. Schematic diagram of both radical-mediated and oxygen-mediated routes with emphasize on the rule of oxygen molecule in generating macroradicals (P*). Reconstructed with permission from reference [4]

3.1.3. Diffusion and viscosity controlled photo-polymerization/crosslinking

One factor that controls the kinetics of photo-induced polymerization/crosslinking is the diffusion of the species in the resin/ink. Initiation, propagation and termination depend all on viscosity. However, the termination step has a marked dependency from the very beginning of the laser writing process. The termination coefficient k_t (a chain-related-process) of the polymerization/crosslinking process, enters many of the reaction rates discussed above and can affect the writing process in many ways. It is dominated by a time-scaled functional fragmentation reactions (e.g., radicals formation) that is described by the diffusion rate coefficient (k_{dif}), and k_{dif} itself depends on properties of the resin/ink, most importantly on the viscosity. Due to the relevance of the termination process in the extension of the cross-linked network, viscosity affects the final efficiency of polymerization/crosslinking process from the very beginning. From the Stokes-Einstein and Smoluchowski equations [5], the relation between the diffusion rate coefficient and the viscosity convolves as below:

$$k_{dif} = \frac{8000\ \mathbb{R}T}{3\eta} \tag{3.12}$$

Where $\mathbb{R}$ is the gas constant (J/mol/K), T is the temperature (K), and the η is the viscosity ($Pa.s$). All the introduced polymerization/crosslinking steps are in a way depend on the diffusion. However, the termination reaction is influenced more by the diffusion or the viscosity from very beginning of the process. The termination coefficient k_t is proportional to the diffusion coefficient k_{dif} (dm³/mol/s), and therefore displays a reciprocal relation with the viscosity ($k_t \propto \eta^{-1}$). The result of this relation helps in understanding the dependency of the polymerization/crosslinking on viscosity. In fact, in higher viscosity inks the diffusion coefficient and the termination rate are low leading to higher and more efficient polymerization/crosslinking rate. However, the above model of the trend of polymerization/crosslinking upon the ink viscosity is not valid when the viscosity of the cross-linking environment is too high, because in such cases also the initiation and propagation steps start depending on the viscosity. In modeling the relation between viscosity/diffusion coefficient and the polymerization/crosslinking rate, there is at least another mechanism-based-coefficient known as addition step. The addition is a step of the propagation of the polymerization/crosslinking, in which a diffusing reactive monomer-radical fragment meets another free monomer. It is described by the addition coefficient rate k_{add}, whose dependence on the ink viscosity is not strong, at least for low values of the viscosity. In theory, when there is a balance between the diffusion coefficient and the addition rate coefficient ($k_{dif} \approx k_{add}$) the highest polymerization/crosslinking rate, R_p, occurs. Strong inequalities, either ($k_{dif} \gg k_{add}$) or ($k_{dif} \ll k_{add}$), of these two factors determines a drop of a polymerization/crosslinking rate (see Figure 3.5). In principle, starting from the initial steps of the photopolymerization/crosslinking

the condition follows $k_{dif} > k_{add}$, when the rate R_p increases. As the cross-linking proceeds, the local viscosity increases and we reach a maximum value of R_p when $k_{dif} \approx k_{add}$. Finally, as the cross-linking proceeds even further to the condition in which $k_{dif} < k_{add}$, the polymerization/crosslinking rate, R_p, drops. For details see Figure 3.5.
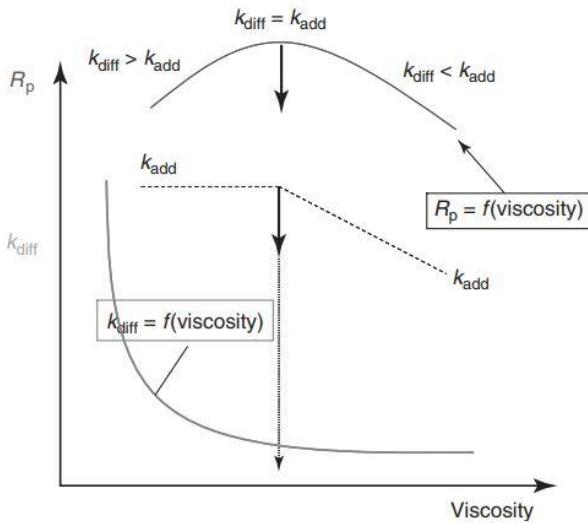

Figure 3.5. Diagram of crosslinking/polymerization rate (R_p) with respect to the viscosity evolution. The viscosity labeled axis also depicts the process from the beginning (low viscosity) to the end (higher viscosity) and demonstrating the efficient margin of crosslinking/polymerization ($k_{dif} \approx k_{add}$). Adapted with permission from reference [9].

3.1.4. Threshold dose in radical formation upon photo-crosslinking

As discussed earlier, from the material science point of view, the photo-polymerization/crosslinking can be described as a phenomenon in which part of the photoresist that is a liquid that we have also called ink, loses its solubility upon light exposure and forms a micro-volume of condensed (soft) matter. This is the basic definition of a negative-tone photoresist or ink, where the solubility of monomers or oligomers reduces in time under light irradiation due to compartments crosslinking. In the multiphoton fabrication regime, the linking of photoresist monomers, which is the building block of photo-crosslinking/polymerization, occurs either via generation of free radicals or cations. As discussed earlier, the photoresist/ink generally consists of two main components, the monomer/oligomers and the photo-responsive molecules. In the systems where the generation of free radicals take the lead in photo-crosslinking, the photo-responsive component is called photoinitiator (PI), while if the photo-crosslinking is promoted by cations, the photo-responsive component is called photoacid generator (PAG). This thesis focuses on the radical polymerization arising from the photoinitiation process induced by a PI. Similar to radical-chain reactions, the radical polymerization itself can take two different routes that directly depend on the PI molecules. In

the first route, which pertains to the Norish Type-I PIs, the molecular photoexcitation leads to intersystem crossing. Upon each intersystem crossing, a triplet di-radical is generated (mostly centered on the carbonyl group) which after a homolytic bond cleavage process, creates two free radicals. In the second route, which pertains to the (intramolecular hydrogen abstraction) Norish Type-II PIs, reactive free radicals (including singlet oxygen) will be directly generated without passing through a triplet state. Since in both cases the excitation of the PI is required, multi-photo-induced radical cross-linking/polymerization largely depends on the PI multiphoton absorption cross-section, which should be high, on the quantum efficiency, which should be low, and on the initiation rate that controls the first step of the cross-linking/polymerization. Activating molecules with large multiphoton absorption cross-section or, more specifically for this thesis, large two-photon absorption (TPA) cross-sections are much more effective in promoting polymerization/crosslinking. However, even in photo-responsive systems containing PIs with large TPA cross-section, the initiation process can be triggered via a non-Norish based mechanism like electron transfer. Hence, for an efficient photo-polymerization/crosslinking approach the PI should present not only high TPA absorption cross-section but also a high photovoltaic quantum efficiency.

As a direct consequence of the photo-initiation and radical generation, many radical monomer clusters are formed inside the excitation volume. The reaction of these radicals with a free monomer propagates (by one step) the cross-linked network. Aside from this crucial on-going radical generation, two other factors or processes affect the propagation rate, quenching and the termination. Through the quenching process, the generated radicals interact with oxygen molecule or any other radical inhibitors and partially lose the reactivity, while in the already discussed termination process two reactive species meet each other annihilating the radicals they carry. These two processes along with the laser intensity and the exposure time, determine the excitation volume or the voxel.

As discussed earlier, the photo-polymerization/crosslinking basically stems from insolubilizing a volume of photoresist by exposing it to light. The relation between solubility and exposure dose is highly non-linear and shows up in the existence of an exposure threshold which is defined as the minimum dose for which polymerization/crosslinking (i.e., insolubilizing) occurs. Mathematically, a threshold model can be derived for the exposure dose D that scales as:

$$D \sim t f_R E_p^n \tag{3.13}$$

Here t is the exposure (illumination) time, f_R is the repetition rate of the laser source, E_p is the peak power, and n (>1) arises from the nonlinearity of the absorption process, and it should be close to the number of absorbed photons in each quantum event. Therefore, the threshold

peak power as a function of the exposure time and the laser repetition rate can be derived from a log-log plot, Figure 3.6:

$$\log\left(E_{p,threshold}\right) = -n\log\left(\frac{tf_R}{D_{threshold}}\right) + c \qquad (3.114)$$
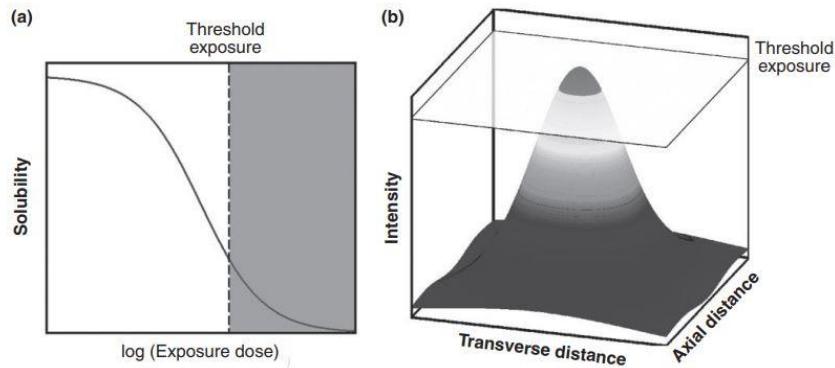

Figure 3.6. Schematic presentation of threshold boundary in relation with intensity and solubility; (a) demonstration of the threshold boundary upon decreasing the solubility in the function of logarithmic exposure dose, (b) the spatial conformation of intensity profile of TPE via employing a Gaussian laser beam. Adapted with permission from reference [4].

In a two-photon regime one expects is $(I) \sim I^2$ since E_p scales as the spatial laser intensity profile, $I(\vec{x}) = I_0 f(\vec{x})$, where I_0 is the maximum of the intensity. The polymerization/crosslinking only occurs if $D \geq D_{threshold}$, or, due to the relation between the exposure dose and laser intensity, only if $(\vec{x}) \geq I_{threshold}$. From spatial point of view, the latter relation determines the cross-linking voxel size: $(\vec{x}) \geq I_{threshold}/I_0$. In this relation, the line/structure shape and width solely relate to the spatial intensity profile (x) not the absorption rate.

Due to the spatial profile of the light source (i.e, Gaussian laser beam) intensity, the degree of two-photon polymerization/crosslinking decreases from interior volume of the voxel toward the exterior boundaries. This spatial dependence of the monomer to polymer conversion efficiency has a role in determining not only the minimum laser writing spacing but also the physical and mechanical properties of the final structure. By employing high overlapping of voxels during the polymerization process, structures with higher Young's modulus in comparison with patterns and structures fabricated with low voxels overlapping can be generated.

3.2. Laser optics and Microfabrication

To step into sub-micron-scale structures laser fabrication, accurate instrumentations are required, from an ultrafast pulsing laser source well-aligned on the optical path to a microscope setup equipped with a scanning device. We will consider in detail the main feature of the laser propagation here. For a fabrication methods that exploits highly focused laser beams, the axial writing resolutions in the optical axis direction, δz, and in the focal plane, δr – the factors that directly determine the finesse of the fabricated micro-structures - arise almost exclusively from the laser working wavelength and the microscope objective features:

$$z = 2\frac{n\lambda}{(N.A)^2} \tag{3.15}$$

$$r = 0.61\frac{\lambda}{N.A} \tag{3.16}$$

From equations (3.15) and (3.16) it is obvious that the resolution of a microstructure is limited by some factors, most importantly the wavelength of fabrication λ and the numerical aperture $N.A$ of the objective mounted on the microscope. On the contrary of the radial parameter that is not related to the refractive index n, the axial resolution is directly proportional to the n of the medium which the laser passes through for the micro-fabrication.

A laser beam propagates as a Gaussian-Lorentzian function in the lowest transverse mode (TEM_{00}) plane. Pivotal properties that describe propagation of an ideal Gaussian beam in three dimensions through the medium/ink are the beam spot size and the depth of focus (DOF). These, together, determine how the intensity profile changes along the irradiation direction. As described in the previous chapter (section. 2.3) the intensity profile of a Gaussian beam follows the equation below:

$$I(R,z) = \frac{2P}{\pi w^2(z)} exp(\frac{-2R^2}{w(z)}) \tag{3.17}$$

$$w^2(z) = w_0^2[1 + (\frac{\lambda z}{n\pi w_0^2})^2] = w_0^2(1 + \frac{z^2}{z_0^2}) \tag{3.18}$$

$$z_0 = \frac{n\pi\omega_0^2}{\lambda} \tag{3.19}$$

Where P is the average power which is also proportional to the I_0. The R stands for the transverse radius, and z is the propagation axis. w_0 defines the beam waist or the minimal focal spot size, z_0 is the Rayleigh range ($2z_0$ is the DOF). In the beam waist plane ($z = 0$) the Gaussian applied electric field drops at $R = w_0$ by a factor of $1/e$ from its maximum, and subsequently the intensity drops by the factor of $1/e^2$ from its maximum value. Along the optical axis, instead, the intensity drops by a factor 2 when $z = z_0$:

$$I(0,z) = \frac{I_0}{1 + (\frac{z}{z_0})^2} \qquad (3.20)$$

The maximum intensity of the propagated beam locates in $z = 0$. The critical distance for the Gaussian beam in z axis is the DOF which depends on the objective's magnification and the numerical aperture.

$$DOF = 2z_0 = \frac{2\pi w_0^2}{\lambda} \qquad (3.21)$$

$$w_0 = \frac{\lambda}{\pi \, N.A} \qquad (3.22)$$

$$DOF = 2z_0 = \frac{2n\lambda}{\pi \, (N.A)^2} \qquad (3.23)$$

This is the origin of the high axial resolution that can reach by writing with highly focused laser beams. It shows a strong dependency with the $N.A$ of the microscope objective. Higher $N.A$ (e.g., 1.4 in oil-immersion objectives) results in an ideal point spread function (PSF) ideal for the two-photon-based microscopy and fabrication processes.

3.2.1. Dependence of the microfabrication on the focused laser properties

The laser source has a relevant role in determining the efficiency of the photo-cross-linking/polymerization process at least in two ways: spectrally and spatially. The presence of a few weight percent of the photo-initiator in a photo-curable resin is enough for triggering the photo-polymerization/crosslinking process. As described earlier, the photoinitiator absorbs the light and following a number of chemical reactions, radicals are generated which then trigger the polymerization/crosslinking process. A crucial task in light-matter interaction-based operation, which is the very early starting point of the photopolymerization/crosslinking, is tuning of the working wavelength of the laser source. Here the tuning of the working wavelength of the laser source on the absorption band of the photo-initiator is important. In single-photon photo-polymerization/crosslinking, the largest photo-crosslinking efficiency is obtained from tuning the laser wavelength around the absorption peak of the selected photo-initiator. On the contrary, for the two-photon polymerization/crosslinking processes, as "two-photon" process should imply, the working wavelength of the laser source should satisfy the rule of thumb $h\nu = 0.5(E_e - E_g)$ or $\lambda_{writing} \cong \frac{\lambda}{0.5}$. However, some recent studies [8] show that more functional and adequate values of the writing wavelength for two-photon processes should follow the relation $h\nu = 0.7(E_e - E_g)$ or $\lambda_{writing} \cong \frac{\lambda}{0.7}$. According to this claim, for dyes with absorption bands at above 550nm, pulsed lasers tuned at 800nm or above can be employed. The dyes with absorption bands below 550nm down to the near UV region, are

mostly used for single-photon polymerization, while for two-photon polymerization/crosslinking with these dyes we employ a visible-tuned laser sources. Aside from the wavelength factor, several other physical parameters affect the multi-photon microfabrication technologies, particularly thermal effects, pulse duration in the sample and repetition rate and other optical instrumentation factors (i.e., objective and lenses as seen from Equations 3.21-3.23).

Coming now to the laser spatial profile role, most of synthetic polymers and biological-based materials have small absorption and scattering (i.e., nearly transparent) cross-section in the NIR region 700nm-1100nm. Since the two-photon absorption or generally the non-linear absorption of a photo-responsive system requires high intensity of irradiation (GW/cm^2 − TW/cm^2), ultrafast and tightly focused beam are used to induce increase the probability of non-linear absorption with low laser mean power.

As seen from Equations 3-21 to 3-23, the condition of tight focusing is obtained by means of an objective with a medium-to-high N.A. From Abbe's diffraction formula the spot size d of a Gaussian beam after passing through of an objective correlates with the beam wavelength and the N.A of the objective.

However, a more detailed formula for the spot size includes also terms due the spatial profile or beam quality for the laser transverse mode (TEM). These are summarized in the use of quality facto, M, and by the following relation:

$$d = \frac{M^2 \lambda}{\pi NA}$$ (3.24)

The M^2 factor stands for the ratio of real laser beam parameter over the diffraction limit parameters (i.e., focal radius and the divergence angle in far-field) with the maximum value of ~1.0. In addition to these terms one should be also considered is any aberration arising from an incorrect alignment of the laser at the objective entrance pupil.

From the above considerations follows also that any optical engineering of the laser beam at the entrance of the objective lens, would allow to obtain new features of the structures fabricated by direct laser writing method (DLW). In fact, to create of 3D-structures with nano-to-micron features by means of photo-polymerization/crosslinking the beam need to be shaped in the far-field with a narrow, well defined profile, and control it along the optical axis. Aside from the aforementioned rule of the high numerical aperture in reducing the feature sizes, a beam with complex polarizations (e.g., radially polarized) and/or spatial field structure (e.g., Bessel beams) could improve the fineness of the fabricated structure.

A part from these applications, with a conventional TEM00 laser profile collimated at the entrance of a microscope objective along its optical axis that defines the real shape of the

laser beam as a coupled function of the radial and axial coordinates. However, the lateral and longitudinal intensity profiles via the Debye's approximation are:

$$I_0(r) = I_{max}\left[\frac{2J_1(R)}{R}\right]^2 \qquad \text{at } Z = 0 \qquad (3.25)$$

$$I_0(z) = I_{max}\left[\frac{\sin(Z)}{Z}\right]^2 \qquad \text{at } R = 0 \qquad (3.26)$$

In above equations $R = 2\pi a f^{-1}\lambda^{-1}r$ and $Z = \pi a^2 f^{-2}\lambda^{-1}nz/2$ where r and z are the cylindrical coordinates, a and f are the objective parameters (aperture radius and the focal length), n is the refractive index in the focal plane, and J_1 is the first order Bessel function [6]. This formulation is correct for the systems with high N.A aperture objectives ($a \gg f$). A convenient formulation of the overall 3D laser spatial profile is generally obtained by considering $N.A \approx na/f$ and employing a Gaussian approximation that allows to empirically combine the equations 3.25 and 3.26 together in the well-known following Gaussian 3D profile:

$$I(r,z) = I_{max} \exp\left(-2\frac{r^2}{w_r^2} - 2\frac{z^2}{w_z^2}\right) \qquad (3.27)$$

$$w_r \approx \frac{\sqrt{2}\lambda}{\pi\,N.A} \qquad w_z \approx w_r\frac{2\sqrt{3}n}{N.A} \qquad (3.28)$$

The 3D Gaussian formulation (3.27) allows to conveniently but approximately describe the dependency of spatial resolution of a multi-photon system. Therefore, even from a pure optical theory point of view, a Gaussian profile of a single spot or line laser written in the resin cannot be expected to be retrieved.

Moreover, another important consideration should be done here on the difference between the terms feature-size and resolution. The minimum feature-size, regardless of the technology and the instrumentation in use, is defined by the smallest polymerized or solidified voxel of the photo-curable resin, which is obtained at the threshold writing intensity. The threshold writing intensity corresponds to the minimum EM energy density required to be absorbed to fabricate a solidified (polymerization or crosslinking) volume, which is then the building-block of any desired structure. In analogy with the definition of a pixel, which corresponds to the smallest area in a 2D pattern/image that preserve the whole system information, in 3D structures we can talk about volumetric pixel or voxel. In photo-induced nano/microstructures, continuous scanning of a laser in lateral direction leads to formation of these voxels that, partially overlapping due to the slow scanning rate, form a 3D structure. Because of the domination of linear polarization in tight focal volume of a two-photon system, and some unavoidable asymmetry of the PI molecule, the focal spot slightly elongates in the direction of the polarization [6]. Regarding this axial elongation, the voxel shape or configuration resembles a

spindle. While the voxel itself determines the feature size, the minimum mutual distance of writing two voxels from each other is the *system resolution*.

Laser writing of a voxel in TPA regime with a focused femtosecond beam comes along with an absorbing energy density[4] of:

$$D^{(2)}(r,z) = \frac{\tau_{pulse}\,RtI_{max}^2\,\sigma^{(2)}G_0}{h\nu}\,exp(\frac{-4r^2}{\omega_r^2} - \frac{4z^2}{\omega_z^2}) \tag{3.29}$$

Here, t is the illumination time, and G_0 is the constant factor of the photo-initiator consumption. With similar assumptions, the intensity distribution of fabricated line while scanning the sample with a focused laser beam along a lateral coordinate (here chosen as y) with velocity V, can be formulated as it follows:

$$I(x,y,z,t) = I_{max}\,exp(-2\frac{x^2+(y-Vt)^2}{\omega_r^2} - 2\frac{z^2}{\omega_z^2}) \tag{3.30}$$

Finally, the integration of above-mentioned (3.29) and (3.30) formulas with the average dwell time per pixel $t = \frac{\omega}{V}$ allows to derive a complete formulation of the energy density during the scanning:

$$D^{(2)}(x,z,t) = \frac{\omega\sqrt{\pi}}{V}\frac{\tau_{pulse}RI_{max}^2\,\sigma^{(2)}G_0}{h\nu}\,exp(\frac{-4x^2}{\omega_r^2} - \frac{4z^2}{\omega_z^2}) \tag{3.31}$$

This formula allows a reliable and simple calculation of the dimension of the smallest fabricated structure. For instance the thickness d_x of the line along the coordinate x is expected to be:

$$d_x = \frac{\omega_r}{2}\sqrt{\ln\left(\frac{D_{max}}{D_{threshold}}\right)} \tag{3.32}$$

The ratio of ω_r/ω_z explains the elongation of the voxel in the plane. In total, by using the formulation summarized in this paragraph and the concept of polymerization threshold one can estimate is the laser writing resolution, or the minimum mutual distance between two structures (voxels) that can be spatially distinguished [6].

3.2.2. Heat accumulation during laser processing

The irradiation of an ultrafast laser pulse could heat electrons up to a temperature around $1000K$ when the irradiation is close to the dielectric breakdown point ($\sim 1\,TW/cm^2$). The

---

[4] $D^{(n)}(\vec{r}) \approx \frac{\tau_{pulse}R\sigma^{(n)}}{(h\nu)^{n-1}}\int_0^t I_0^n(\vec{r},t)G(\vec{r},t)dt$

percentage of radiative energy transfer from hot electrons of $T_e = 1000K$ to an absorber element at $T_c = 300K$ is very high and can be estimated as $\eta = (1 - \frac{T_c^4}{T_e^4}) \approx 99.2\%$. This claim explains the loss of system resolution and material processing for absorber sites out of the focal volume.

In order to derive a formulation of the temperature distribution during the DLW process, the intensity profile along the focal spot of diameter d could simply be written as below:

$$I = I_0 exp(\frac{-2R^2}{(d/2)^2}) \tag{3.33}$$

The temperature profile follows approximately the same behavior, with a rescaled variance, as the intensity distribution if the free carriers absorb linearly light up to high irradiance levels.

$$T \cong T_{max} exp(\frac{-8R^2}{d^2}) \tag{3.34}$$

Here the T_{max} is the maximum temperature in the focal plane and d is the standard deviation of the temperature profile that is determined by the thermal diffusion coefficient $\mathbb{D}$. Assuming this spatial profile, the solution of the 3D heat diffusion equation in spherical coordinate leads to the following expression of the temperature profile evolution with time, t, after a single very short pulse.

$$\frac{\partial T}{\partial t} = \mathbb{D}(\frac{\partial^2 T}{\partial R^2} + \frac{2 \partial T}{R \partial R}) \tag{3.35}$$

$$T(r,t) = T_{max}(\frac{d^2}{d^2 + 32 \mathbb{D}t})^{3/2} exp(\frac{8R^2}{d^2 + 32 \mathbb{D}t}) \tag{3.36}$$

Between consecutive pulses the temperature drops by a factor:

$$a = (\frac{1}{1 + 32 \mathbb{D} f_R^{-1} d^{-2}})^{3/2} \tag{3.37}$$

Where f_R is the laser repetition rate. The a factor determines the decrease of the temperature at the center of the spot, while the size of heated region scales as $R \sim t^{1/2}$ rate (due to isotropic heat diffusion). After n-pulses, the influence of a single pulse decreases following the factor given below.

$$a_n = (\frac{1}{1 + 32 n \mathbb{D} f_R^{-1} d^{-2}})^{3/2} \tag{3.38}$$

Regarding this dropping factor derived from equation (3.37), the maximum temperature at the end of a train of pulses (contain N pulses) will be given by:

$$T_N = T_1 \sum_0^{N-1} a_n \tag{3.39}$$

Here T_1 is the temperature increase due to the impact of the first pulse.

The same modeling approach used here for the heat accumulations induced by ultrafast (femtosecond-picosecond) laser beam absorption, could be adopted for studying the thermal effect in photo-polymerization/crosslinking on scanning setups. In fact, by taking into account the dwell time for each pulse of spatial size d in the focal plane, and the scanning speed V of the raster scanning setup, the dwell time can be computed as $t_{dw} = d_f/V$. This value should be compared to the thermal diffusion time across the spot size that can be estimated as $t_{th} = d^2/\mathbb{D}$[5] For typical experimental conditions one can be assumed is $\mathbb{D} = 10^{-6}\ m^2/s$, $d \cong 0.5\ \mu m$ and $V \cong 10 \mu m/s$. With these values $t_{dw} = d/V \cong 50\ ms$ and $t_{th} = d^2/\mathbb{D} \cong 250\ ns$. The cooling procees is therefore dynamically at the equilibrium during the scanning process. From these considerations, a fact is revealed that indicates the average temperature drop due to the heat transfer to the surrounding cold area between each incident pulses is dominated by the thermal diffusion time and how this compares to the relaxation times between the pulses. The total heat accumulation after N pulses have irradiated the sample can be derived as:

$$T_N = T_1(1 + a + a^2 + \ldots + a^N) = T_1 \frac{1-a^N}{1-a} \tag{3.40}$$

Here the a factor is defined as $a = \left(\frac{f_R t_{th}}{32 + f_R t_{th}}\right)^{3/2}$, which is another expression of the equation 3.37. This simple model provides us a simple explanation of the dependence of the heat accumulation on the laser repetition rate and the heat diffusivity of the medium. Each pulse in a train of N pulses results in a temperature increase dependent on both the beam and the material properties. Finally, in order to characterize the whole heat load, the laser ablation model described above provides us with an expression of the maximum increase of the temperature as [6]:

$$T_1^{max} = \frac{A.F}{l_s C_L n_a} \tag{3.41}$$

Where A is the Fresnel absorption coefficient[6], F is the laser fluence[7], l_s is the absorption depth, n_a is the atomic density of the material, and C_L stands for lattice specific heat.

3.2.3. Light source, optical elements, and the setup

From the physical point of view, a setup of two/multi-photon polymerization consists of three main parts; a light source, an array of optical focusing system, and scanning/positioning stage. However, depending on specific purposes, there are additional components like spatial light

---

[5] since in tight focusing regime the beam elongates cylindrically along the optical axis, the heat accumulation and the cooling time along the optical axis are larger than what described by equation $t_{th} = d^2/\mathbb{D}$.

[6] $A = 1 - R$, where defines as Fresnel reflection coefficient with respect to different polarization angles

[7] $F = E_p/S$ (E_p introduces the pulse energy, and S is the surface area)

modulator (SLM) system or diffractive optic elements. An interesting approach to the use of laser spot multiplexing with a SLM has been recently published by the group of Osellame and Cerullo [10] for the fabrication minimized platforms for cell growing. The group of Farsari has instead first applied SLM and holographic strategies for beam shaping purposes [11].

The light source properties and working conditions directly affect the non-linear processes on which the two-photon polymerization is based. As we already discussed in this chapter, parameters: like wavelength, pulse energy, pulse duration, repetition rate, special bandwidth, and beam profile are among most important parameters of a light source that have a direct impact on the polymerization result. To begin with the laser wavelength and bandwidth need to match with the spectral sensitivity of the photo-responsive medium. The beam profile affects the voxel shape and configuration, and the pulse energy and repetition rate determine the polymerization process efficiency/speed. Ultrafast-pulse laser employed in multi-photon polymerization generally produce pulses in durations of picosecond or hundreds of femtosecond. The necessary parameters to characterize laser pulses are pulse power P_p, pulse energy E_p, the repetition rate f_{rep}, pulse duration (width) t_p, and the average power $P_{ave} = E_p \cdot f_{rep}$. All those parameters are linked by the following equation:

$$P_{peak} = \frac{P_{ave}}{f_{rep} \cdot t_p} = \frac{E_p}{t_p} \tag{3.42}$$

The laser beam, while propagating through the optical path and expands to overfill the back aperture of the objective that provides a tiny focal spot in photo-curable medium. In the focusing system or the optical path prior to the objective entrance pupil plane, there are several optical elements that help controlling the beam shape and alignment and allows controlling the beam propagation to the focal plane, like filters and shutters, diaphragms, lenses, polarizers, dichroic mirrors, etc.
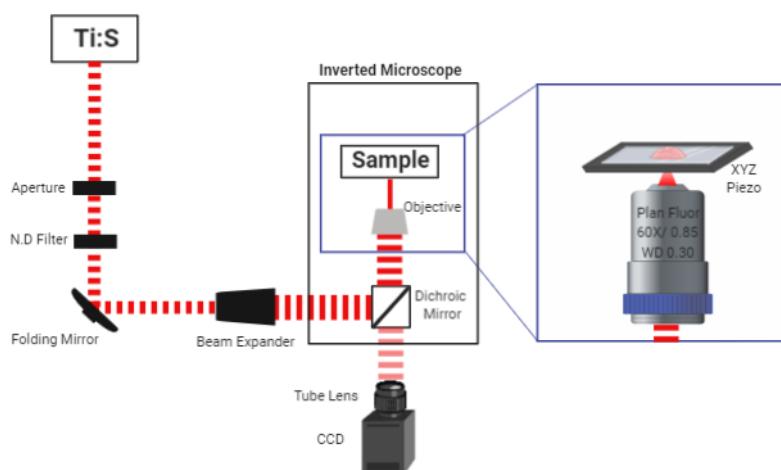
Figure 3.7. Configuration of the DLW setup developed in-house

After configuring an efficient laser beam by traversing through the above mentioned optical elements, and further tightening the focal spot using an objective, miniaturized complex 3D structures in nano-to-micron sizes could generate by moving the focal spot in the as-prepared photo-curable medium. As thoroughly discussed in elsewhere (for instance see reference [4]) the movement is possible either by means of a three-axis (XYZ) positioning piezo-stage on which the sample is mounted or by raster scanning the laser beam via galvo-scanning mirrors or beam deflection units. In any case, the axial displacement can be set with nanometer accuracy by means of a piezo actuator. All the actuators are designed and controlled externally using a computer-aided system or circuit.

3.3. References

[1] Robert W. Boyd, S., *Quantum Photonics: Pioneering Advances and Emerging Applications*

[2] Ravve, A., 2014. *Light-Associated Reactions of Synthetic Polymers*: Springer

[3] Lin, J., Liu, H., Chen, K. and Cheng, D., 2019. Modeling the Kinetics, Curing Depth, and Efficacy of Radical-Mediated Photopolymerization: The Role of Oxygen Inhibition, Viscosity, and Dynamic Light Intensity. *Frontiers in Chemistry*, 7

[4] Baldacchini, T., *Three-Dimensional Microfabrication Using Two-Photon Polymerization - Fundamentals*

[5] Andrzejewska, E., Podgorska-Golubska, M., Stepniak, I., & Andrzejewski, M. (2009). Photoinitiated polymerization in Ionic liquids: Kinetics and viscosity effects. *Polymer*, *50*(9), 2040-2047.

[6] Stampfl, J., Liska, R., & Ovsianikov, A. (2016). *Multiphoton lithography: Techniques, materials, and applications*. John Wiley & Sons.

[7] Free radical polymerizations. *(2015, March 30). No Added Chemicals. https://chem-is-you.blogspot.com/2015/03/free-radical polymerisation.html*

[8] Malinauskas, M., Žukauskas, A., Bičkauskaitė, G., Gadonas, R., & Juodkazis, S. (2010). Mechanisms of three-dimensional structuring of photo-polymers by tightly focussed femtosecond laser pulses. *Optics Express*, *18*(10), 10209.

[9] Fouassier, J., & Lalevée, J. (2013). *Photoinitiators for polymer synthesis: Scope, reactivity, and efficiency*. John Wiley & Sons.

[10] Zandrini, T., Shan, O., Parodi, V., Cerullo, G., Raimondi, M. T., & Osellame, R. (2019). Multi-foci laser microfabrication of 3D polymeric scaffolds for stem cell expansion in regenerative medicine. *Scientific Reports*, *9*(1).

[11] Manousidaki, M., Papazoglou, D. G., Farsari, M., & Tzortzakis, S. (2019). 3D holographic light shaping for advanced multiphoton polymerization. *Optics Letters*, *45*(1), 85.

Chapter 4.

Materials and methods

4.1. Materials

4.1.1. Bovine Serum Albumin (BSA)

Serum albumin (SA) is the most abundant protein in mammalian's blood plasma. The SA is a multifunctional, relatively large (MW ~66 kDa), and negatively charged globular protein at pH $\cong 7$. The SA extracted from Cow's liver, BSA (Bovine Serum Albumine), is a protein constituted by a single polypeptide chain comprising 583 amino acids with a heart-shaped tertiary structure. BSA and almost all the SA-based proteins are composed of three homologous domains (I-II-III), each grouped in two sub-domains (A, and B). In these proteins (here BSA), the responsible ligand binding sites, or in general the active binding regions for external dockings are located in IIA and IIIA subdomains which also known as Sudlow's site I and II. The isoelectric point (pI) of the BSA protein following the synthesizing protocol varies from 4.7 to 5 which implies negative surface charge in neutral pH.

4.1.2. Methylene Blue (MB)

Methylene blue is a cationic organic bluish dye from the family of phenothiazine with the chemical formula of $C_{16}H_{18}N_3ClS$, and the molecular weight of 319.9 gr/mol. Aside from its use in some therapeutic treatments, MB has been mostly used to stain the negatively-charged cells or fragments like nucleic acids, and also employed as an efficient antioxidant agent due to its oxidation-reduction capability in solutions. The dye shows an absorption peak at 664nm and a shoulder at 615nm, Figure 4.1. The broad absorption band of MB in the red-region of the light spectrum makes this dye a favorable candidate as a photosensitizer/photo-initiator compound in photo-excitation applications. The photo-excitation of the MB molecule, due to its high singlet oxygen quantum yield (ϕ_O ~0.5) [10, 11], results in the activation of the singlet oxygen which then leads to the formation of oxidizing radicals. The generated radicals further give rise to induction of polymerization/crosslinking of the photo-responsive medium in use.
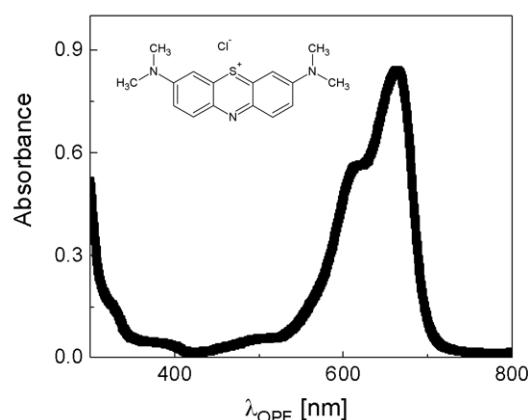
Figure 4.1. Absorption spectrum of Methylene Blue (MB) dye in Milli-Q grade water

4.1.3. Rose Bengal (RB)

Rose Bengal with a chemical formula of $C_{20}H_4Cl_4I_4O_5$ and the molecular weight of 973.7 gr/mol is a pink-reddish anionic organic dye from hydroxyxanthene dye family or generally xanthene family. Fluorescein is a well-known dye of this family, and halogenated derivatives of fluorescein result in formation of dyes like Rose Bengal (tetraiodo-tetrachlorofluorescein), Eosin (borominated derivative), and Erythrosin (tetraiodofluorescein). RB or in general the xanthene family most effectively has been used as staining agents and molecular probe in various biological science disciplines. RB has an absorption peak at 560nm with a shoulder at 520nm (see Figure 4.2l). The quantum yield and singlet oxygen quantum yield of RB molecule respectively are ϕ=0.11 and ϕ_O=0.80 which classify the molecule among efficient singlet oxygen generator dyes [12]. Due to the low quantum yield factor, the RB molecule could not be used effectively as a photosensitizer however its high singlet oxygen quantum yield makes RB a suitable photo-initiator for photo-responsive mediums to induce initiating species.
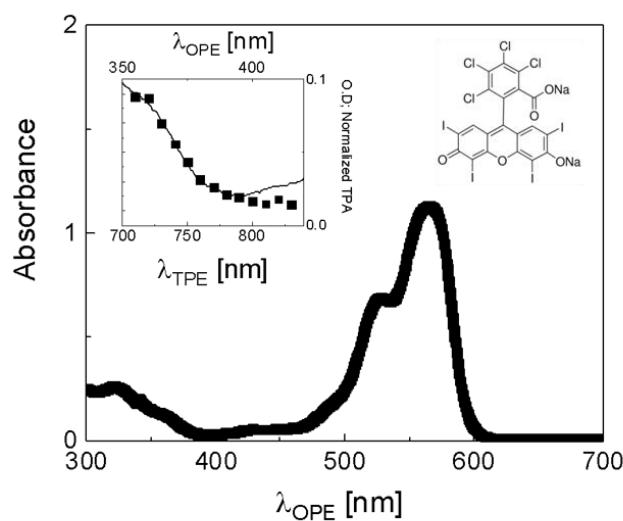
Figure 4.2. Absorption spectrum of Rose Bengal (RB) dye in Milli-Q grade water. The inset shows the two-photon spectrum superimposed to the rescaled single photon excitation.

4.1.4. Gold Nanoparticles (GNPs)

These tunable sub-micron-sized particles with promising applications in electronics and photonics exist in different shapes and formations. Among those, Gold Nanorods (GNRs) and Gold Nanostars (GNSs)/branched-gold nanoparticles exhibit suitable LSPR for performing studies in NIR and IR ranges.

The interaction of light with noble-metal nanoparticles produces coherent oscillations of the free electrons on the surface of the nanoparticle, a phenomenon called Localized Surface

Plasmon Resonance (LSPR). For non-spherically symmetric nanoparticles, or for large spherical ones (size > 100nm), the relaxation of this excitation can lead primarily to heat release to the lattice and then to the medium. These nano-scale hot spots can also be employed as tools to engineer the interaction of electromagnetic (EM) radiations with matter. The close vicinity of a molecule, being this inorganic or organic, synthetic or biological in character, changes its light-particle interaction rates. For example, there are changes in the absorption extinction coefficient or in the fluorescence quantum yield of the molecule that decorates the nanoparticle. Effects on the LSPR resonance are instead found when changing the medium refractive index. Upon photo-excitation of a plasmonic particle, the "sea" of the free electrons faces with a rapid (10-100 ps) temperature increase up to about 1000°C, while the lattice heats up by hundreds of degrees100°C [14] This is the fundamental of photo-thermal effect that is able to readily induce an increase of the temperature in the close surroundings of the nanoparticle (within few nanometers).

Two time scales are important in describing the relaxation processes that follow the absorption of a pulse of radiation by a nanoparticle of overall size d: the volumetric expansion time, τ_V, and the thermal diffusion, τ_{th}. The expansion time depends on the sound velocity v_s in the nanoparticle as $\tau_V = \frac{d}{v_s}$, and the thermal diffusion depends on the thermal diffusivity D through the nanoparticle as , $\tau_V = \frac{d^2}{D}$. They are typically $\tau_V \cong 10 - 20 \ ps$ and $\tau_{th} \cong 200 - 400 \ ps$, both much longer than the duration of the fs laser pulses, but much shorter that the repetition period of the lasers, which is of the order of 10 ns. Due to this rapid and highly localized heat flow and to mechanical oscillations arising from the rapid volumetric expansion, the absorbing plasmonic nanoparticles can be exploited for biophotonic imaging, for example through photo-acoustic signals, or for in vitro and in vivo therapeutic photothermal ablations.

4.2. Nano-plasmonic

Nanometer-sized particles (1-100nm) show significant enhancement of radiation-matter interactions in comparison with bulk materials, particularly under illumination of the light (electromagnetic radiation). In the nano-systems realm, nanoparticles of noble-metals display additional unique resonance, known as plasmonic effect. Aside from the chemical properties of the specific metal, the optical properties of metals are dominated by their capability to confine electric fields and by the free motion of conduction band electrons, where in nano-scale metal objects this dependency is amplified by the extreme confinement. When exposing the metallic nanoparticles to light, the free electrons on the surface are excited and causes a coherent motion of the electron cloud throughout the metallic nanoparticle. The motion of the

electron cloud induces a charge separation over the nuclei of the nanoparticle and further generates a Coulomb force between electrons and the nuclei that results in a spring-like oscillation. This collective oscillation of electrons at the boundary of nanoparticle and the surrounding medium (i.e., dielectric) is called localized surface plasmon (LSP). When the frequency of the light source matches the LSP oscillation frequency in a nanoparticle, a resonant interaction occurs which leads to a strong light absorption, scattering and to a marked amplification of the electric field close to the nanoparticle surface. This resonating condition between frequencies of the light source and the LSP is also known as the localized surface plasmon resonance (LSPR). In LSPR regime, the excitation relaxes in two different ways, a radiative process through diffused photons (i.e., scattering), and a radiation-less relaxation via phononic conversions following photon absorption. Due to the origin of the LSPR from the configuration of the electron cloud or density of electrons on the surface of nanoparticles, it is expected that factors like particle size and shape and dielectric constants of the metal and the surrounding medium, directly affect the nanoparticles plasmonic effect and indirectly influence the scattering and absorption cross-sections. It is noteworthy to say that the noble-metals nanoparticles (i.e., gold, silver and platinum) are preferred over other metallic compounds even though, recently, some interest is growing in the use of less noble or non-noble metals like and copper, aluminum, gallium, indium and nickel [15] due to their reduced cost.

The aforementioned absorption and scattering properties of nanoparticles induced via photo-excitation and the LSPR can be quantitatively describe by means of the Gans theory that allows to write the both the absorption and the scattering cross-section factors (σ_{abs}) and (σ_{sca}) [9]:

$$\sigma_{abs} = \frac{2\pi}{3\lambda} \varepsilon_m^{3/2} V \sum_i \frac{\varepsilon_2/(k^{(i)})^2}{(\varepsilon_1 + [(1-k^{(i)})/k^{(i)}]\varepsilon_m)^2 + \varepsilon_2^2} \tag{4.1}$$

$$\sigma_{sca} = \frac{8\pi^3}{9\lambda^4} \varepsilon_m^2 V^2 \sum_i \frac{(\varepsilon_1 - \varepsilon_m)^2 + \varepsilon_2^2/(k^{(i)})^2}{(\varepsilon_1 + [(1-k^{(i)})/k^{(i)}]\varepsilon_m)^2 + \varepsilon_2^2} \tag{4.2}$$

$$\sigma_{ext} = \sigma_{abs} + \sigma_{sca} \tag{4.3}$$

In above sets of equations, λ is the wavelength, ε_m is the dielectric constant of surrounding medium and $\varepsilon = \varepsilon_1 + i\varepsilon_2$ is the dielectric constant of the metallic nanoparticle, V stands for the nanoparticle's volume, and $k^{(i)}$ is the depolarization factor defined as:

$$k^{(a)} = \frac{1}{R^2-1}\left(\frac{R}{2\sqrt{R^2-1}}\ln\left(\frac{R+\sqrt{R^2-1}}{R-\sqrt{R^2-1}}\right) - 1\right) \tag{4.4}$$

$$k^{(b)} = k^{(c)} = (1 - k^{(a)})/2 \tag{4.5}$$

In above equation a, b, and c ($a > b = c$) are axial geometric indices of the nanoparticle. For a spherical nanoparticle, $k^{(i)}$ is equal to 1/3 for i= a, b and c. The term R is the aspect ratio of nanoparticle expresses as a/b. From these formulations, the cross-section factors are strongly correlated with the irradiation wavelength, size and shape of nanoparticles. One can directly see from these equations that both the cross-section factors depend on the volume V, though the absorption cross-section scales linearly with the volume while the scattering cross-section follows a V^2 trend. This dependence allows to understand the fact that when increasing the nanoparticle size the absorption to the scattering cross-sections ratio increases. Of course, for higher dimensions (mostly sizes >40nm) of nanoparticles the scattering will dominate. The ensuing wide tunability of the optical properties of these nanoparticles offers the possibility to operate a smart selection of nanoparticles, specifically tuned for different optical applications. Usually the nanoparticles of dimensions larger than 40nm are apt to be used in imaging/microscopy where a high scattering efficiency is required. Small nanoparticles (<40nm) are suitable instead for photo-thermal-based experiments, due to high absorption cross-section.

A non-spherical shape of nanoparticles has dramatic effects on the LSPR, both for the scattering and for the absorption properties. There is a zoology of nanoparticles shapes, from simple spherical-shaped to elongated ones (nanorods), branched (nanostars), prismatic (nanoprisms) or more complex shapes like nanocages. A comparison of the plasmonic resonance properties of nanoparticles with different shapes is based on the ratio of optical cross-section to the nanoparticle's volume. As an example, Gold-nanorods with high aspect ratios (length over width) but small volume display are the most efficient in terms of absorption, while nanoparticles of large volume and axial ration bring the best efficiency of scattering. Furthermore, the shape or, more precisely, the reduction of the nanoparticle symmetry, has an impact on the SPR spectral properties (e.g., position, and number peaks). The nanoparticles symmetry reduction allows to tune the spectral shape of the nanoparticles LSPR for specific applications. For example, the small (<40nm) gold nanospheres show a single SPR band around 520nm while with a symmetry reduction from sphere to cylinder (gold nanorods), two SPR bands will appear. One, arising from the excitation along the nanorod width axis is slightly blue-shifted from the position of the original nanosphere band, and the second band corresponds to the excitation along the cylindrical axis, with a spectral position that depends on the aspect ratio. By increasing the aspect ratio, this less energetic band will be shifted to even lower energies, corresponding to wavelengths as high as 1600 nm [16].
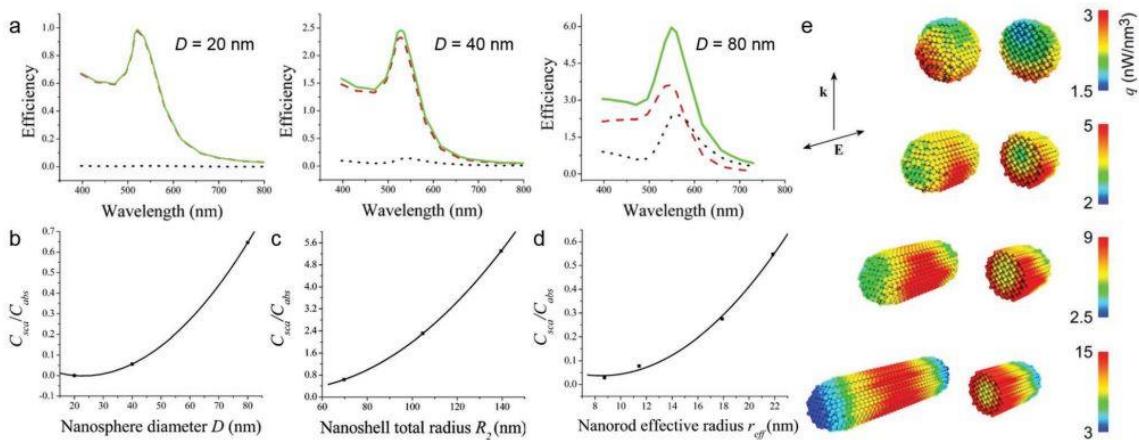
Figure 4.3. Size and shape-dependent absorption, scattering, and extinction properties of plasmonic nanoparticles. a) Calculated spectra of optical efficiency for gold nanospheres with different diameters (D): 20 nm (left), 40 nm (middle), and 80 nm (right). The red-dashed, black-dotted, and green solid lines indicate the efficiencies of absorption, scattering, and extinction for gold nanospheres, respectively. As the size of nanosphere increases, the contribution of absorption and scattering to the total extinction decreases and increases, respectively. b–d) Size-dependent changes in the relative ratio of scattering to absorption cross-sections (C_{sca}/C_{abs}) of nanoparticles: b) gold nanosphere, c) gold nanorod, and d) silica–gold nanoshell. In case of the nanoshell, the total particle radius (R_2) are varied (70, 105, and 140 nm) for a fixed ratio of the core radius (R_1) to the total particle radius ($R_1/R_2 =$ 0.857). In case of the nanorod, the effective nanorod radius (r_{eff}) that determines the volume (V) of the nanorod [r_{eff} $= (3V/4\pi)^{1/3}$] varied (8.74, 11.43, 17.9, and 21.86 nm) at a fixed aspect ratio of 3.9. Reproduced with permission [5]. e) 3D mapping of the heat power density of different shaped colloidal gold nanoparticles (nanosphere and nanorod) at their respective LSPR conditions. Cross-sectional images (right side) reveal the heating power density of the inner parts of each nanostructure. Reproduced with permission [6].

4.3. Photo-thermal effect

The non-radiative relaxation of the LSPR via electron-phonon coupling occurs through thermalization of the hot electrons with consequent increase of temperature of the lattice and generation of local heat. This phenomenon is the so-called photo-thermal in plasmonic bodies (e.g., noble metals). The relaxation of the LSPR follows a chain event; Landau damping, carrier relaxation, and thermal dissipation. Generation of hot carriers (electrons and holes) via photo-excitation of the metallic nanoparticles forces high-energy electrons to occupy states above the Fermi-state where they face with a non-thermal energy distribution with respect to the Fermi-Dirac principles (within a time-scale of 1-100 fs). From here the excited carries tend to relax back (redistribution) through the electron-electron scattering phenomena which results in the electronic (or internal) thermalization (100 fs-1 ps). In final relaxation (100 ps-10 ns), the electronic energy relaxes back to the equilibrium by transfer to the metallic lattice via electron-phonon collisions. Following this step, a thermal dissipation (i.e., external thermalization) of the particle lattice phonons with the medium occurs, that induce the local heating in the nano-environment of the particle.

In the various application fields where the photo-thermal effect of these nanoparticles is used one important factor is the rate of temperature increase. In other word, a proper exploitation of photo-thermal effect originates from an efficient nanoparticle cooling rate that leads to an efficient nano-environment heating. In conditions when the rate of nanoparticles excitation and the temperature increase is larger than the relaxation or cooling process, the medium surrounding the nanoparticles is inefficiently exploiting the photo-thermal effect. This, in turn, causes structural damages to the nanoparticles or even ablation. Considering a spherical nanoparticle with a radius r_s and a thermal diffusivity of D_n, under irradiation of a high-power laser with a pulse width shorter than the thermal relaxation time (approximately given by $\tau = r_s^2/6.75 D_n \cong 200\ ps$), the excited nanoparticle cannot efficiently dissipate heat in its environment [4, 13] and it heats up. This fast temperature increase of the nanoparticle, induces the transfer of energy as heat (~85% of the photo-induced one) to a thin volume around the nanoparticles. When the temperature in this nano-environment surrounding the nanoparticles comes close to 85% of the critical temperature, the pressure increases above the surface tension-dependent (σ) pressure ($p = 2\sigma/r_s$), and this enables the vaporization of the surrounded medium and the generation of microbubbles[1]. The vaporization (that includes effects like cavitation and localized fluid pressure) of medium further isolates the nanoparticles causing particles fragmentations and an additional cooling rate reduction.

4.4. Heat equation

For nanoparticles for which the absorption dominates the light extinction (i.e., smaller than 50nm), dispersed in a suspension at concentration C, the photo-induced temperature increase (ΔT) is determined by the laser source intensity I_0, the particle's absorbance A over optical path length l, the sample heat capacity c_p, and the laser spot area d.

$$\Delta T \sim \frac{I_0(1-10^{-A})}{d\ C\ c_p\ l} \tag{4.6}$$

The heat generated by the excited nanoparticles dissipates in the interfacial surrounding medium of temperature T_s (within the suspension but of the laser spot) on a time-scale of pico-to-nanoseconds depending on the nanoparticle's size, the delivered energy, and the medium condition.

$$\frac{T_p(t)-T_s}{T_i-T_s} = exp[-(t/\tau_d)^\beta] \tag{4.7}$$

In the above formulation, the time derivation of the nanoparticle's temperature $T_p(t)$ is characterized by the difference between the initial temperature of nanoparticle T_i, and that of

---

[1] Young-Laplace pressure formula [7, 8]

the medium, with the heat dissipation time-scale τ_s and a logical constant[2] β. The dissipation time-scale can be estimated by matching the heat capacity of nanoparticles of radius r ($\frac{4}{3}\pi r^3 c_p \rho_p$) and the heat capacity of the adjacent thermal diffusion layer of length l_d ($4\pi r^2 l_d c_d \rho_d$) where $l_d = (D_f \tau_d)^{1/2}$ and here D_f stands for the fluid thermal diffusivity [4].

$$D_f = \frac{k_d}{\rho_d c_d} \tag{4.8}$$

$$\tau_s = \frac{r^2 c_p{}^2 \rho_p{}^2}{9\, c_d \rho_d k_d} \tag{4.9}$$

In regimes where the rate of interface thermal conductance G ($W.m^{-2}.K^{-1}$) is lower than the medium conductance ($G \ll 3c_d \rho_d k_d / rc_p \rho_p$), β approaches unity and the conductance of the interface dominates in adjacent layer medium. Then the above formula simplifies to.

$$\tau_s = \frac{rc_p \rho_p}{3G} \tag{4.10}$$

By employing Eq.4.7, the energy balance of a system containing plasmonic nanoparticles in a suspension contained in a glass cuvette under laser irradiation can be described by the following equation when the thermal equilibrium within the sample is much faster than the energy dissipation of the system with the laboratory:

$$\sum_i m_i c_p \frac{dT}{dt} = \sum_j Q_j \tag{4.11}$$

The sum in the left hand side is over the various components of the system: the nanoparticle suspension and the cuvette (possibly a cuvette holder). The Q_j term accounts for several processes: the laser energy absorbed by the nanoparticle suspension Q_I, the heat absorbed by the cuvette Q_0, the conduction heat flow Q_{con}, and the radiative heat Q_{rad}. At a closer look, the Q_I is determined via the relaxation of electron-phonon in SPR of nanoparticles excited by radiation tuned at the LSPR wavelength λ:

$$Q_I = I(1 - 10^{-A_\lambda})\eta_T \tag{4.12}$$

, where η_T is the efficiency of thermal energy accumulation from SPR upon the light absorption and A_λ represents the absorbance of the nanoparticle suspension according to the Beer-Lambert's law. The Q_{rad} is given by the well-known Stefan-Boltzmann equation:

$$Q_{rad} = a\epsilon\xi(T^4 - T_{amb}{}^4) \tag{4.13}$$

---

[2] For nanoparticles with diameters between 5-15nm the estimation is $\beta = 0.6$ and for those with diameters between 25-50nm $\beta = 0.7$; (Hu and Hartland et al.)

Here ϵ is the emissivity factor, ξ is the Stefan-Boltzman constant, a is the area cross-section through which the heat is transferred, and T_{amb} defines the ambient temperature. One can be considered is to add also the convective term of the heat transfer to this term. However, the total heat flux from the suspension to the external ambient, can be described overall by considering a heat transfer coefficient h closely related to the linear thermal driving force:

$$Q_{ext} = ha(T - T_{amb}) \tag{4.14}$$

With this simplifying assumption, and by further assuming that the heat dissipated with the cuvette I negligible with respect to the laser energy absorbed by the suspension, the energy balance is determined by the simplified equation, as reported below:

$$\sum_i m_i c_p \frac{dT}{dt} = Q_I - Q_{ext} \tag{4.15}$$

Within the same approximated model, the system time constant τ_s given above in Eq. 4.10, can be empirically rewritten as it follows:

$$\tau_s = \frac{\sum_i m_i c_p}{ha} \tag{4.16}$$

From here, by introducing a dimensionless factor of temperature θ and scaling of ambient temperature T_{amb}, the real time temperature T, and the maximum temperature T_{max}, the gradient of θ can be derived through the time, which accounts for a micron-scaled heat transfer in a sample medium containing nanoparticles.

$$\theta(t) = \frac{T_{amb} - T(t)}{T_{amb} - T_{max}} \tag{4.17}$$

$$\frac{d\theta}{dt} = \frac{1}{\tau_s}\left[\frac{Q_I}{ha(T_{max} - T_{amb})} - \theta\right] \tag{4.18}$$

The above equation reduces to the $\frac{d\theta}{dt} = \frac{-\theta}{\tau_s}$ when the laser source is off (or temporary off between pulses) defining the system cooling ratio (for detailed description see reference [4]).

4.5. Methods

4.5.1. Direct Laser Writing (DLW)

In this thesis, which is based on the long term goal to control cells growth and differentiation by exploiting the thermal-sensitivity of the living cells, specific photo-thermally active microstructures have been designed. With this aim, a series of bio-based micropatterns and assemblies made of BSA protein was fabricated by means of the two-photon assisted DLW techniques, to act as the hosting beds for cell cultures. In order to apply photothermal

stimulation on cell, the proteinaceous structures have been doped with photothermally active GNPs.

Direct writing, by definition, is an operation or technique in which materials can be printed, and dispensed over a substrate or surface with variable feature size, down to tens of nanometers. Like other printing techniques of the class rapid prototyping and additive manufacturing, the direct writing manipulate materials, but at finer resolution and digitally defined positioning. The Direct Laser Writing (DLW) technique is defined as the direct manipulation of materials by means of a laser source without the exploitation of an optical mask, being this obtained by a physical mask or by shaping the light wave front by means of a spatial light modulator (SLM) or a digital micro-mirror (DMD). The interaction of the material with the laser source, leading to photo-polymerization or photo-crosslinking, can be either single-photon or multi-photon. The DLW can be implemented either on an inverted or a direct microscope setup. In the present study both the single-photon and multi-photon (two-photon) methods were applied to fabricate the desired proteinaceous patterns. The different capabilities of these approaches in producing structures with different spatial scales allowed the present study to access a broad range of patterns and architectures. The single-photon method results in reasonably fast structuration but at large-scales (i.e., mesoscopic) while the multi-photon method lead the study towards the fabrication of fine micron-sized structures, despite of being slow and time-consuming.

Crosslinking of the proteinaceous ink in multiphoton excitation regime was induced by the absorption of the NIR laser emission from a Titanium-Sapphire (Ti:Sapph) femtosecond pulsed laser source coupled to an inverted microscope setup. The optical path is an array of lenses and folding mirrors mounted in a way to modify and control the beam shape before entering the microscope, but the basic operations made on the laser wavefront is a beam diameter expansion to fit the entrance pupil of the objective. After traversing the optical path, the laser beam enters the microscope setup (see chapter 3 section 3.2.3). The multi-purpose microscope setup contains several important parts: piezo controlled sample holder stage, objective, and CCD. In most cases of DLW, the sample holder is a three-axis (XYZ) piezo-driven stage, which is controlled externally through a computer-based program and provides the freedom to write pre-defined patterns in a 3D volume. The mounted CCD (in our case a EM-CCD Cascade 512, Photometrics, USA) helps in recording and visualizing the polymerization process. Among the various components, the objective plays the crucial role in photo-polymerization process by localizing the focal spot down to hundreds of nanometer. The table below summarizes the parameters of the laser source and microscope setup involve in the present study.

Table 4.1. Laser source and microscope-objective information

Laser Type	Repetition Rate	Pulse Duration	Working Wavelength	Mode	Objective
Ti:Sapph	80MHz	200fs	700nm-900nm	Pulsed	60X- N.A 0.85 (Dry)[a]

a Nikon, Plan Fluor DIC-M, WD 0.3

For single-photon-assisted DLW, producing meso-structures, a different setup was employed. A continuous-wave (CW) mode Ar-laser (2020-5 Spectra Physics – Newport, USA) working at the wavelength of 514nm acted as source. On the contrary of the multiphoton DLW setup, that uses a piezo-driven stage to drive the laser spot in fabricating microstructures with a nanometer accuracy in the X, Y, and Z axes, the X and Y laser spot positioning for the single-photon setup is provided via a couple of galvano-scanner mirrors mounted in the optical path. In this optical configuration, the laser traverses the optical path, reaches the cover-glass and hits the sample from below (i.e., the cover-glass and ink drop interface), Figure 4.1, similarly to the two-photon setup.
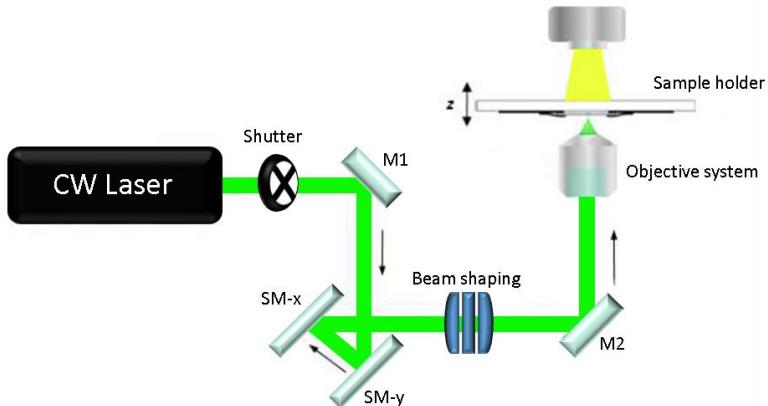
Figure 4.1. Laser setup (Ar-laser in CW mode, working wavelength = 514nm) used for single-photon-assisted DLW of [BSA-RB] ink include mirrors (M1 and M2), galvanometric mirrors as the scanning systems (SM), an array of lenses for shaping the beam after the scanning system, and the objective system (multiple lens array) to focalize the beam on the sample plane.

4.5.2. Infrared imaging

According to the main goals of this study, as mentioned earlier, the fabricated microstructures were doped with plasmonic NPs (i.e., GNRs and GNSs). One emerging research line in medical imaging domains is photothermal imaging (PTI). The *in-vivo* and *in-vitro* PTI attracts the scientific attention besides the conventional imaging techniques like confocal and fluorescence microscopies. In principle, the idea in PTI lies on reading the highly localized photo-induced temperature increase with low resolution thermal sensitive devices. However, for a more efficient thermal characterization of materials, in the present study another photothermal imaging technique was developed that relies on the acquisition of the thermal load induced in the sample by a highly focused laser beam by means of a thermographic camera. The sample is raster scanned with a modulated highly focused laser beam and the image is reconstructed digitally from the information (maximum temperature reached on the sample, as well as temperature profile and rising time) retrieved from a time stack of thermographic images acquired synchronously with the laser irradiation. This will be discussed in Ch. 5. Hereafter, the main issues related to the detection of thermal radiation that will be useful in describing the reconstruction algorithm will be discussed briefly.

At temperatures above the absolute zero (0 K) all the materials, regardless of the size, emit heat waves. The intensity and the wavelength of this emitted radiation (far infrared) which has electromagnetic origin are determined by local material's temperature itself (apart from emissivity factors). The ratio between the radiated heat flux $d\phi$ and the area cross-section dA of the radiation gives a temperature and wavelength related parameter called emittance (T, λ).

$$M(T,\lambda) = \frac{d\phi}{dA} \tag{4.20}$$

The detectors for infrared range (e.g., thermo-cameras) are divided into two different categories of wavelength-related measurements, short-wave (SW) and long-wave (LW) with sensitivity over, respectively, the short-band 2-5 μm and long-band 8-14 μm of the thermal emission. There are detectors also for the near-infrared region which detect waves with wavelengths of 0.75-1.5μm, typically used to align NIR lasers. The latter device are not pixelated and are based on a wide field image setup. The SW and LW detectors came with a pixelated detector that is simply a matrix of micro-bolometers and that can be devised in three geometries: point, linear, and array. Among detectors used in the thermography technologies, Bolometric detectors are the most widely used. These detectors are basically resistors with low heat capacity and large negative temperature coefficient of resistivity. This coefficient is defined as below:

$$\alpha_T \; = \frac{1}{\mathbb{R}}\frac{d\mathbb{R}}{dT} = -\frac{B}{T^2} \tag{4.21}$$

Where $\mathbb{R}$ is the bolometric resistance. The bolometric detectors are then built as arrays of microbolometer resistors, and the smallest element of detection, or pixel, is typically 15µm X 15µm in size for low cost thermo-cameras.

The infrared radiation is collected by a very low numerical aperture Germanium optics and conjugated on the microbolometer array with a 10-30 times demagnification. Therefore the pixel size in the sample plane is typically 150-450µm. The radiation absorbed by the microbolometers causes changes in their resistance that is read by the electronics, processed by the signal readout circuits and used to build the heat-distribution map. There are important factors controlling thermography by thermo-cameras: Noise Equivalent Temperature Difference (NETD), Field of View (FOV), Instantaneous Field of View (IFOV), and etc. Each of these terms would require a full treatment physical analysis of the electronic signals. Here we simply discuss these factors for the case of the IR radiation and how they impact on the quality of the thermal images. The NETD or the temperature resolution defines the temperature difference between the object/specimen and the ambient environment by generating signal-to-noise ratio of one. The FOV provide the spatial resolution of the infrared camera based on its installed optical elements and determines the area of observation with respect to the distance d. The IFOV is also a term in describing the spatial resolution of the camera. However, the IFOV is the FOV of each pixel (single detector) or can be consider as the minimal field of view. In general, the spatial resolution of an IR camera is directly determined by the Germanium collection optics and the size of the pixels, projected in the sample plane. However, another intrinsic limitation of the resolution is the thermal diffusivity of the heat in the sample plane during the acquisition time. Therefore, the smaller is the pixel size and the higher is its sensitivity, the lower could be the acquisition time and the higher could be the effective resolution reached by the camera. However, we still need to fulfill the Abbe's condition relating the optical resolution to the wavelength and the numerical aperture of the collection optics. As we will discuss later, for NA $\cong 0.02$ and $\cong 9\mu m$, we have a minimum resolved feature of about $\frac{\lambda}{NA} \cong 450 \ \mu m$, approximately the size of the pixel size projected onto the sample plane.

4.5.3. Cell-culture

In the present study, in order to achieve one of the main goals of the project, i.e. to study cell-adhesion and differentiation on the fabricated micropatterns, a series of *in-vitro* trials was carried out on different cell-lines (i.e., NIH 3T3 fibroblast, and 4T1 cancer cells).

Cell-culture is a term that refers to extraction of cells from animal or plant and the growth in an artificial environment. This extraction could be done directly from the real tissue (e.g.,

enzymatic or mechanical tools) or indirectly from already established cell-line or cell strain. After cell removal and isolation from the tissue, under an appropriate condition, cells will differentiate and spread over the culturing substrate. This stage of the work is also known as primary culture. From this point, it is necessary to subculture (passage) the cells by transferring them to a new container holding a fresh growth medium. The first passage or the first subculture stage generates the cell-line or subclone. The artificial environment or the place within which the cells are cultured must contain several factors that include essential nutrient supplies (e.g., amino acids, carbohydrates, vitamins, minerals, and etc.) growth factors, hormones, gases (i.e., O_2 and CO_2), all along with regulating also several physico-chemical factors (pH, osmotic pressure, temperature). These are the suitable models for any desired *in-vitro* studies.

Nowadays, the research fields of regenerative medicine, tissue engineering, cancer personalized therapy and drug discovery are extensively investigated and are based on the identification cellular mechanisms and cell-microenvironment interaction both *in-vitro* and *in-vivo*. These studies allow understanding the cell-cell and cell- ECM (extra cellular matrix) interactions. Despite the most relevant information can be obtained from real tissue models in *in-vivo* studies, the *in-vitro* trials based on cell-cultures are suitable alternatives that offer the possibility to modulate the stimuli at will. In these in-vitro assays, the possibility to exploit micro-structured substrates for the cell growing is of paramount importance. The first research studies in this direction appeared about 40 years ago [17], and since 2009 the in-vitro engineered platforms became an essential tool for research in medical biotechnology. These methods can be categorized into two classes of micropatterning: 1) the indirect and 2) direct procedures that genuinely help in understanding fundamental of cellular functions like; migration, differentiation, polarity, chirality. Among the advantages of micropatterned platforms, compared to the traditional petri dishes that has brought the possibility to directly control the cell spatial confinement and the roughness of the substrate. In fact, it has been shown that [18], upon cell-adhesion to the micropatterns, the cells re-configure their shape according to the geometry of the substrate. This is a useful strategy for studying the nucleus orientation and deformation. For example in round patterns cells and nucleus form circular while in rectangular geometries cells become more elliptical [19]. Interesting development in the direction of 3D micropatterns and their confinement and mechanical effect on the cell shape and adhesion, have been carried out recently by the group of prof. Raimondi at the politecnico di Milano [20]. Micropatterning is a tool to manipulate the cell response to a variety of stimuli, mainly mechanical, and to record information on cellular physiology that can be further exploited to promote different aspects of human health technology. In this thesis, the goal is to extend these methods to the applications of other physical stimuli, like temperature.

4.6. References

[1] Huang, X., Neretina, S., & El-Sayed, M. A. (2009). Gold Nanorods: From synthesis and properties to biological and biomedical applications. *Advanced Materials*, *21*(48), 4880-4910.

[2] Qiu, L., Larson, T. A., Smith, D. K., Vitkin, E., Zhang, S., Modell, M. D., Itzkan, I., Hanlon, E. B., Korgel, B. A., Sokolov, K. V., & Perelman, L. T. (2007). Single gold Nanorod detection using confocal light absorption and scattering spectroscopy. *IEEE Journal of Selected Topics in Quantum Electronics*, *13*(6), 1730-1738.

[3] Minkina, W., & Dudzik, S. (2009). *Infrared thermography: Errors and uncertainties*. John Wiley & Sons.

[4] Roper, D. K., Ahn, W., & Hoepfner, M. (2007). Microscale heat transfer Transduced by surface Plasmon resonant gold nanoparticles. *The Journal of Physical Chemistry C*, *111*(9), 3636-3641.

[5] Jain, P. K., Lee, K. S., El-Sayed, I. H., & El-Sayed, M. A. (2006). Calculated absorption and scattering properties of gold nanoparticles of different size, shape, and composition: Applications in biological imaging and biomedicine. *The Journal of Physical Chemistry B*, *110*(14), 7238-7248.

[6] Baffou, G., Quidant, R., & Girard, C. (2009). Heat generation in plasmonic nanostructures: Influence of morphology. *Applied Physics Letters*, *94*(15), 153109.

[7] Kotaidis, V., & Plech, A. (2005). Cavitation dynamics on the nanoscale. *Applied Physics Letters*, *87*(21), 213102.

[8] Vafaei, S., & Wen, D. (2015). Modification of the Young–Laplace equation and prediction of bubble interface in the presence of nanoparticles. *Advances in Colloid and Interface Science*, *225*, 1-15.

[9] Kim, M., Lee, J., & Nam, J. (2019). Plasmonic Photothermal Nanoparticles for Biomedical Applications. *Advance science*, *6*(17).

[10] Alarcón, E., Edwards, A. M., Aspee, A., Moran, F. E., Borsarelli, C. D., Lissi, E. A., Gonzalez-Nilo, D., Poblete, H., & Scaiano, J. C. (2010). Photophysics and photochemistry of dyes bound to human serum albumin are determined by the dyelocalization. *Photochem. Photobiol. Sci*, *9*(1), 93-102.

[11] Niu, E., Ghiggino, K., Mau, A., & Sasse, W. (1988). Fluorescence and photochemistry of dye sensitizers in nafion membrane. *Journal of Luminescence*, *40-41*, 563-564.

[12] Hoebeke, M., & Damoiseau, X. (2002). Determination of the singlet oxygen quantumyield of bacteriochlorin a: A comparative study in phosphate buffer and aqueous dispersion of dimiristoyL-L-α-phosphatidyLchoLine liposomes. *Photochemical & Photobiological Sciences*, *1*(4), 283-287.

[13] Takami, A., Kurita, H., & Koda, S. (1999). Laser-induced size reduction of noble metal particles. *The Journal of Physical Chemistry B*, *103*(8), 1226-1232.

[14] Kumar, S., & Sood, A. K. (2016). Ultrafast response of Plasmonic Nanostructures. *Reviews in Plasmonics*, 131-167. https://doi.org/10.1007/978-3-319-24606-2_6

[15] Kim, S., Kim, J., Park, J., & Nam, J. (2018). Plasmonic nanomaterials: Nonnoble-metal-Based Plasmonic nanomaterials: Recent advances and future perspectives (Adv. Mater. 42/2018). *Advanced Materials*, *30*(42), 1870320.

[16] Pallavicini, P., Donà, A., Casu, A., Chirico, G., Collini, M., Dacarro, G., Falqui, A., Milanese, C., Sironi, L., & Taglietti, A. (2013). Triton X-100 for three-plasmon gold nanostars with two photothermally active NIR (near IR) and SWIR (short-wavelength IR) channels. *Chemical Communications*, *49*(56), 6265.

[17] Gu, Z., Fu, J., Lin, H., & He, Y. (2019). Development of 3D bioprinting: From printing methods to biomedical applications. *Asian Journal of Pharmaceutical Sciences*.

[18] Guo, Z., Hu, K., Sun, J., Zhang, T., Zhang, Q., Song, L., Zhang, X., & Gu, N. (2014). Fabrication of Hydrogel with cell adhesive Micropatterns for mimicking the oriented tumor-associated Extracellular matrix. *ACS Applied Materials & Interfaces*, *6*(14),

[19] Levina, E., Kharitonova, M., Rovensky, Y., & Vasiliev, J. (2001). Cytoskeletal control of fibroblast length: experiments with linear strips of substrate. *Cell Science*, *114*, 4335-4341.

[20] Zandrini, T., Shan, O., Parodi, V., Cerullo, G., Raimondi, M. T., & Osellame, R. (2019). Multi-foci laser microfabrication of 3D polymeric scaffolds for stem cell expansion in regenerative medicine. *Scientific Reports*, *9*(1).

Chapter 5.

Results and Discussion

5.1. Photoresist and Device

5.1.1. Bovine serum Albumin (BSA) and Methylene Blue (MB)

With a glance on the fundamentals of photo-polymerization discussed in previous chapters, and in the view of the main goal of the present project to produce proteinaceous microstructures, the first approach toward microfabrication is to prepare a resist composed of BSA proteins as monomers and MB dyes as photo-initiators (here is called as [BSA-MB]). The MB dye molecules trigger the cross-linking process through the two-photon absorption process, acting both as photosensitizer and photoinitiator. The BSA protein acts as monomeric unit which, upon the photoexcitation of the MB dye, starts the crosslinking chain reaction. Our initial choice is motivated by the presence of several experimental studies in which BSA and MB were used as main compounds to produce a photoresist [14, 15]. Normally, the photoresist for photo-cross-linking can be synthesized only by mixing the photosensitizer/initiator and monomer/oligomer parts. However, depending on the desired final product, other compounds with different activity and role could be added to the basic composition. For example, in the present case of study and aside from the idea of embedding plasmonic NPs within the proteinaceous microstructures, compounds like PolyVinylPyrrolidone (PVP) and Glycerol were added to regulate the viscosity of the ink. The ink viscosity has non-linear dependence on the PVP percentage in as reported in Figure 5.1. The ink was composed of [BSA-MB-PVP] prepared at different concentrations of PVP up to [PVP] = 10% w/w. The viscosity of the ink was measured from the fit of the mean square displacement of latex microbeads observed and tracked on the stage of a confocal reflection microscope.
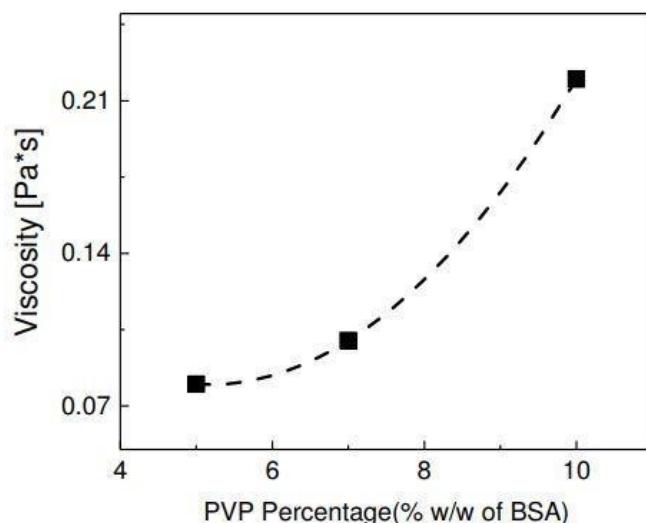
Figure 5.1. Non-linear behavior of ink viscosity following the PVP increasing concentration in the ink solution, with respect to the BSA total amount in use.

There are examples, in the works of other Authors, where complex inks with several enhanced features were obtained by adding agents for pH-control, multiple photo-initiators (initiator and co-initiator), or by pursuing other chemical modifications [15, 16].

In this study, different amounts of the BSA protein powder were added to the as-prepared MB dye solution. The molecular concentration ratio between the monomeric and photo-responsive components has a direct impact on the final fabricated microstructure and subsequently, controls various properties like the elastic modulus, degree of conversion, and the flexural strength. Disproportions of the concentration of the photo-responsive molecule in the ink with respect to the concentration of monomeric part, leads to large radical generation and monomer conversion rates, which brings to the fabricated structures higher elasto-mechanical properties. On the contrary, low concentration of the dye molecule in the ink solution, due to the possible limited radical generation, results in having random-site polymerization/crosslinking and the fabrication of mechanically instable structures. In the present study, the effect of the dye on the photo-resist efficiency was studied both in terms of the PI/monomer concentration ratio and of the type of photo-initiator: the low photo-initiator concentration regime is explored in section 5.1.1 on BSA and MB inks, and the high photo-initiator concentration regime is explored in section 5.1.2, on BSA and RB inks.

Both BSA (Bovine Serum Albumin, lyophilized, ≥96%) and MB (Methylene Blue, M6900) was purchased from Sigma-Aldrich (Merck, NL). The stock MB solution was prepared at 4 mM by dissolving MB powder in Milli-Q water. In each round of experiments, a fresh 1mL ink stock was produced by mixing 300mg BSA and 6% w/w of MB from the 4mM stock solution reaching the final concentration of [MB] ≈ 0.01% w/w in the ink, and afterward kept in fridge (4°C) for further uses. The stability of proteinaceous ink was tested up to 12 days and the functionality was found approximately unchanged through this period.

Before describing the implementation of the DLW on the [BSA-MB] ink, it is necessary to briefly summarize the photochemistry and photophysics of this complex. From the theory and protocols behind the TPP or crosslinking of mediums, the laser source wavelength should not always follow the exact mapping $\lambda_{\text{TPE}} = \frac{\lambda_{OPE}}{0.5}$ (λ is the excitation wavelength) behavior. In most of cases, efficient two-photon excitation of the photo-responsive compounds take places at $\lambda_{\text{TPE}} \cong \frac{\lambda_{OPE}}{0.7}$. In the case of MB, as $\lambda_{\text{OPE}} \cong 665$nm, the expected two-photon absorption peak should then lies at $\lambda_{\text{TPE}} \cong 950$nm. However, as it has been already addressed elsewhere, the experimental two-photon absorption band of MB spans from 720nm to 800nm.

Here, the strategy for tuning the laser setup on the most appropriate wavelength for the photo-resist and reach an efficient photo-crosslinking of the [BSA-MB] complex, was based

on searching the minimum necessary average power to trigger the photo-crosslinking. The minimum amount of photonic energy needed to excite an optimized photo-responsive medium is mostly limited by how much the excitation wavelength is tuned on the photo-initiator absorption band. Therefore, the shifting the experimental excitation wavelength toward either the red or the blue wings of the spectrum leads to inadequate molecular excitation which will appear as the increase the threshold dose needed to trigger the cross-linking. With this strategy in mind, in this first part of the study, the [BSA-MB] ink was irradiated with wavelengths from 750nm to 810nm (Ti:Sapph Femtosecond pulsed laser source). The dataset of this experiments are reported in Figure 5.2, from which one can infer which is the most effective spectral region (i.e., around 780nm) for the photo-crosslinking of the [BSA-MB] ink. From the analysis of Figure 5.2, one can conclude that the most efficient region of the spectrum to perform photo-crosslinking of [BSA-MB] is around 780nm. Figure 5.2 reports two writing parameters, the threshold power for photo-crosslinking, $<P>_{thr}$, that is defined as the minimum level of the laser power at which one can detect visually the formation of a more optically dense blob under the action of the laser spot, and the writing threshold power, $<P>_{write}$, that is defined as the minimum level of the laser power at which a continuous polymerized line is formed under action of the laser irradiation scanned at the speed v_{scan} on the focal plane.
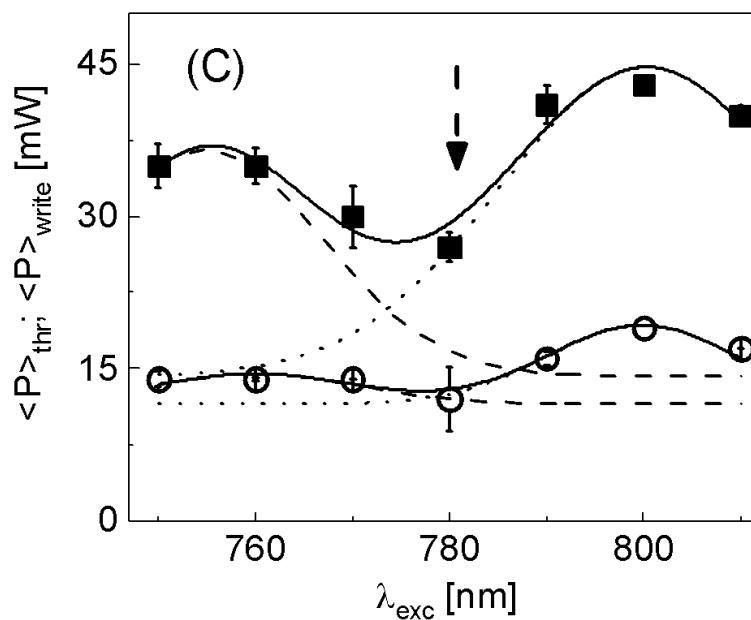
Figure 5.2. Dependence of the threshold power $<P>_{thr}$ (black squares) and writing power $<P>_{writing}$ (open circles) on the writing wavelength. The scanning speed was set at $v_{scan} = 2\mu m/s$ for each $<P>_{writing}$.

Former spectroscopic studies of interaction of BSA and MB indicate the presence of a quenching mechanism between these two molecules due to Fluorescence Resonance Energy

Transfer (FRET) in which BSA acts as the donor and MB as the acceptor. The FRET efficiency can reach high values, due to the electrostatic attraction of the two molecules [17, 18], and can be measured for a fluorescent molecule as MB is, from the drop of the fluorescent quantum yield. Such a drop can however arise from a direct quenching by a quencher molecule as well as from a FRET mechanism. For fluorescence imaging applications quenching is detrimental. However, a careful study of the drop in fluorescence quantum yield (or, better, its fluctuations in times) may shed some light on the active intersystem crossing which carries the fluorophore to a triplet-state excitation, which is a necessary step towards the photo-polymerization.

MB is considered in many studies as a photosensitizer agent and, as such, added to the photo-responsive ink in which it comes along with a co-initiator molecule or generally a donor molecule. However, dependent on the molecular characteristic and composition of the monomer/oligomer in use, the [monomer-MB] complex (here [BSA-MB]) could be itself a photo-initiating system. In these cases, the [BSA-MB] complex undergoes photo-crosslinking generally through a radical generation along two different paths: either indirectly assisted via singlet oxygen generation (path-1), or as a cationic dye assisted via the amine ends of active amino acids (path-2) in BSA protein. The mechanism of photo-induced singlet oxygen was discussed in chapter 3, along with the description of the route leading to the production of active radicals. The principle behind singlet oxygen generation is the photo-excitation of the photo-responsive molecule. In principle, the ground-state oxygen molecule, which exists in form of a triplet-state, meets the excited dye and changes to excited singlet oxygen molecule. Through this procedure, the dye molecule, sitting in its triplet state, relaxes toward its ground singlet state. Numerous research studies of the amino acids interaction with singlet oxygen have indicated that when the singlet oxygen sits beside a proteinaceous molecule and interact with Trp, Try, His, Met, and Cys side chains, the radical oxygen species can be generated. Through interaction of singlet oxygen with aromatic residues (i.e., Trp and Tyr), the radicalization occurs through a ring-opening reaction resulting in radicals with hydroperoxide functional groups (R-O-OH), while upon interaction of singlet oxygen with His, Met, and Cys, after a bond-cleavage, radicals with peroxide (R-O-OR) functional group are generated. In the singlet oxygen mediated photo-crosslinking of proteins, these generated radicals may be the leading parts for chain propagations.

In path-2, typical of the cationic dye-based photo-responsive systems as it is the case for the [BSA-MB] ink, the photo-initiation process undergoes a bimolecular (electrostatic) interaction with a donor. For the [BSA-MB] resists, protein amine groups play the role of donors. Following this event, a series of interaction between the dye molecule and the amine reactive group results in the production of a free radical. Upon photo-excitation of the dye, an exciplex

will be formed between the dye molecule (the acceptor) and the amine (the donor). The exciplex participates in electron and proton transfer actions from the amine to the molecule leading to a bond cleavage and further free radical generation. This route of radical generation by participation of a secondary active residue has been often referred to as "semi-direct approach of photo-crosslinking". Coming to the experimental results reported in Figure 5.2, about the identification of the most efficient wavelength for TPC of the [BSA-MB] resists, one can say that independent of the specific cross-linking pathway, the choice of wavelengths in the 770 – 790 nm range results in the best condition for TPC of the ink in use.

The DLW setup includes a Ti:S femtosecond laser source (Newport, Tsunami, CA, repetition rate of 80MHz; pulse width 250fs on the sample) followed by an inverted microscope system (Nikon TE300). Aside from the laser source and beam conditioning optics, the microscope-objective, and more specifically the N.A and its working distance (WD), play the most important role in the delivery of adequate energy dose on the sample plane and in determining the final feature size. In multiphoton-excitation experiments we always choose medium to high N.A (≥ 0.6) objectives both to decrease the size of the diffraction limited spot in excitation and, for fluorescence imaging, to enhance the photon collection efficiency that scales as $(N.A)^4$. In our setup, the laser beam was focused by a 60X microscope-objective (Nikon dry objective, WD=0.3; N.A=0.85). It was mentioned in earlier chapters that to have accesses writing structures in three-dimension (3D, XYZ), it is necessary to employ a three-axis motion control board installed on the microscope sample plane. In this study, a three-axis piezo-driven stage (Hera p733-Pifoc P725, Physik Instrument) was mounted on the inverted microscope and externally controlled via an Arduino shield (Arduino-Uno, Campustore, Italy).

Prior to each trial, fresh batches of ink were prepared and stored in the fridge. A drop (~50 μL) of the as prepared ink was seeped on a pre-cleaned cover glass and transferred on the microscope sample holder. The laser beam was focused at the interface between the ink drop and the cover glass: focusing the beam at the interface is important to fabricate structures well fixed on the cover glass surface. In fact, when using low-viscosity inks, structuration deep in the sample volume happens inadequately and at random. To overcome this, DLW of microarchitectures took place in a bottom-to-top (layer by layer from the cover-glass interface) mode, starting from the glass slide.

5.1.2. Bovine serum Albumin (BSA) and Rose Bengal (RB)

As a second approach for two-photon-assisted microfabrication of proteinaceous structures, Rose Bengal (RB) dye was chosen as photo-responsive molecule to be coupled with BSA.

Doubts in the efficiency of [BSA-MB] complex photo-crosslinking process (namely the possibility to be off-tuned from the real two-photon peak of MB) and its cationic property, pushed us to explore different dye/protein combinations and find much more optimized conditions to fabricate proteinaceous microstructures. RB is an anionic dye molecule with the two-photon peak at 800nm (as computed from the $\lambda/0.7$ rule). This dye, due to its efficient singlet oxygen quantum yield has been widely employed in singlet oxygen and photodynamic therapy (PDT) studies and applications. However, this ability of producing singlet oxygen will also foster free radical production, which is one of the most limiting factors for an efficient photo-polymerization/ crosslinking. Aside from the consideration of property of RB in singlet oxygen generation, the photo-responsive effect importantly relates to the interaction of RB molecule with the protein (BSA) binding sites and the number of dye molecule per each BSA protein n. The RB dye, as well as the MB, can undergo different routes in generating free radicals. However, despite the fact of sharing, with different extent, the singlet oxygen-mediating free radicals pathway, RB is also capable to activate a direct free radical generation driven by *electron transfer* (Type I reaction) while MB induces a semi-direct photo-crosslinking process via *energy transfer* (Type II reaction).
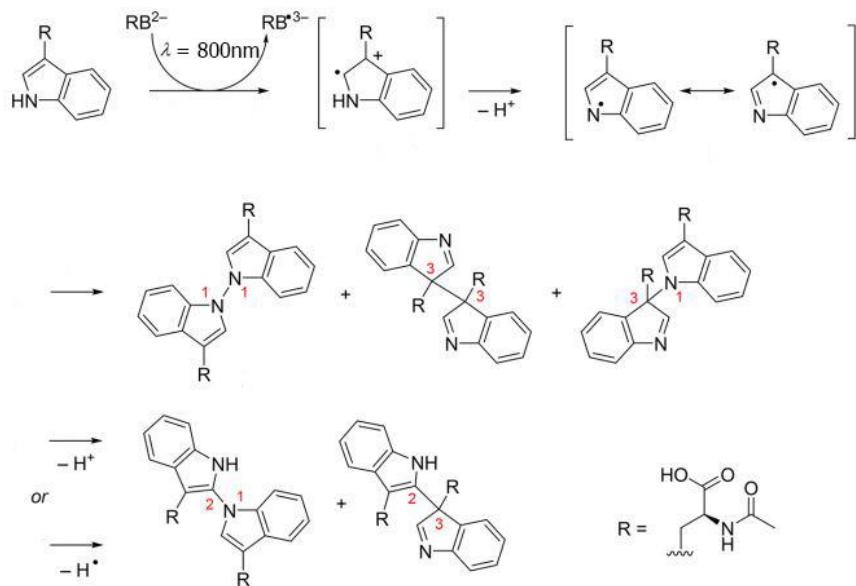
Figure 5.3. Scheme of photo-crosslinking of N-acetyl-L-tryptophan residue. Upon TPE of RB^{2-}, the molecule undergoes inter-systems crossing and forms as triplet-excited state molecule $^3RB^{2-}$. From this point by accepting electrons from amine derivative of Trp, the RB excited molecule changes to an anionic radical ($RB^{\bullet 3-}$) and makes the Trp donor molecule as a cationic radical. Reproduced from reference [1].

In type I reaction of RB with proteins (here BSA), reductive quenching takes place between dye molecules and BSA side-chain residues mainly Trp (Figure 5.3), Tyr (Figure 5.4), Met, Cys, and His. Upon photo-excitation of RB (RB^{2-}), either via single photon or multi-photons,

the molecule lands on the singlet state ($^1RB^{2-*}$) and from this state transits, via intersystem crossing, to the triplet excited state ($^3RB^{2-*}$) with an efficient quantum yield (~1 in water). In turn, $^3RB^{2-*}$ interacts with above mentioned amino acid residues producing free radicals in the protein. The reactions mostly involve the production of Tyr-derived phenoxyl radicals (C_6H_5-O-) and thiyl radicals (R-S) from Cys. The formation of highly reactive radicals along with reacting with other protein side chains or even self-reactions of these entities help in crosslinking of BSA proteins.

Two-photon crosslinking experiments were carried out by means of the same laser source (Ti:Sapph) on fresh ink solution (1 mL in volume) obtained by mixing 50mg BSA and 2mg RB (Sigma-Aldrich, dye content 95%) in Milli-Q water. This strategy, of combining BSA and RB in powder form to make the [BSA-RB] ink, provides approximately three RB molecules for each BSA protein which increases the chance of photo-excitation, free radical generation, and hence enhances the photo-crosslinking efficiency with respect to the [BSA-MB] ink prepared at 1/19 (dye/protein) ratio. For TPC of [BSA-RB] ink, the pulsed laser source tuned at 800nm was focused at the glass-ink interface on an inverted microscope for bottom-to-top DLW experiment. Following the same protocol as in the case of [BSA-MB], 50µL drop of the ink was deposited on microscope cover slips just before the DLW experiment. However, high resolution multi-photon DLW by raster scanning is intrinsically slow. Therefore, it is important to ensure the largest stability of the ink drop during the DLW by limiting factors like the photothermal activity of the dye at the writing wavelength, which directly affects the ink dehydration. Indeed, in the case of [BSA-MB], due to the photothermal activity of MB in the red region of spectrum, fast dehydration was observed. The dehydration of the ink results in increasing viscosity of the medium as the DLW proceeds. As seen in chapter 3, the ink viscosity is known to be a crucial factor for a stable polymerization/crosslinking rate. Changes in the ink viscosity as a function of time alters the microstructure uniformity. To avoid fast dehydration in DLW of microstructures written in the [BSA-MB] ink, the ink drop was preserved in an open cylindrical chamber sealed by a thin layer of immersion oil for microscopy.
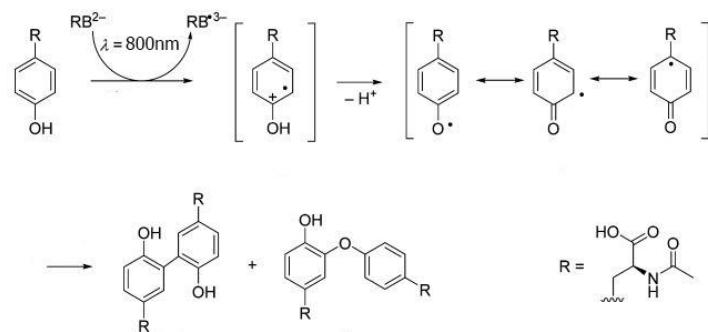
Figure 5.4. Scheme of photo-crosslinking of N-acetyl-L-tyrosine following the TPE of RB^{2-}. Reproduced from reference [1].

5.2. DLW of [BSA-MB] and [BSA-RB]

The study proceeded first by studying the parameters that affect the ability to fabricate stable proteinaceous microstructures that can be used to perform living cell studies (both cell growing and bacteria eradication). The fabrication was pursued by two-photon-assisted DLW of BSA based ink via Ti:S femtosecond pulsed laser on an inverted microscope-piezo-driven stage systems [see 5.1]. The three-axis piezo-actuators stage was controlled via Arduino shield through a Digital-to-Analog (DAC) converter chip coupled to an Arduino Uno board driven by a simple raster scanning program. By employing the Arduino programming environment, the piezo-stage was driven so to fabricate micro-patterns like square array, parallel lines, and slits in maximum plane size of 50µmX50µm.
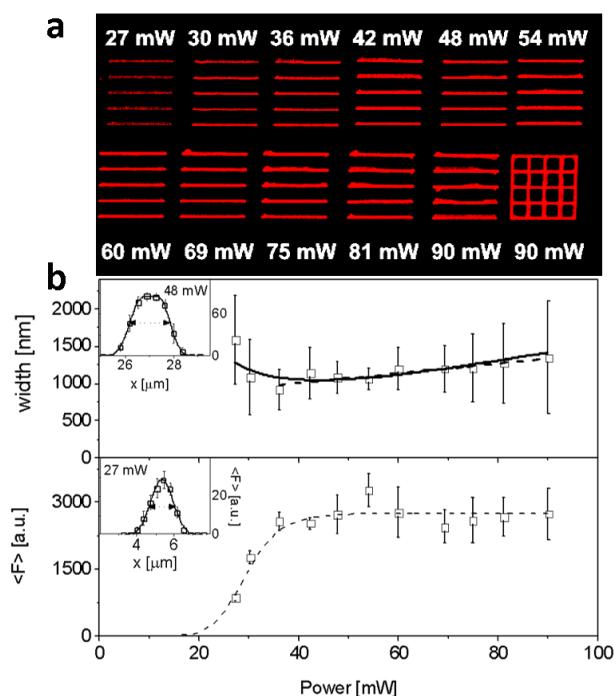
Figure 5.5. Microstructures fabricated using two-photon-assisted DLW of [BSA-MB] ink complex. (a) 40µm Parallelepiped structures from [BSA-MB], red channel is MB emission ($\lambda_{exc} = 633nm$, $\lambda_{em} = 665nm$) at writing powers listed in panel (b)

Due to the different two-photon absorption cross sections of the RB and MB photo-initiators, different laser average power <P> were used to implement DLW on [BSA-MB] and [BSA-RB] inks. As discussed above in the analysis of Figure 5.2, the average threshold power <P>$_{thr}$ defines the lower level of power needed for photo-polymerization/crosslinking: working below that threshold results in random polymerization/crosslinking or in general "no structuration", while raising the power well above the threshold leads to the formation of micro-bubbles. In the case of [BSA-MB] of crosslinking threshold was located at about 20mW of source average power. Above 100mW average power, micro-bubbles generation hindered the possibility to create continuous microstructures. In the microfabrication trials performed on the [BSA-RB]

ink, the cross-linking threshold level was located at 100mW source average power and a massive formation of micro-bubbles was observed above 150mW average power.

The above differences in the writing threshold implies a difference in the minimum dose required for triggering the radical cross-linking reaction. For a multi-photon experiment, as it is the case here, the high N.A objective increases the probability of multi-photon excitation through a tight focusing of beam on the sample plane. In the in-house setup that uses a 60X N.A=0.85 objective, the spot size (beam waist) on the sample plane is theoretically ω_0 ~ 0.57µm (ω_0, $1/e^2$ radius). The fluence or the energy dose delivered to the sample with each pulse (~200fs pulse duration) in writing microstructures in [BSA-MB] (λ=780nm) and [BSA-RB] (λ=800nm) inks are approximately 0.02 and 0.12 Jcm^{-2}, respectively, and can span up to 0.18 Jcm^{-2}.

Aside from the average peak power, other factors that control the micro-structuration uniformity and efficiency are the stage scanning step (dl) and scanning speed (v). The piezostage was programmed to scan the sample with a = 0.1µm in the plane (X and Y) and the scanning speed was chosen in the range 1 µm/s < v < 10 µm/s. The efficiency of generated patterns directly correlates with scanning speed and the increase of the scanning speed requires higher doses of laser energy delivered per TPC voxel. On the other hand, very low scanning speeds at high doses of delivered energy cause micro-bubbles and unexpected damages to the structure. In most of trials in the present study, the scanning speed did not exceed 2 µm/s, resulting in a scanning time of 25s for a 50µm long line.
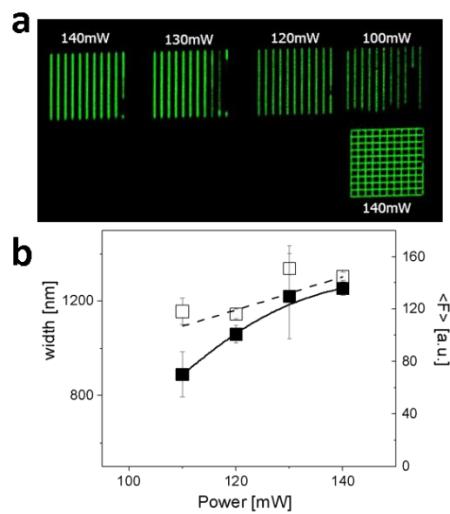
Figure 5.6. Microstructures fabricated using two-photon-assisted DLW of [BSA-RB] ink complex. (a) Green channel is RB emission ($\lambda_{exc} = 514nm$, $\lambda_{em} = 560nm$) at writing powers listed in panel (b)

The Figure 5.5 (panel a) summarizes the fluorescence confocal characterization of [BSA-MB] proteinaceous microstructures fabricated at increasing values of the laser average

power (Red channel is the MB emission at λ_{em}=665nm, under excitation at λ_{exc}=633nm, line length 40μm). From the profiles of the written lines (see for example the insets of Figure 5.5, panel b), the line width (FWHM) and the maximum fluorescence signal could be measured. These values are reported in the upper and lower plots of panel b, respectively, as a function of the laser source average power. The lines are the fit of the data to the function $\Omega_1 + \frac{a}{<P>^2} + b<P>$ (solid line) and the function $\Omega_0 + b<P>$ (dashed line) with the best fit parameters: Ω_0=740±90nm, b=7±1.6 nm/mW, Ω_1=200±50nm, and a=0.54=0.2 μm/mW. The minimum FWHM width estimated from the fitting function (solid line) of Figure 5.5b is 1040 ± 120nm for a writing power <P>=44 ± 4mW. This value is approximately twice the diffraction limit spot size, $\omega_0 \cong 0.6\frac{\lambda}{N.A} \cong 450$nm. The fluorescence average intensity signal is plotted as a fit to a sigmoidal nonlinear function of $\frac{a<P>^2}{1+b<P>^2}$ with best fit parameters a= 0.6±0.04nm/mW, b =0.002±0.001nm/mW.

Figure 5.6 presents (panel a) the fluorescence confocal characterization of microstructures written in the [BSA-RB] ink (Green channel is tuned on the RB emission λ_{exc}=514nm and λ_{em}=560nm; line length 40μm). Parallel lines and a square arrays were fabricated at the writing wavelength λ=800nm and increasing laser average power, from 100mW to 140mW. We analyzed these images by fitting the profiles of the written structures to Gaussian functions in order to derive the maximum fluorescence signal, <F>, and the FWHM width. Figure 5.6b summarizes the dependence of the FWHM of the structured lines (open squares, left axis) and the maximum fluorescence signal <F> (filled squares, right axis), both as function of average power. The dashed and solid lines are best linear fit to the FWHM (trial function $\Omega_0 + b<P>$; Ω_0=200±100nm and b=4.5±2 nm/mW) and to the average fluorescence signal. In this case, the minimum FWHM width that can be obtained is 970 ± 120nm for a writing power <P>=110 mW.

5.2.1. Width comparison of written microstructures, FWHM analysis

Apart from this first characterization of the microstructures, done by exploiting the signal of the dyes trapped within the structure to obtain confocal fluorescence microscopy (CFM) images, we employed also atomic force microscopy (AFM), and scanning electron microscopy (SEM). AFM was employed to characterize both the morphology and the elastic parameters of the DLW written objects. These microscopy techniques exploit different matter-radiation and matter-matter interactions to construct the image from the sample plane: we exploit fluorescence from the residual dye in the microstructure in CFM, the mechanical

interaction of the scanning probe with the sample surface in AFM, and a focused electron beam scanning the sample, in SEM. Each microscopy system brings its own contrast and resolution in imaging the sample. Hence, in order to have a correct estimation of the microstructure width and morphology, a set of comparative analyses was carried out, based on the comparison of the width of laser written microstructures recorded via all the above-mentioned microscopy instruments.
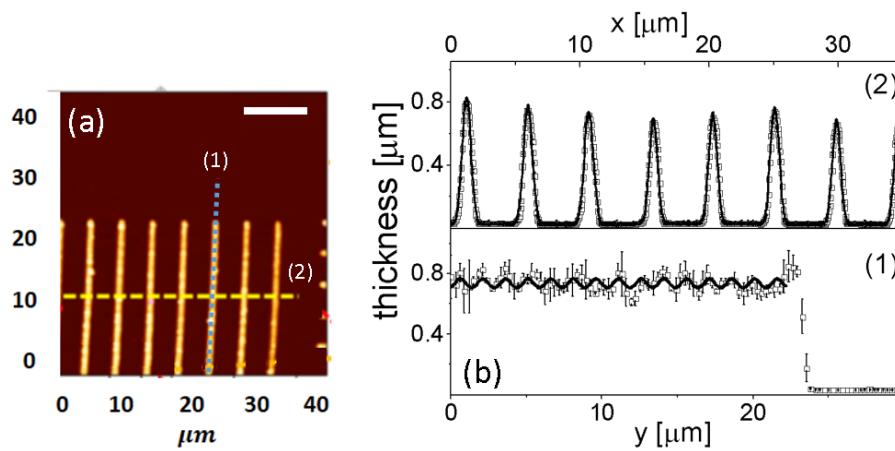

Figure 5.7. (a) AFM image of fabricated parallelepipeds from [BSA-MB] ink written with <P>=44mW, scale bar is 10μm. (b) Profiles of section 1 and 2, solid lines are best fit to the data with function $t = A\cos\left(\frac{2\pi y}{\Lambda}\right)$.

The first non-optical characterization of the written microstructures was carried out by means of AFM imaging. Figure 5.7 reports an AFM study of a set of parallel DLW written lines in [BS-MB] inks. The width analysis of the profiles measured along sections 1 and 2 in Figure 5.7a are reported in Figure 5.7b. The solid lines are the best fit to the data with a harmonic function $t = A\cos\left(\frac{2\pi y}{\Lambda}\right)$, for section 1 ($\Lambda$ =1.5 ± 0.05μm, A = 0.05 ± 0.006nm, for y ≤ 22 μm) and sum of Gaussian peaks, for section 2 (FWHM = 0.94 ± 0.04μm).
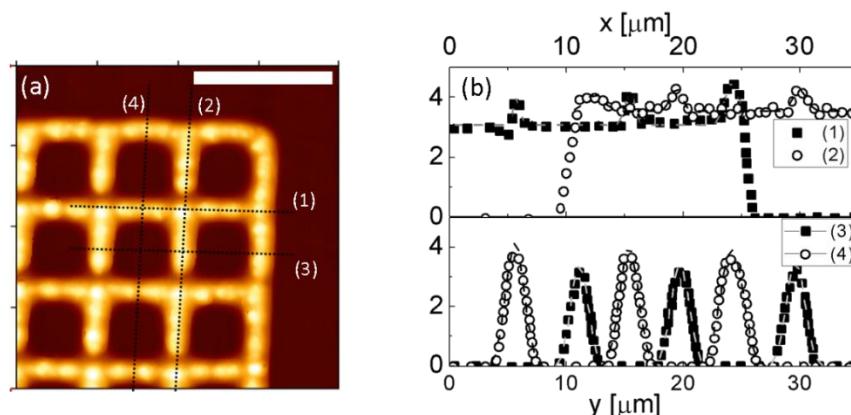
Figure 5.8. (a) AFM image of fabricated square-array from [BSA-MB] ink, scale bar is 10μm. (b) Profiles of the sections 1 to 4 in panel (a), and the y-axis shows the lines width in micrometer.

The characterization of more involved structures written by DLW in [BSA-MB] inks is reported in Figure 5.8. From a rectangular array (Figure 5.8a) a sections was selected across the center of the walls (dashed lines 3 and 4 in Figure 5.8a) whose profiles were analyzed by a multi-Gaussian fit (Figure 5.8b, lower panel) that provided the FWHM values of $1.87 \pm 0.07 \mu m$ (traces 3) and $2.1 \pm 0.2 \mu m$ (trace 4). The same analysis performed on the sections 1 and 2 in Figure 5.8a, along the vertical and horizontal walls, indicates that (see Figure 5.8b, upper panel) the written structures have an average height of 3-4 micrometers with high smoothness between crossings of the vertical and horizontal lines, at which a change of 3-4 % was observed in the height, clearly correlated to the crossing position.
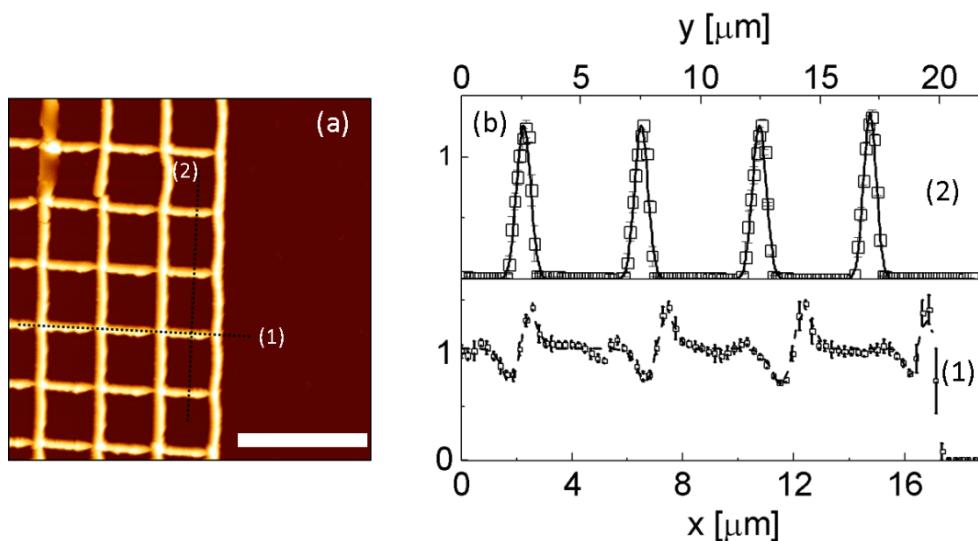
Figure 5.9. (a) AFM image of fabricated square-array from [BSA-RB] ink with <P>=120mW, scale bar is 10μm. (b) Thickness profiles of the structures along the selected sections 1 and 2 from the panel (a).

A similar AFM study was performed on microstructures written in [BSA-RB] inks. Figure 5.9 presents the AFM topographic image of a square-array written in [BSA-RB], in which the profiles measured along the dashed lines (1) and (2) show the thickness profiles presented in Figure 5.9b. In the upper panel of Figure 5.9b, the solid line, represents the best fit of a sum Gaussian to the data measured along section (2). The average FWHM of the Gaussian profiles fit to the profiles of the individual walls, is $660 \pm 20 nm$. The lower panel in the Figure 5.9b (dashed line, section (1)) is the best fit of a sum of first derivative of Gaussian functions (plus a constant height value) to the data with best fit FWHM=$850 \pm 220 nm$, with a maximum amplitude of the oscillations of about 500 nm. The positions at which we observed the oscillations in Figure 5.9b, section (1), are again very much correlated with the positions of the crossing between vertical and horizontal scanning of the DLW laser on the sample.
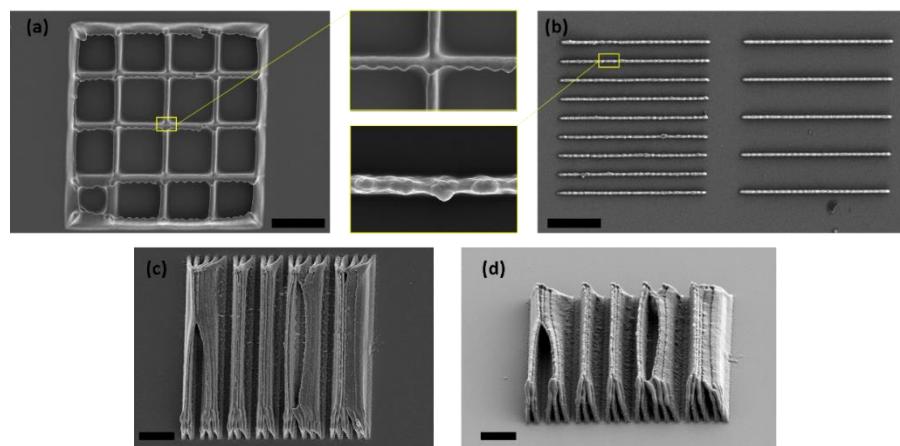
Figure 5.10. SEM images of (a) and (b) [BSA-MB]-based micropatterns, scale bars are 10µm, and (c) and (d) [BSA-RB]-based 3D slits, scale bars are 5µm.

From these topographical and morphological experiments (see Table 5.1), one can see that the micro-structuration of [BSA-MB] results in crosslinking of lines and patterns with larger features probably due to the fact that the writing wavelength (780nm-800nm) is quite off-tuned from expected two-photon peak of MB (~900nm). This fact led the trials to deliver too large energy doses to the ink inducing a photothermal effect in the MB dye that absorbs a large fraction of the red and NIR radiation. The rapid thermal dissipation in the ink of this local release of heat reduces the spatial resolution with which we can induce the free radical generation. For the same reasons, the micropatterns fabricated in the [BSA-RB] ink show good and acceptable surface uniformity.

Table 5.1. Width analysis of fabricated (DLW) proteinaceous microstructures. The FWHM are calculated from fluorescence confocal images (Fluo), AFM topographical images (AFM) and SEM images (SEM). All data are in micrometer.

		2D structures				3D structures		
Pitch	**[BSA]**[a]	Fluo[b]	AFM	SEM	**Pitch**	Fluo	AFM	SEM
20 (C)	**300**	1.14 ± 0.04	1.16 ± 0.1	0.93 ± 0.03	**10 (B)**	1.7 ± 0.1	2.1 ± 0.1	1.3 ± 0.1
20 (C)	**500**	1.16 ± 0.1	1.13 ± 0.08	0.86 ± 0.04	**15 (A)**	1.7 ± 0.1	2.2 ± 0.2	1.24 ± 0.1
5 (E)	**300**	1.4 ± 0.2	1.4 ± 0.2	1.25 ± 0.07				
5 (E)	**500**	1.16 ± 0.03	1.17 ± 0.08	0.84 ± 0.05				
			W_{Fluo}/W_{AFM}	W_{SEM}/W_{AFM}				
			1.00 ± 0.05	0.77 ± 0.03				

a: BSA concentration in mg/mL, b: Fluorescence
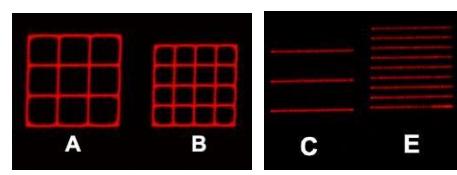
5.2.2. Young's modulus analysis

The elastic modulus was determined by AFM indentation experiments performed on rectangular parallelepiped structures (40 µm × 40 µm × 2.7 µm) written in BSA/RB inks. The force-indentation curves were measured on about 70 different positions on each microstructure and fit to a second-order compression force $F(\delta)$– indentation δ relation. From the fit of this plot to the Hertz model function, $F(\delta) = E' \frac{tan(\alpha)}{\sqrt{2}} \delta^2$, and by assuming a tip aperture angle (four-sided pyramidal tip; $\alpha = 20^o$, producer data), the reduced Young modulus E' can be estimated [21], which is related through the Poisson ratio of the tip (μ_{tip}) and the material (μ_{sample}), to the Young modulus of the tip, E_{tip}, according to the relation:

$$\frac{1}{E'} = \frac{1-\mu_{sample}^2}{E_{sample}} + \frac{1-\mu_{tip}^2}{E_{tip}} \tag{5.1}$$

Since the silicon nitride cantilever is very stiff ($E_{tip} \geq 100\ GPa$) and the Poisson ratio $\mu_{sample}^2 \cong$ 0.25, [22] the Young modulus was computed from the reduced value E' as $E_{sample} \cong E'(1-\mu_{sample}^2)$.

The AFM measurement of the Young modulus made according to the above approach on DLW fabricated features of [BSA-MB] ink (300mg BSA protein in 1mL Milli-Q grade water) showed a log-normal distribution, Figure 5.11. The mode value of this distribution, $E_{[BSA-MB]}$ = 240 ± 80kPa lies fairly well in the region of soft tissues, Figure 5.12.
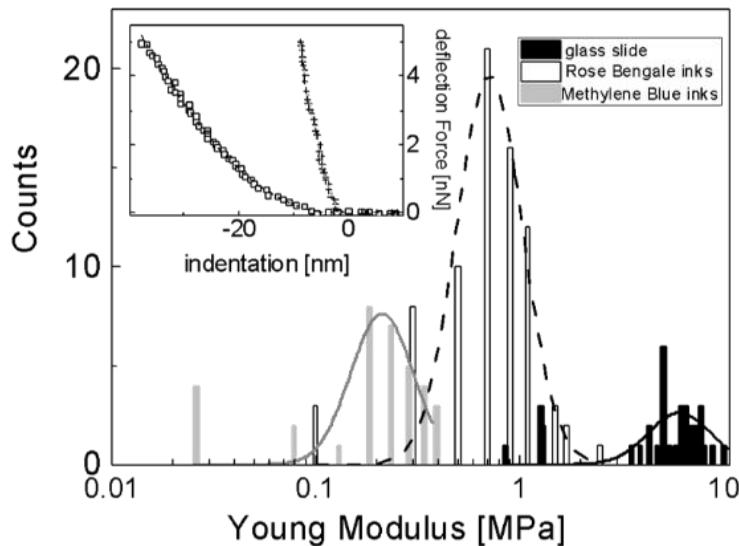
Figure 5.11. Diagrams of Young's modulus of the proteinaceous microstructure [BSA-RB] with BSA concentration at 50mg/mL (open bars) and [BSA-MB] with BSA concentration at 300mg/mL (hatched bars). The inset shows the details of Force-indentation curves together with Hertz model fitting for the case of [BSA-RB] ink with BSA concentration=50mg/mL (open squares) and the glass.

Figure 5.11 presents also the full comparison among the distributions of the Young's modulus values obtained by the Hertz model fitting of the $F(\delta) - \delta$ plot (inset: glass (crosses) and MB-based structures (open squares)), for the structures written in [BSA-RB] (open bars), [BSA-MB] (hatched bars), and for glass slide (filled bars). The black solid, black dashed, and solid gray lines are best fit to log normal functions of distributions measured on glass, [BSA-RB], and [BSA-MB] microstructures, respectively. As a reference for the experiments performed on the proteinaceous microstructures, the elastic modulus of a 170µm glass slide was found, E_{glass} = 6.9 ± 2.1 MPa.
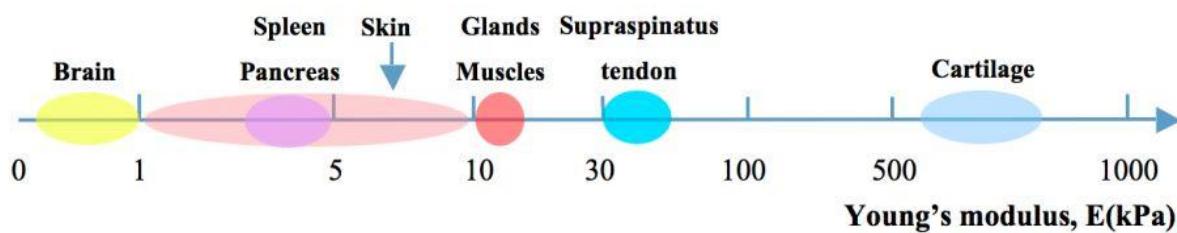
Figure 5.12. Young's modulus values of soft natural tissues, adapted with permission from reference [7].

However, the elastic modulus measurement for [BSA-RB] fabricated microstructures with larger concentrations of BSA were systematically smaller (see Figure 5.13). The value of $E_{[BSA-RB]}$ = 820 ± 300 kPa found for structures written in a 50mg/mL BSA protein [BSA-RB] ink was almost four times larger than the case of a 300mg/mL BSA protein [BSA-MB] ink.
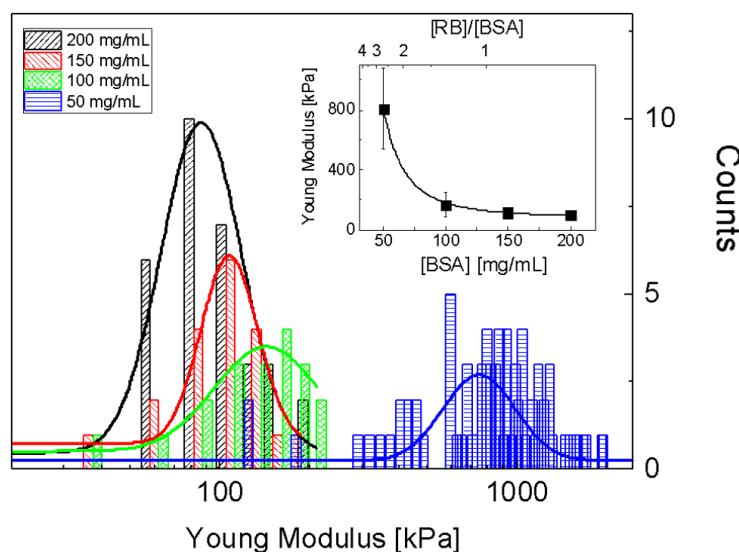
Figure 5.13. Depiction of dependency of Young's modulus to the protein concentration in microstructuration of proteinaceous features.

The mode values of the elastic Young modulus distributions can be fitted to power law function of the protein concentration C_{BSA} (Figure 5.13), $E_{max} = E_0 + a(C_{BSA})^{-p}$, finding best fit values $E_0 = 83 \pm 3 kPa$ and $p = 2.9 \pm 0.1$. The parameter E_0 estimates the Young's modulus of the microstructure written with no initiator/sensitizer. The steep power law, $p \cong 3$, indicates a high cooperativity of cross-linking process that reveals the dependency of the elastic modulus on the monomer (i.e. BSA) concentration and the relevant molecular weight of the whole system. Understanding the materials characteristic of the compounds is a crucial step to analyze the printed microstructure functionalities. In this approach, molecular weight plays an important role in the final structure or pattern robustness[1] [19] and stiffness. In polymer science, the molecular weight is the average weight of molecules that are involved in the polymerization process which also affects the polymeric/crosslinking chain lengths. As the molecular weight increases, the strength and toughness[2] [20] of the polymeric network increase. This phenomenon push proteinaceous blends in a corner in comparison with polymeric resins with tunable molecular weight property like PEG (Polyethylene glycol)-based compounds. However, protein-based resins have the advantage of higher biocompatibility that makes them fair candidates for photo-crosslinking and living-system studies.

For the detailed definition and impact of molar mass and concentration of monomer on the polymerization/crosslinking procedure see chapter 3 section 3.1.1.

5.3. DLW of photo-thermally active proteinaceous microstructures

Two-photons assisted DLW, or in general multi-photon polymerization processes, do not rely on the local temperature increase due to the laser irradiation. In fact, these techniques that involve delivering high energy doses to the focal volume of the sample, can cause unwanted thermal processes which produce local damages and distortions while writing the micro-structures. This undesired effect follows from the heat dissipation from the laser spot which occurs over a time-scale of the order of $\tau_{heat} = d_{focus}^2 / \chi_{resin}$, where d_{focus} is the size of the domain heated by the focused laser and χ_{resin} indicates the thermal diffusivity of the resin. The thermal diffusion time-scale is way smaller (in the range of microseconds) than the polymeric chain propagation rate (see chapter 3 section 3.1.1)[3]. The generated heat would not affect the polymerization/crosslinking process, as the heat is rapidly dissipated while

---

[1] Robustness is often described as the structure's ability to avoid disproportionate collapse due to an initial damage

[2] The intrinsic fracture toughness of polymer networks, defined as the energy required to fracture a single layer of polymer chains

[3] The thermal diffusion time is however much longer than the source repetition time, about 10 ns, and it is therefore seen as an effective continuous source in this context.

scanning the ink, unless very large local heat release are generated in the TPC voxel. These considerations can be drawn from the physical chemical parameters of the conventional resins in use for which $\chi_{re\sin} \cong 10^6 \, \mu m^2/s$. However, the increase of the light power or the presence of photo-responsive molecules and/or physical systems in the resin/ink, like dyes and plasmonic nanoparticles, can dramatically increase the local release of heat and induce thermal effects in the ink. Apart from the large photo-thermal efficiency of non-spherical plasmonic nanoparticles in producing localized heat (chapter 4), also weakly fluorescent (low fluorescence quantum yield) dyes can generate, under considerable laser irradiance levels, localized heat that is not dissipated rapidly enough in the micro-environment and builds up a consistent temperature increase in the TPC voxel. These dyes can be classified as photothermal molecules or particles (e.g., Prussian Blue nanocrystals, Methylene Blue, and Malachite Green). It is quite clear then that the fabrication of microstructures that incorporate such photo-thermal composites is quite demanding from the experimental point of view.

In this thesis, the novelty in the DLW of proteinaceous microarchitectures comes from the success in fabricating microstructures by two-photon-assisted crosslinking of inks including the above-mentioned photo-responsive systems (i.e., [BSA-MB] and [BSA-RB]) and photo-thermally active gold nanoparticles (GNPs). Preliminary experiments on fabricating microstructures using the plasmonic inks of BSA ([BSA-MB] or [RB-GNP] with the addition of GNPs) suggested that a direct interaction between the two photo-initiators (RB or MB) and the gold nanoparticles may occur and hinder the possibility to reach the project goal. The trials proceeded then to investigate the photochemical behavior of the RB/GNP and MB/GNP complexes as it is addressed later on this chapter. It is noteworthy to remind that another condition that markedly affects the efficiency of the microfabrication of hybrid GNPs/protein structures and their properties is the matching of LSPR of GNPs (that depends on the particles shape and size) with the DLW wavelength $\lambda_{writing}$. In fact, this determines the minimum laser power for DLW and reduces any excessive thermal load to the voxel during writing. Because of this, different GNPs with different LSPR spectral positions were used to optimize the DLW conditions.

5.3.1. Anionic and Cationic photosensitizers interaction with GNPs

In a first approach, pegylated (the pegylation will additionally help to synthesize stable nanoparticles) gold-nanostars[4] (GNSs) were mixed at different ratios with the [BSA-MB] ink (ratio 1:3). The GNSs display two widely spaced LSPR resonance peaks, one at about 800nm (very close to [BSA-MB] $\lambda_{writing}$=780nm-800nm) and the other at about 1200nm. Two-photon-assisted DLW in a drop of [BSA-MB-GNSs] ink was not as successful as in the [BSA-

---

[4] The GNSs were pegylated using PEG-SH of MW=5000

MB] ink. At the best situation, DLW experiments produced only random and unstable crosslinked features. This is probably due to a strong specific interaction of the plasmonic nanoparticles with the MB dye. Indeed, there are studies that reveal the nature of the interaction of cationic and anionic dyes with GNPs [5, 6]. From these studies we can derive the idea that in the case of cationic the dyes (e.g., MB), there is a strong interaction with the dye molecule and nanoparticle which may cause agglomeration of nanoparticles.
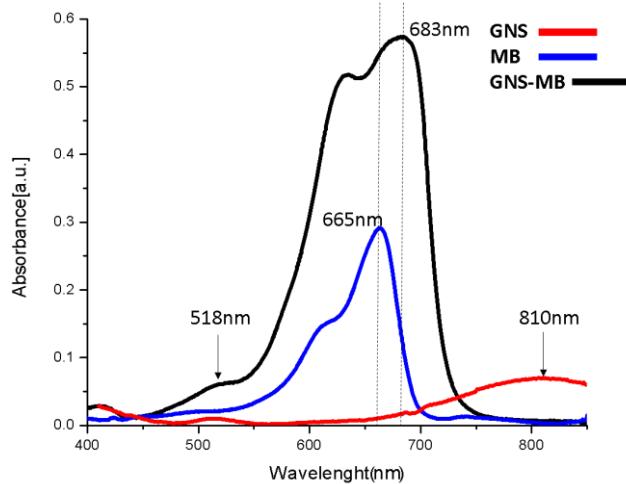
Figure 5.14. Absorption spectra of GNS (red line, 3 times diluted), MB (blue line), and GNS-MB mix (black line). The impact of presence of GNSs in absorption spectrum of the GNS-MB mixture complex can be understood by comparing the absorption spectrums (black and blue lines) and that unique shoulder at 518nm that is close to the GNPs LSPR peak (spherical GNPs).

This large nanoparticle-dye aggregations results in a red-shift (in this case ~20nm) and enhancement of the absorption rate of the ink complex, Figure 5.14, with a marked increase of the absorption cross-section of the MB dye. In Figure 5.14, this aggregation is demonstrated in terms of absorption spectrum from a diluted sample of ink composed of 150μL of [BSA-MB] and 50μL GNSs. However, the efficiency of the two-photons DLW was poor probably due to an enhanced photothermal effect triggered by the enhanced MB dye absorption (fluorescent quantum yield=0.04). The local release of heat prevented an efficient photo-crosslinking process. Even when using the best dispersed [BSA-MB-GNSs] ink and choosing the best writing conditions in our hands, $\lambda_{writing}$=780nm, scan rate of 1μm/s, average power <P>=100mW, we could not obtain sufficiently stable writing conditions as to fabricate continuous and robust proteinaceous microstructures. Finally, and equally relevant, Figure 5.14 shows that the LSPR peak at 800 nm disappears in the composite ink, indicating once more that an energy transfer process occurs between the GNS and the cationic MB dye.

On the contrary, the literature indications are that the interaction of anionic dyes (here RB) and GNPs can be at most marginal. It can be assumed that there is almost no electronic interaction between the nanoparticles and the dye molecules. Indeed, from the absorption spectra reported in Figure 5.15, one can infer that there is almost no impact of the gold nanoparticles on the absorption spectra of the photo-responsive system (here RB) and no massive agglomeration of the nanoparticles is present. Given these results, in order to limit the unwanted photothermal effect caused mainly by the absorption of radiation at $\lambda_{writing}$=780nm-800nm from the photo-initiator itself (through its plasmonic-enhanced absorption) and, marginally, from the gold nanoparticles (through its direct plasmonic absorption), we resolved ourselves to adopt in the DLW trials inks composed of BSA, the anionic dye RB, and gold-branched nanoparticles. The ink suspension was prepared using the former 1:3 dilution protocol (1 part plasmonic nanoparticle solution and 3 parts the proteinaceous ink in a total of 4 parts) to fabricate photothermally active microarchitectures via two-photon assisted DLW. It is worth noting from Figure 5.15 that the LSPR resonance of the GNSs is preserved in the composite ink. This is extremely important for the present project as it is the prerequisite to be able to fabricate a proteinaceous microstructure with photo-thermal activity.
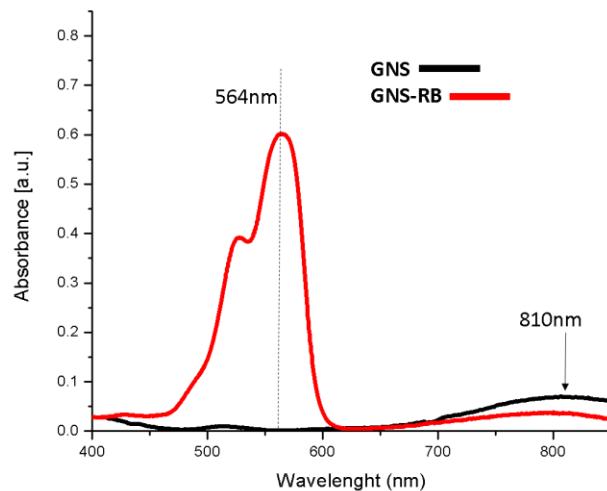
Figure 5.15. Absorption spectra of GNS-RB mix (red line) and solo GNS (black line).

Regarding the choice of the plasmonic nanoparticles, two types of gold nanoparticles, both branched, were used in the experiments of DLW fabrication of photothermally-active proteinaceous microstructures. The studies of the interaction of the gold nanoparticles with cationic and anionic photo-initiator, discussed above, were performed with a type of highly regular nanoparticles, called gold nanostars, GNS. These GNSs were synthesized as

described elsewhere [8]. They were then pegylated (PEG-SH, *MW* 5000) and diluted in the proteinaceous ink at 35% v/v. The GNS hydrodynamic radius is 26.5±3 nm (see Appendix-II) and TEM studies indicated a very regular penta-twinned planar structure with an arm length of about 32 nm in length [8]. As can be seen in Figures 5.14 and 5.15, the LPSR absorption of these nanoparticles lies at about 810 nm. A second type of less regular gold branched nanoparticles, called GBNP, was synthesized by using HEPES as a reducing and stabilizing agent according to the protocol given elsewhere [9] and further pegylated with 6000 *MW* thiol-PEG. The size of the GBNPs, measured by fluorescence correlation spectroscopy, is 39±4 nm (Appendix-II). The additional feature of GBNPs[5] with respect to GNSs is that GBNPs exhibit a single LSPR resonance at about 600nm (100nm down-shifted from the NIR range used to induce the two-photon excitation of the photo-initiator). The re-formulation of the proteinaceous ink with RB and with the above mentioned GNPs, made it possible to create adequate microstructures with measurable photothermal activity when irradiated with NIR and visible radiations.
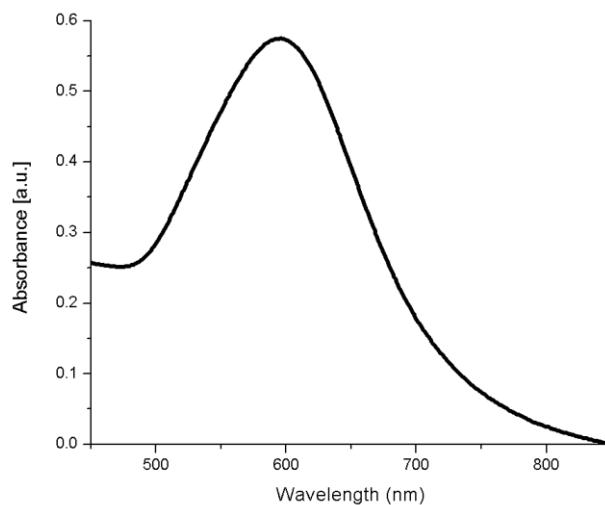
Figure 5.16. Absorption spectra of GBNPs in HEPES solution.

5.4. Characterization

5.4.1. Two-photon excitation fluorescence microscopy

Indeed, the proteinaceous microstructures were successfully fabricate with embedded gold nanoparticles (both GNSs and GBNPs) by adopting the RB dye as a photoinitiator. The

---

[5] Size measured through fluorescence correlation spectroscopy is estimated around $39 \pm 4 nm$

DLW of these active microstructures was carried out under the following conditions: $\lambda_{writing}$=800nm, average power <P>=120mW, and scanning rate 10µm/s (10 times faster than the case of [BSA-MBGNSs]). When characterized by means of TPE fluorescence microscopy, the microstructures free of GNSs display a uniform emission peak at 570nm originating from the residual dye in the cross-linked structure. On the images of the microstructures fabricated with the ink containing the GNSs, instead well distinct spots (see Figure 5.17 for exemplary data) were found with a broad fluorescence signal with a maximum at 440nm. We ascribed these structures, of the size of the microscope point spread function, to the two-photon excitation luminescence of the gold nanoparticles.
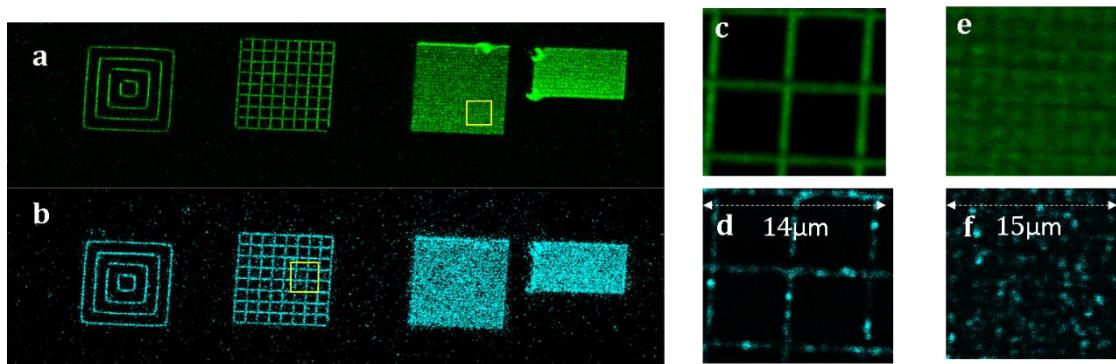
Figure 5.17. Two-photon fluorescence microscopy image of the microstructures written using the ink [BSA-RB-GNSs]: a) the green channel ($\lambda_{em} = 535 \pm 20nm$) reports the RB emission (550nm) and b) the cyan channel reports ($\lambda_{em} = 440 \pm 20nm$) a fraction of the two-photon luminescence emissivity of the GNSs on a 50µmx50µmx3.5µm fabricated microstructure. c-f) blow up of the yellow-marked regions in a and b.
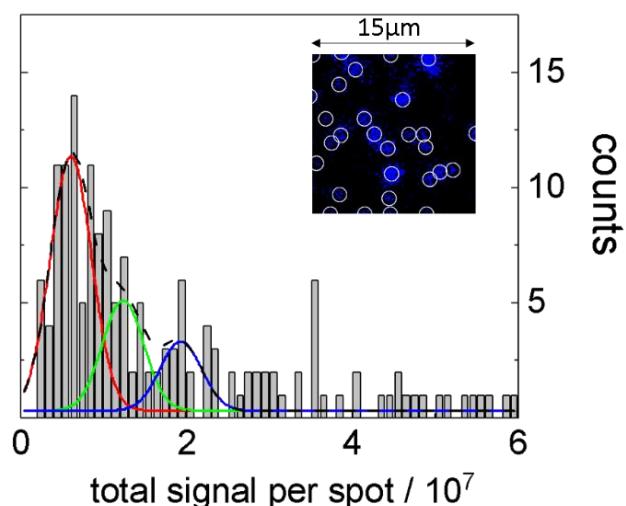
Figure 5.18. Distribution of the intensity per spot measured on the GNS emission channel of Figure 5.17f.

In order to ascertain the origin of the distinct spots visible in the GNPs doped micro-structures, the distribution of the 440 nm (GNS emission channel, Figure 5.17f) intensity per spot was measured. As can be judged from Figure 5.18 (colored solid lines), the distributions can be well described by a sum of (up to 3) Gaussian components. The distributions can be well described by a sum of (up to 3) Gaussian components. The lines are the best fit of three components Gaussian distribution to the data. The distributions of the intensity per spot reported in Figure 5.18 refer to a uniform squared array microstructure with a FOV= 15µmx15µm and an estimated thickness of 2.7µm. The inset plot in Figure 5.18 shows the segmentation of the spots ascribed to the GNPs on the microscopy image. The width of the three components was fit as a single parameter, giving $\sigma_I = 5 \pm 0.5 \times 10^6$. The maxima of the three components were fit independently and resulted $I_1 = 6.1 \pm 0.5 \pm 10^6$, $I_2 = 12.4 \pm 0.9 \pm 10^6$, and $I_3 = 19.4 \pm 1.5 \pm 10^6$. The ratios of $\frac{I_2}{I_1} = 2 \pm 0.2$ and $\frac{I_3}{I_1} = 3.2 \pm 0.4$, which are close to small integer numbers, suggests that the three components corresponds to single GNSs and their dimers and trimmers, respectively. The relative computed percentages from the area of the corresponding components are 58%, 26%, and 16%, respectively. The number of particles per unit volume is 0.27 ± 0.03 particle per µm-3, a value that is close to the nominal concentration of the GNSs in the fabrication ink $\cong 0.4 \pm 0.1$ particle per µm-3.

5.4.2. Thermal-imaging

Having being able to produce a putative photothermal microstructure, it was necessary to devise a high spatial resolution thermal imaging method to verify and characterize the photo-thermal activity of the DLW structures. More than a thermal-imaging method, we pursued to develop an imaging system that exploits the photo-activated thermal emission from the gold NPs that act as hot spots emitting thermal radiation and spaced a few micrometers from each other.

Non-contact thermographic imaging maps the intensity emitted by the sample (and here arising from photo-activated plasmonic nanoparticles) in the far infrared (~7-14µm; thermal radiation) region of the spectrum by means of an array of micro-bolometeres (thermo-camera, see chapter 4). It exploits the Stephan-Boltzman law that states that the radiance of a gray-body of emissivity ε ($0 < \varepsilon < 1$) at temperature T is $R = \varepsilon\sigma T^4$, where $\sigma = 5.67 \times 10^{-8}\ Wm^{-2}K^{-4}$ is the Stephan-Boltzman constant. The array of micro-bolometer, coupled to a Germanium conjugating optics, allows to monitor in space and time (x, y; t) the sample radiance, and infer from this the temperature (x,y;t) provided the emissivity is known. Typical resolutions are ~10ms in time and $\cong$ 200-300 µm in space. The poor spatial and time resolutions are due to the very low numeral aperture of the Germanium optics, typically N.A $\cong$ 0.05. Actually, the

spatial resolution achieved on the field is even worst, about 1 mm, due to the thermal diffusivity in the sample.

Given these premises, an alternative thermo-imaging method was developed that we named active photothermal imaging. In brief, high spatial resolution imaging of the thermal emission from the fabricated micro-patterns was achieved by sparsely priming the heat release from the sample with a spatially structured and time modulated laser illumination. An asynchronous thermal video was acquired at 30 Hz frame rate by a low-cost thermo-camera and on each frame we identified the absorptive centers based on a localization algorithm of the isolated laser-induced hot spots based on a multi-Gaussian fit. By focusing visible radiation, even with a low numerical aperture optics (N.A $\cong 0.3$), we are able to prime the absorption in a well-defined micrometer size area on the sample that determines the spatial resolution of the final reconstructed mapping of the thermal emission. With this method we were able to reach sub-wavelength ($\lambda \cong 12\ \mu m$) spatial resolutions of the order of 100 nm [23].
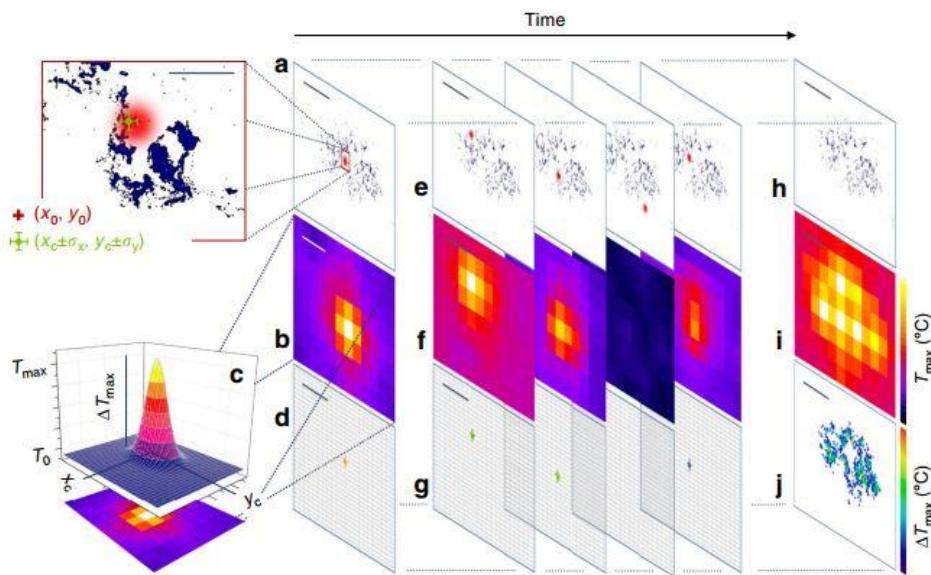
Figure 5.19. Photo-activated thermal imaging at sub-diffraction resolution of an explanted murine skin biopsy treated with 30 nm Prussian Blue nano-cubes. Scale bars (100 μm in the magnification of "a" panel, and 1000 μm elsewhere). Adopted from reference [23].

With this purpose, a CW TEM$_{00}$ laser beam of variable average power with wavelength lying within the sample absorption band (here GNP's LSPR resonance range) was focused on the sample so to reach a beam variance of ω_0^2, Figure 5.19. In this approach, a single square-wave excitation pulse of duration τ_{on} is focused on the sample at the position (x_0, y_0). If the laser beam impinges on light absorbing and heat releasing features, an approximately Gaussian 2D temperature distribution is observed in the acquired thermo-camera images.

The time evolution of the Gaussian amplitude obeys an exponential rise and decay law, with the maximum value found at the τ_{on}, when the laser is switched off and steered to another position before being again switched on. A non-linear 2D Gaussian fit of the temperature peak on the thermal image acquired at time τ_{on} provides the temperature $\Delta T_{max} = T_{max} - T_0$ in excess over the equilibrium sample temperature T_0, together with the Gaussian center coordinates (x_c, y_c). Importantly, x_c and y_c identify the center of the distribution of the absorbing objects within the area assigned by the excitation laser spot size. For a given thermo-camera pixel size, the uncertainty σ_x, in the determination of the best fit coordinates $(x_c,)$ is a function of the number of collected infrared photons and can be made arbitrarily small down to the typical visible optical resolution, $\cong 1\ \mu m$, by increasing the laser power, that directly determines the temperature variations, and by maximizing the fraction of the collected thermal emission (by means of larger NA conjugating Germanium lenses). Obviously, this result can be reached at the expenses of the experimental duration because it implies the use of smaller laser spots with the consequent increase of the number of "pixels" in the reconstructed image.

However, the localization of absorbing objects can be performed well below the theoretical resolution limit sets by the diffraction of far infrared radiation by the thermal camera collecting lens, which in our hands is $\cong \frac{\lambda_{therm}}{NA} \cong \frac{12\ \mu m}{0.05} = 240\ \mu m$. This theoretical figure is much worsened by the pixel size of the thermo-camera and the thermal diffusion (typical thermal diffusivity values are $D_{therm} = 10^6\ \mu m^2/s$). In fact, the pixel size, d_{pix}, of the thermo-camera projected on the sample plane is about $400\ \mu m$, about twice the theoretical value, and the thermal diffusion time over the pixel is $\tau_{therm} = \left(\frac{d_{pix}}{2}\right)^2 \frac{1}{D_{therm}} \cong 40\ ms$, of the same order of our image acquisition time. This implies that in a few frames the information on the thermal emission will be distributed over many adjacent pixels. Experimentally, as presented later in this chapter, the effective spatial resolution of the thermal image on our samples is of the order of 1 mm. Our raster scanning photo-activation thermal imaging approach will overcome both these effects providing us with a sub-wavelength resolution.

Additional details on the scanning and imaging algorithms can be found in the reference [23]. In brief, this thermo-imaging method relies on the raster scanning of the sample (see Figure 5.19) with a Gaussian laser beam (red spot in panel "a"), which is focused on the sample and temporarily parked at the position (x_0, y_0) for a duration τ_{on} after which the laser is switched off and moved to another parking position, and so on, in a raster profile. The parking position (x_0, y_0) is therefore a function of time and perform, at the end of the algorithm, a sparse complete coverage of the sample with a predetermined x and y spacing. The light absorbing

features (blue region), when hit by the laser spot, induce a local temperature increase, which is measured by the thermo-camera as a growing 2D Gaussian peak. A Gaussian fit of the frame collected at time τ_{on} (panels "b" and "c") provides the temperature variation $\Delta T_{max} = T_{max} - T_0$ at the parking position (x_0,y$_0$) and provide the peak coordinates ($x_c \pm \sigma_x, \pm \sigma_y$) that localizes the center of the distribution of absorbing objects within the laser spot size. These coordinates may not coincide with the parking position. The procedure will be repeated over sets of isolated points as the laser is scanned over the sample (exemplified in Fig.5.19e and Fig.5.19f). The center coordinates provided by the Gaussian fit of temperature profiles stored on the thermal image reveals the position of the absorbing features on the scan grid (Fig.5.19-d and Fig.5.19-g) with the above-stated uncertainty σ_x. The positions obtained by the fit of each frame are then used to build the synthetic thermal image in which a color, coding for the value of the best fit ΔT_{max}, is assigned to each pixel. The maximum projection of all the raw thermal images collected during the full scan of the sample provides a low (~mm) resolution image of sample (Fig. 5.19- i), whereas the maximum projection of the stack containing all the localized absorptive centers provides the super-resolution image of the scanned region (Figure 5.19-j and Figure 5.19-h). This methodology allowed to image photo-thermally active substrates with a resolution below the thermal diffraction limits, and appropriately optimized in house by the author and colleagues, was employed to investigate the photothermal functionality of the fabricated microarchitectures as discussed below.

In the first approach to characterize the photothermal activity of fabricated proteinaceous features contain GNSs and GBNPs using the thermo-camera, the Ti:Sapph laser source was tuned in pulsing mode at 760nm $\leq \lambda \leq$ 800nm. The temperatures profiles in Figures 5.20a and 5.19b show the temperature kinetics of two different fabricated proteinaceous microstructures [BSA-RB-GNSs] (Figure 5.20a) and [BSARB-GBNPs] (Figure 5.20b) using the same NIR pulsing laser source tuned at different wavelengths and average powers. The Figure 5.20a, shows the temperature increase of the uniform 20µmx20µmx3µm parallelepiped microstructure under continues irradiation with the NIR pulsed laser tuned at 800nm. The temperature increase, monitored in time with the thermo-camera, was fitted to an exponential growth (solid line) at <P>=100mW (squares), 80mW (circles), and 30mW (up triangles). The raising time, used as a single global fitting parameter for the three measurements was $\tau = 0.75 \pm 0.03 s$ (Figure 5.20a). In any case, we found that the rising time was relatively insensitive to the laser power in the range 20 mW – 100 mW. The limiting temperature increase $\Delta T_{\omega=0}$ as a function of average power can be fit (Figure 5.20a, inset) to the following linear ramp: 20.0 $\pm$ 3 $\langle P \rangle_{pulsed}$ (Power in Watts) that corresponds to a photothermal efficiency of $\frac{\partial \Delta T_{\omega=0}}{\partial <P>_{pulsed}} = 20 \pm 3 \, ^{o}C \, W^{-1}$.
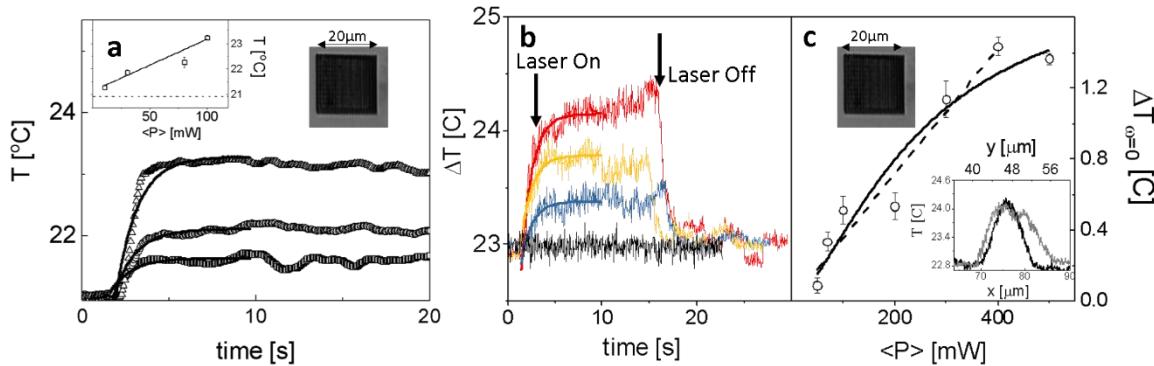
Figure 5.20. Recorded photothermal effect from a) GNSs embedded with proteinaceous microstructure under irradiation of pulsed laser at 800nm, b) and c) GBNPs in the same proteinaceous ink configuration with irradiation of pulsed NIR at 770nm.

The difference in the photothermal efficiency of the microstructures fabricated with the two types of nanoparticles can be gained from a comparison of the temperatures profiles in Figures 5.20a and 5.20b that report the temperature kinetics of proteinaceous microstructures fabricated in the [BSA-RB-GNSs] (Figure 5.20a) and [BSA-RB-GBNPs] (Figure 5.20b) ink, under irradiation of the same NIR pulsing laser source tuned at different wavelengths and average powers. The Figure 5.20a, shows the temperature increase of the uniform 20μmx20μmx3μm parallelepiped microstructure under continued irradiation with the NIR pulsed laser tuned at 800nm and corresponds to photothermal efficiency of about 20°C/W, as discussed above.
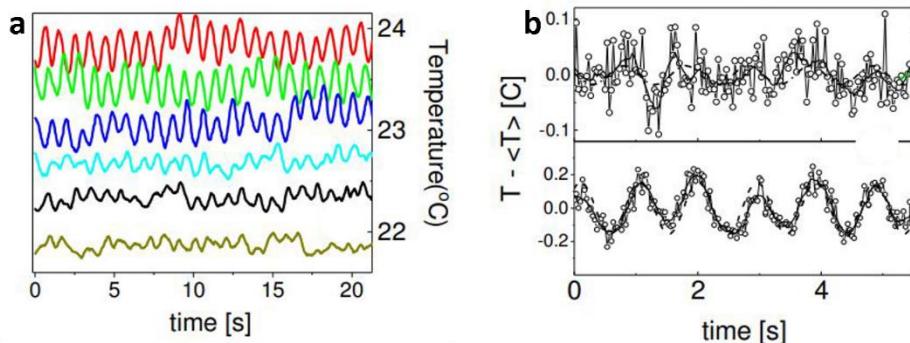
Figure 5.21 a) Temperature response under modulated NIR pulsed irradiation at frequency ~1Hz and various <P>= 70, 100, 200, 300, 400, and 500mW, b) harmonic fit of the data at <P>=70mW (upper plot) and 300mW (lower plot) measured on [BSA-RB-GBNPs] microstructures.

Due to the low photothermal efficiency of GBNPs at $\lambda_{exc} = 760nm$, as shown in Figure 5.20b, the photo-thermal effect on the GBNPs containing microstructures was better characterized by modulating the excitation intensity with a mechanical shutter at a frequency close to the reciprocal of the growth time $\frac{1}{\tau}$ ($\tau = 1.16 \pm 0.03s$). The temperature signal on the thermo-

camera is modulated as the same frequency as the irradiation light. The analysis of the temperature oscillations to a harmonic function $\Delta T_{max}(\omega)\sin(\omega t + \varphi(\omega))$, as done for example in Figure 5.21b by keeping the frequency fixed at $f = 1.05 Hz$, provides the temperature amplitude $\Delta T_{max}(\omega)$ as a function of the irradiation power, Figure 5.20c. The trend of the amplitude, to a high approximation (dashed line in Figure 5.20c), is linear with a slight round off at $<P> > 400 mW$ (solid line in Figure 5.20c). In addition, by taking into account the Fourier filter contribution at the experimental pulsation[6] $\omega \cong 2\pi \frac{rad}{s}$, the amplitudes $\Delta T_{max}(\omega)$ are in good agreement with the plateau values $\Delta T_{\omega=0}$.

Figure 5.20c accordingly reports the trend of $\Delta T_{\omega=0}(\omega) = \Delta T_{max}\sqrt{1 + \omega^2 \tau^2}$ as a function of average excitation power $<P>_{pulsed}$ where the dashed line is best linear fit to the data with the average slope of $\frac{\partial \Delta T_{\omega=0}}{\partial <P>} = 3.5 \pm 0.2 \, {}^oC/W$. For a comparison the photothermal efficiency for the [BSA-RB-GNSs] microstructures was $\frac{\partial \Delta T}{\partial \langle P \rangle_{pulsed}} = 20 \pm 3 \, {}^oC/W$. A logistic curve (solid line) can also fit the data reported in Figure 5.20c, partially accounting for the round-off above P= 400 mW.

In Figure 5.21b, the dashed lines are best fit of the harmonic function $\Delta T_{max}\cos(2\pi f t + \varphi)$ with the frequency best fit of $f = 1.05 \pm 0.03 Hz$. These measurements then revealed that the temperature increase was indeed due to the NIR absorption of GNSs in the microstructures, as confirmed by the temperature profile across the features in the focal plane (see inset in Figure 5.20c). These results were obtained by irradiating the nanoparticles embedded in the proteinaceous microstructures with a pulsed laser (duty cycle $d_c \cong 2 \times 10^{-5}$) at an effective intensity of $\frac{\langle I \rangle}{\sqrt{d_c}} \cong 50 - 150 \, kW/cm^2$).

This high value would make the routine application of the photo-thermal action of the microstructures unfeasible. In another strategy, the photo-thermal efficiency of proteinaceous microstructures fabricated in [BSA-RB-GNSs] inks was measured under continuous-wave (CW) laser irradiation (Figure 5.21) with the same thermography methods used for the pulse laser irradiation studies. Under CW irradiation, the temperature kinetics of the microstructures was similar to that measurement under pulsed laser irradiation, and could be fit as an exponential growth with a rising time $\tau = 1.58 \pm 0.02 s$, independent of the excitation power in the range 100-200mW. However, the photothermal efficiency lowers to $\frac{\partial \Delta T}{\partial \langle P \rangle_{CW}} = 1.7 \pm 0.2 \, {}^oC/W$, about ten times lower than what measured under pulsed excitation.

---

[6] $\Delta T_{max}(\omega) = \frac{\Delta T_{\omega=0}}{\sqrt{1 + \omega^2 \tau^2}}$

Apart from these photothermal characterizations of the plasmonic nanoparticles embedded in photo-crosslinked proteinaceous structures and its dependence on the irradiation mode, either under pulsed or CW, one can surmise that the photothermal efficiency is directly influenced also by the concentration of nanoparticles within the microstructures. However, tuning the concentration of nanoparticles in the ink toward higher ratios is not an easy task because this implies a large thermal load on the developing ink during laser writing due to the vicinity of the plasmonic resonance of the GNSs with the laser writing wavelength. To overcome this drawback, there were two options: either to increase the thickness of the microstructure, or using nanoparticles with a well-defined LSPR above 850 nm, to avoid superimposing with the laser writing wavelength.
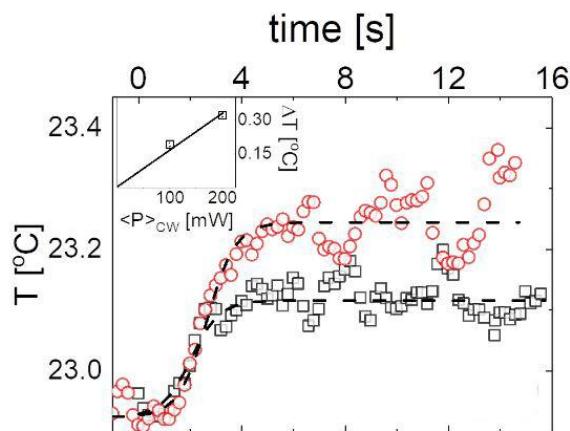
Figure 5.22. Time and power (inset) dependence of the temperature induce from [BSA-RB-GNSs] microstructures under irradiation of a CW laser at 800nm; black squares correspond to the average power of 100mW and red circles to 200mW.
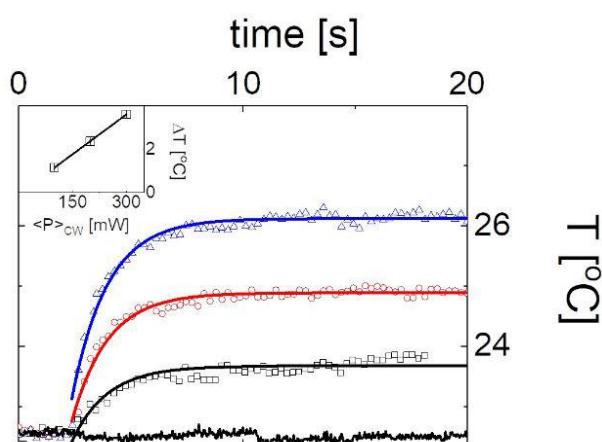

Figure 5.23. Time and power (inset) dependence of the temperature recorded from [BSA-RB-GNSs] mesostructures (1mmx3mmx0.1mm) fabricated with the CW Ar-laser. The photothermal efficiency was analyzed using Ti:Sapph laser source on the CW mode with irradiation average powers of $< P >_{CW}$=100mW (black squares), $< P >_{CW}$=200mW (red circles), and $< P >_{CW}$=300mW (blue triangles). The solid lines are the best fit to an exponential growth.

The first solution was carried out by implementing single photon cross-linking in the same [BSA-RB-GNSs] inks. In this condition, the ink drops irradiated with the Ar-laser at 514nm at $<P>\sim20mW$ undergo photo-crosslinked due to the single photon absorption of photo-responsive molecules, RB dye, at 562nm. These large-scaled microarchitectures, here called mesostructures, presented a photothermal efficiency of $\frac{\partial \Delta T}{\partial \langle P \rangle_{CW}} = 12.2 \pm 0.4\ ^{o}C/W$, almost seven times higher than the photothermal effect in the proteinaceous microstructures. The temperature kinetics are reported in Figure 5.23.

The temperature increase then was mapped on these mesostructures, whose size are 1x1x0.1 mm³ (see Figure 5.24a). The use of the high spatial resolution photo-thermal imaging methods discussed in Figure 5.19, allowed to derive the temperature map reported in Figure 5.24b.
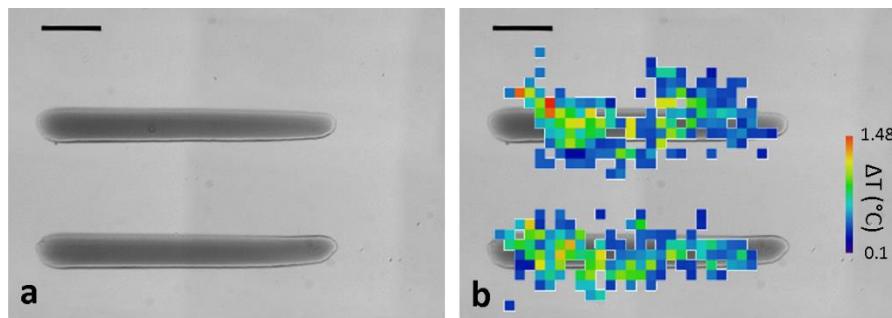

Figure 5.24. a) Single-photon assisted DLW of [BSA-RB-GNS] (parallelepiped) and b) high resolution thermal-imaging recorded from the written parallelepiped. Scale bars are 200µm.
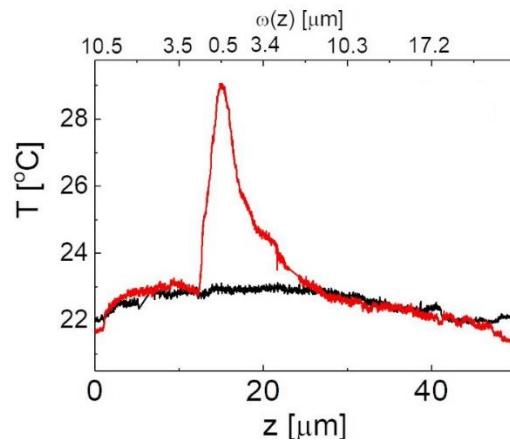

Figure 5.25. Photothermal effect measured in [BSA-RB-GNS] microstructure (filled square 50µmx50µm), under irradiation wavelength of 800nm and average power of <P>=300mW, as a function of laser modes: CW (black) and pulsed (red). Upper x-axis is the beam size on the microstructure sample and lower x-axis presents the z-scan along the optical axis.

For application purposes, we need also to demonstrate that the thermal load can be induced over extended (tens of micrometers) areas. Figure 5.25 reports data that indicate that the photothermal effect can indeed be induced over extended irradiation areas. A 50µm² filled square of [BSA-RB-GNS] was subjected to a thermographic analysis while scanning the laser

beam over the optical axis (z-scan) under irradiation with different laser modes (CW, or pulsed). A temperature increase of 1.1 ± 0.05 ^{o}C was detected over the range $0.45\mu m \leq \omega(z) \leq 15\mu m$ of the irradiation beam size (upper x-axis in Figure 5.25) under CW mode at <P>=300mW. In pulsing mode, employing the same strategy and average laser power, the maximum detected temperature raised to 7.0 ± 0.06 ^{o}C (Figure 5.25, red curve).

5.5. Cell Studies

One fulfilled milestone of this project was to fabricate miniaturized photothermally-active proteinaceous structures by employing single-photon and two-photon-assisted DLW methods. This result was then transferred to the final stage which was to investigate the interaction of living-system and organisms (i.e., cells or bacteria) with the printed microarchitectures. For this reason, both microstructures and mesostructures were examined under different cell-culture mediums.
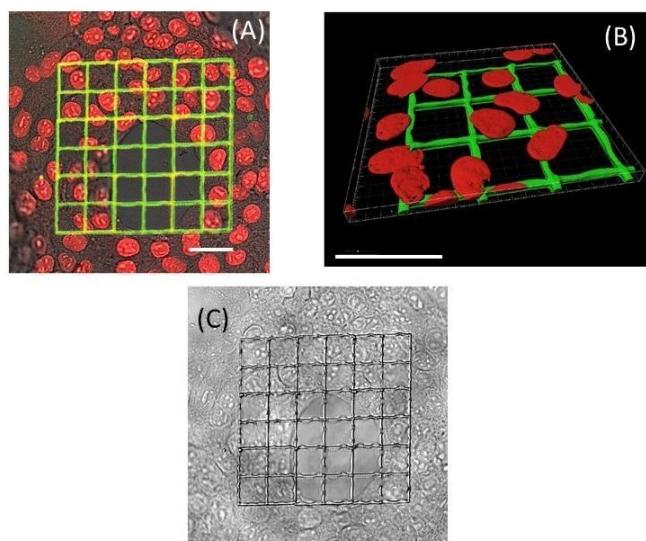

Figure 5.26. 4T1 cell culture on [BSA-MB] microstructures, scale bars 10μm. (A) confocal image of 4T1 cells (stained nuclei is the red-channel, $\lambda_{em} = 681nm$) and MB dye (green channel, $\lambda_{em} = 665nm$), (B) 3D reconstructed image, and (C) transmission image of 4T1 cells grown (48 hours) on microstructures.

In the first approach, the fabricated [BSA-MB] microstructures were seeded with the triple negative breast cancer cells, 4T1. The 4T1 cell line first was cultured in IMDM-10 complete medium: IMDM, 10% heat-inactivated FBS (EuroClone), 2mM 1-glutamine, 100 U/mL penicillin, and 100μg/mL streptomycin. The grid-like parallelepiped microstructures were fabricated using TPC-assisted DLW technique on a 35mm petri dish with cover glass bottom (MatTek, MA, USA). The 4T1 cell line was cultured till the confluence reached 70%. The printed microstructures were seeded with a drop of 4T1 cells with the 48 hours incubation time. Afterward, the cells were fixed using 4% paraformaldehyde (PFA) and the nuclei were stained with Draq5 dye. Figure 5.26 shows the 4T1 cells adhesion situation on top of the

fabricated [BSA-MB] microstructures and support the conclusion that no dramatic cytotoxicity was observed on the 4T1 cell when seeded on the microstructures.

We then studied the interaction of cell lines with proteinaceous mesostructures. To this purpose, a mesostructure fabricated in the [BSA-RB] ink via single-photon-assisted DLW was cultured with NIH-3T3 fibroblast cell line. NIH-3T3 cells was routinely cultured in high-glucose Dulbecco's modified Eagle medium supplemented with 10% calf serum, 100 U/ml penicillin, and 100µg/ml streptomycin. The printed mesostructure, hashtag-like, was seeded with a drop of 70% reached confluence NIH-3T3 cell culture with an incubation time of 48 hours, and then fixed with 4% PFA. The fluorescence confocal microscopy, Figure 5.27, demonstrates that the fibroblast cells adhered to the mesostructure's side edges. One can surmise from this finding that the height of the printed hashtag (~100µm) is too large for the fibroblast cells to reach and grow on top-surface. However, we did observe that in some regions the cells tried to climb up and populate the top-surface.
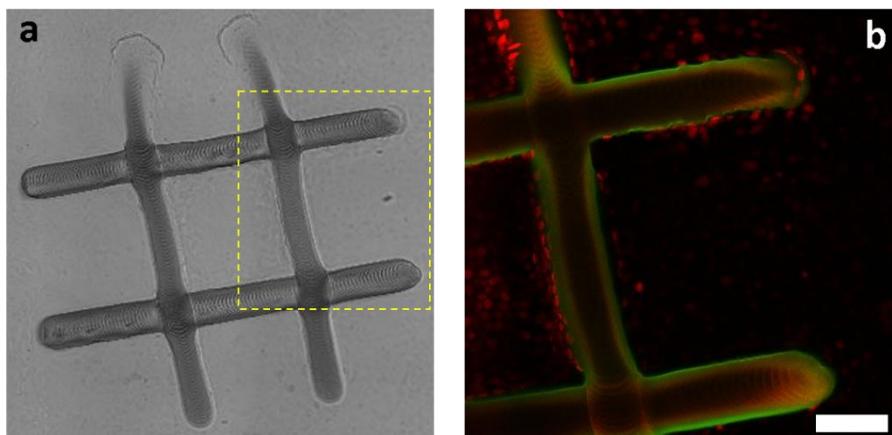

Figure 5.27. Confocal images of [BSA-RB] printed hashtag-mesostructure. (a) shows the transmission image, and (b) fluorescence image of the dashed rectangle in panel a, red channel represents the NIH-3T3 cell nuclei stained with propidium iodide ($\lambda_{em} = 636nm$) and green channel is the RB dye residues ($\lambda_{em} = 560nm$). Scale bar is 100µm.

5.6. Conclusion

This project has paved a way to the fabrication via DLW of miniaturized proteinaceous architectures (feature sizes of hundreds of nanometer to hundreds of micrometer) endowed with photo-thermal activity. These tiny features were printed from inks containing non-spherically symmetric gold nanoparticles which consequently gave the fabricated microstructures the property of being photothermally activated by means of NIR radiation. The preservation of the photothermal activity of the GNPs in the proteinaceous photoresists appears to be in very close relation with the electrochemical property of the dye (i.e., cationic or anionic) used as photo-initiator in the photoresist. We reached this conclusion by testing

both cationic (Methylene Blue) and anionic (Rose Bengal) type of dyes that have also different activation routes of radical species, to find a suitable formulation of the micro-structuration ink. We found that the fabrication of photothermally active microstructures was only possible when using the Rose Bengal dye. Moreover, these optimization approaches led us to investigate different dyes to proteins ratios and to assess that the value of this ratio largely determines the microarchitecture Young's modulus allowing us to change it over a wide range (80kPa to 800kPa). The accessibility to this wide range of elasticity makes these microstructures suitable for various tissue-engineering and regenerative medicine applications.

As stated above, successful fabrication of proteinaceous structures (both microstructure and mesostructure) was carried out using two types of non-spherical gold nanoparticles, GNSs (flat penta-twinned nanostars) and GBNPs (branched sea-urchin like particles), mixed with [BSA-RB] ink. By using focused CW laser on microstructures (thickness ~ 3µm) of [BSA-RB-GNSs], a photothermal efficiency of $\frac{\partial \Delta T}{\partial <P>_{CW}} = 1.7 \pm 0.2°C/W$ was recorded. This value raised to $\frac{\partial \Delta T}{\partial <P>_{CW}} = 12.2 \pm 0.4°C/W$ by using the same ink and excitation laser but on mesostructure (thickness ~ 100µm). On the other hand, the temperature increase arising from the thin microstructures of [BSA-RB-GBNPs] reached only $\Delta T = 1.1 \pm 0.05°C$. These records showed dependency of efficient photothermal effect to parameters like sample thickness, and nanoparticle's concentration. Increasing the value of these parameters result in higher local temperature gradient. These notable results came from gold concentration at the order of $\cong$ $0.01\% w/w$ in the microstructures that indicates approximately 0.4 ± 0.1 particle per µm³ (particle-particle distance$\cong$1.5µm). It is noteworthy to mention that this value could be increased to about 10 particles per µm³ (particle-particle distance$\cong$0.50µm), without running into the risk of massive aggregation and plasmon delocalization among nearby nanoparticles.

All in all, both of these fabricated microstructures and mesostructures of [BSA-RB-GNPs] are candidates to host cell and bacteria cultures to investigate the effect of local temperature increase on the fate of these living-organisms. We can envision the possibility to modulate several cellular processes, like adhesion, growth rate, differentiation, proliferation, etc., by tiny temperature change. On the other hand, working on meso-structures, we can predict a possible anti-bacteria effect obtained by reaching high temperature jumps possibly combined with chemical stresses like singlet oxygen formation. These tasks are currently under way in our laboratory.

5.7. Future outlook

Nowadays, at the end of 2020, there is a huge amount of research topics that are employing, either directly or indirectly, additive manufacturing strategies for studying living-system functionalities and subsequently use them to promote human-related health technologies. The present project wants to follow this research avenue by giving the fabricated structures extra functionalities, in this case photothermal effect that can be triggered remotely using NIR and IR range of the spectrum. As summarized throughout this thesis, this idea now has reached a milestone where microstructuration by means of DLW can be employed to fabricate fine photothermally active proteinaceous microarchitectures down to the tens of micrometer feature size with wide range of elastic modulus. The effect of local temperature increase on the differentiation of cells is currently under investigation and is the topic of another ongoing PhD thesis that has the specific aim to <u>characterize the effect of tiny temperature increase (1-2 ^{o}C) on cells growth and differentiation using the local photothermal effect</u> <u>induced by the embedded GNPs</u>.

To study the cells response and interaction with the printed proteinaceous feature containing RB dye and gold nanoparticles, one factor that needs to be evaluated is the cytotoxic effects. A major issue in this research line could be reactive oxygen species (ROS) like singlet oxygen induced by the tracer quantities of the RB dye remained in the printed structure. The photoexcitation of the RB dye (holding a high singlet oxygen quantum yield) can induce ROS which are known to damage cells and cause the activation of the inflammatory response. As an optimization step for laser-induced local temperature increase, <u>ROS inhibition and screening are mandatory strategies to</u> <u>minimize the cytotoxicity for the cell studies</u>. On the other hand, the efficiency of the RB dye to act as a singlet oxygen generator can be exploited, as another line of study, for antibacterial purposes with the idea of <u>printing proteinaceous antibacterial substrates</u>.

Finally, there are three major goals that the author wants to suggest as possible follow-up, each of which could be taken as a single full research project:

- Micro-engineered 3D hydrogel scaffolds for spatiotemporal analysis of viral infection

- 3D-printed optics for intravital bioprinting
- Quasi-3D microarchitectures for neural tissues differentiation.

5.8. References

[1] Ludvíková, L., Štacko, P., Sperry, J., & Klán, P. (2018). Photosensitized cross-linking of tryptophan and tyrosine derivatives by rose Bengal in aqueous solutions. *The Journal of Organic Chemistry*, *83*(18), 10835-10844.

[2] Allen, R., Nielson, R., Wise, D. D., & Shear, J. B. (2005). Catalytic three-dimensional protein architectures. *Analytical Chemistry*, *77*(16), 5089-5095.

[3] Fischer, B. B., Krieger-Liszkay, A., & Eggen, R. I. (2004). Photosensitizers neutral red (Type I) and rose Bengal (Type II) cause light-dependent toxicity inChlamydomonas reinhardtiiand induce theGpxhGene via increased singlet oxygen formation. *Environmental Science & Technology*, *38*(23), 6307-6313.

[4] Fuentes-Lemus, E., Mariotti, M., Hägglund, P., Leinisch, F., Fierro, A., Silva, E., López-Alarcón, C., & Davies, M. J. (2019). Binding of rose Bengal to lysozyme modulates photooxidation and cross-linking reactions involving tyrosine and tryptophan. *Free Radical Biology and Medicine*, *143*, 375-386.

[5] Kitching, H., Kenyon, A. J., & Parkin, I. P. (2014). The interaction of gold and silver nanoparticles with a range of anionic and cationic dyes. *Phys. Chem. Chem. Phys*, *16*(13), 6050-6059.

[6] Narband, N., Uppal, M., Dunnill, C. W., Hyett, G., Wilson, M., & Parkin, I. P. (2009). The interaction between gold nanoparticles and cationic and anionic dyes: Enhanced UV-visible absorption. *Physical Chemistry Chemical Physics*, *11*(44), 10513.

[7] Liu, J., Zheng, H., Poh, P., Machens, H., & Schilling, A. (2015). Hydrogels for engineering of Perfusable vascular networks. *International Journal of Molecular Sciences*, *16*(7), 15997-16016.

[8] Pallavicini, P., Donà, A., Casu, A., Chirico, G., Collini, M., Dacarro, G., Falqui, A., Milanese, C., Sironi, L., & Taglietti, A. (2013). Triton X-100 for three-plasmon gold nanostars with two photothermally active NIR (near IR) and SWIR (short-wavelength IR) channels. *Chemical Communications*, *49*(56), 6265.

[9] Lv, W., Gu, C., Zeng, S., Han, J., Jiang, T., & Zhou, J. (2018). One-pot synthesis of multi-branch gold nanoparticles and investigation of their SERS performance. *Biosensors*, *8*(4), 113.

[14] S., N., Easwaramoorthi, S., Rao, J. R., & Thanikaivelan, P. (2019). Probing visible light induced photochemical stabilization of collagen in green solvent medium. *International Journal of Biological Macromolecules*, *131*, 779-786.

[15] Wei, S., Liu, J., Zhao, Y., Zhang, T., Zheng, M., Jin, F., Dong, X., Xing, J., & Duan, X. (2017). Protein-based 3D microstructures with controllable morphology and pH-responsive properties. *ACS Applied Materials & Interfaces*, *9*(48), 42247-42257.

[16] Torgersen, J., Qin, X., Li, Z., Ovsianikov, A., Liska, R., & Stampfl, J. (2013). Hydrogels for two-photon polymerization: A toolbox for mimicking the Extracellular matrix. *Advanced Functional Materials*, *23*(36), 4542-4554.

[17] Hu, Y., Liu, Y., Zhao, R., Dong, J., & Qu, S. (2006). Spectroscopic studies on the interaction between methylene blue and bovine serum albumin. *Journal Of Photochemistry And Photobiology A: Chemistry*, *179*(3), 324-329. doi: 10.1016/j.jphotochem.2005.08.037

[18] Turbay, M. B., Rey, V., Argañaraz, N. M., Morán Vieyra, F. E., Aspée, A., Lissi, E. A., & Borsarelli, C. D. (2014). Effect of dye localization and self-interactions on the photosensitized generation of singlet oxygen by rose Bengal bound to bovine serum albumin. *Journal of Photochemistry and Photobiology B: Biology*, *141*, 275-282.

[19] Stochino, F., Bedon, C., Sagaseta, J., & Honfi, D. (2019). Robustness and Resilience of Structures under Extreme Loads. *Advances in Civil Engineering*, *2019*.

[20] Zhao, X. (2017). Designing toughness and strength for soft materials. *PNAS*, *114*(31), 8138-8140.

[21] Lin, D. C., Dimitriadis, E. K., & Horkay, F. (2006). Robust strategies for automated AFM force curve analysis—I. non-adhesive indentation of soft, inhomogeneous materials. *Journal of Biomechanical Engineering*, *129*(3), 430-440.

[22] Khan, A., Philip, J., & Hess, P. (2004). Young's modulus of silicon nitride used in scanning force microscope cantilevers. *Journal of Applied Physics*, *95*(4), 1667-1672.

[23] Bouzin, M., Marini, M., Zeynali, A., Borzenkov, M., Sironi, L., D'Alfonso, L., Mingozzi, F., Granucci, F., Pallavicini, P., Chirico, G., & Collini, M. (2019). Photo-activated raster scanning thermal imaging at sub-diffraction resolution. *Nature Communications*, *10*(1).

Appendix-I

Refraction of the laser during DLW

The printed BSA proteinaceous microstructures are possibly among the features that demonstrate high refractive index, regarding the estimations have been shown elsewhere[1]. The presented protocol, estimates the refractive index of BSA, with relation to the protein concentration (here C=300mg.mL^{-1}), n_{BSA}=1.44 at 20°C. During the DLW, the beam scans the sample plane with respect to the piezo-stage movement in XYZ axis. There are moments of DLW that structuration of a new plane or feature that is synchronized by beam passing over the already printed regions. This occasion is followed by the so-called beam refraction that can be arisen from two possible scenarios: either the low curvature of the bottom of the printed microstructures at the glass-microstructure interface (bottom-case), or top-surface curvature of the microstructures (top-case).
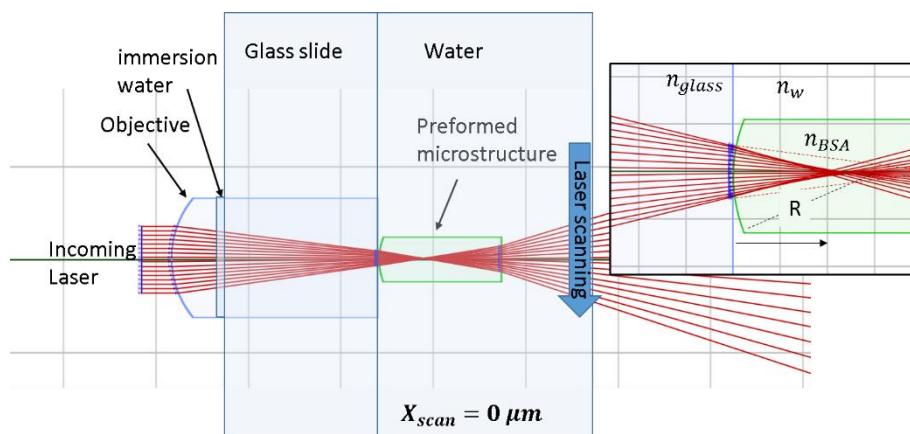

Figure 1. Sketch of the laser beam refraction from a microstructure in the case of the curvature on the bottom surface, facing the glass slide. The optical path was simplified by describing the objective with a single lens (blue). The microstructure is sketched as a green parallelepiped with one hemispherical side of radius $R \cong$ 2-6µm. The blow-up indicates details of the refraction index of the water n_W, glass n_{glass}, and the BSA n_{BSA}.

Actually, the index of refraction can be estimated as 1.44 for the proteinaceous hydrogel. Due to this re-evaluation, the maximum transversal displacement of the focal spot in the structure is evaluated when the laser spot is focused at a distance |p| beyond the vertex of the built microstructure. This depends on the curvature radius with which the built microstructure can be approximated. As remarked, this is a qualitative estimate at least for two reasons: 1) the micro-structure is evaluated for the above-mentioned estimation as it is being cross-linked like

---

[1] BARER, R., & TKACZYK, S. (1954). Refractive Index of Concentrated Protein Solutions. *Nature, 173*(4409), 821-822.

a partially detached structure with a curved surface approximated to the section of a sphere and 2) this method of refractive index estimation avoids to compute the effect of the spherical aberrations that with such high NA beams are highly relevant. A part from these considerations, the transversal displacement corresponds always to a maginification M<1 that implies that the beam is partially trapped within the structure.

Bottom-case: In this situation as depicted in Figure 1. The refraction causes bending the laser beam inward, with respect to the microstructure printed plane. This analysis was followed by simulating the refraction of a laser beam focused by the objective through the glass slide and at the entrance of microstructure printing plane. As an assumption, the surface of the cross-linked microstructure that is formed on the glass slide is not perfectly flat in addition with a slight detachment from the glass slide at the edges. This situation was sketched as a mild curvature of the surface of the structure laying on the glass slide. The microstructure is then modeled as a parallelepiped with round surface on the laser entrance side of curvature radius *R*.
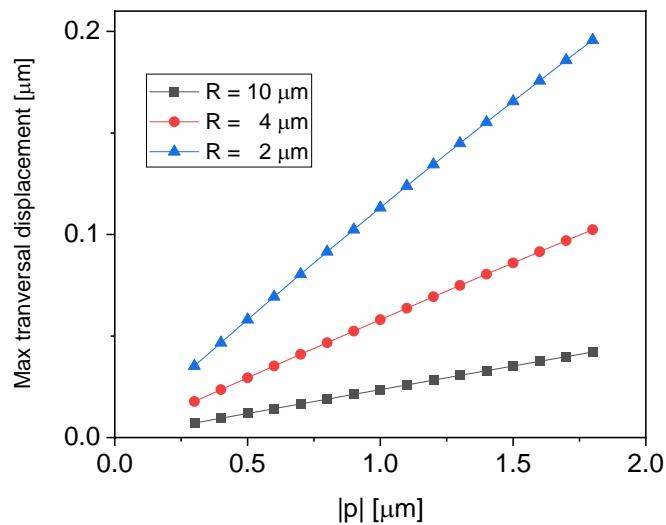

Figure 2. Depiction of focal spot transversal displacement over its distance |p| beyond the vertex in fabricated microstructure in three different approximated condition with curvature radius of R.

Through this simulation condition, the laser beam was focused at a point along with the optical axis that lies within the microstructure. The presence of the microstructure decreases the dioptric power of the system. Hence, when the laser beam is focused along the optical axis of microstructures, a shift farther from the glass slide can be observed, in comparison with the case that there is no beam-microstructure interaction. One can be understood from this simulation is that when the laser beam is moved out of the optical axis of the microstructure, the beam is refracted by the microstructure in a way that the focal spot bent inward the structure till at least half the beam is moved off from the printed medium, Figure 2. The

evaluation of the refractive index was estimated using a model in which the microstructure-glass slide surface is a single diopter with a curvature radius R. Regarding this assumption the dioptric power $\mathcal{P}$ of the curved surface of the microstructure is:

$$\mathcal{P} = \frac{(n_{BSA} - n_W)}{R} = \frac{\Delta n}{R} \tag{I-1}$$

While the conjugate planes equation can be written as below:

$$\mathcal{P} = \frac{n_{BSA}}{q} + \frac{n_W}{p} = \frac{n_{BSA}}{q} - \frac{n_W}{|p|} \tag{I-2}$$

The distances q and p are measured from the vertex of the dioptric (due to an assumption if the refraction angles are small). This is a limiting approximation for a quantitative estimate of the optical path but gives a qualitative understanding over the previous equation, if $p < 0$ (laser is focused beyond the dioptric surface). In the condition where the laser beam is focused inside the microstructure at the distance q^2, the transverse magnification is given by equation below:

$$M = 1 - \frac{q\mathcal{P}}{n_{BSA}} \tag{I-3}$$
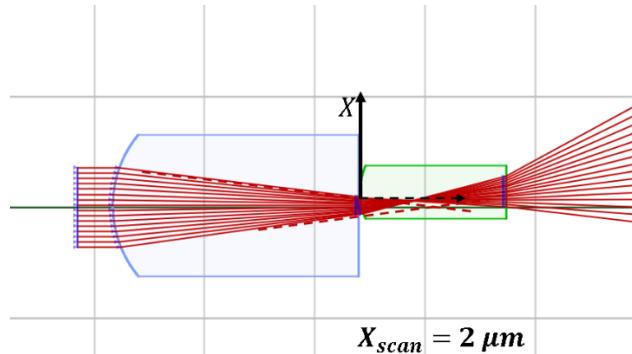

$$X_{scan} = 2\,\mu m$$

Figure 3. Sketch of one of the scanning positions. The laser spot should be scanned at position $X_{scan} = 2\mu m$, instead here is focused at the position $X_{eff} = 1.65\mu m$.

The transverse magnification is always positive for a laser focused within the microstructure and it is smaller than 1.

If X_{scan} is the position that the laser focal spot should have due to the scanning protocol, the actual position along the scanning axis can be approximately computed as $X_{eff} \cong M \cdot X_{scan}$ as long as the nominal position of the laser spot lies within the microstructure, at the point that

---

$^2\ q = \dfrac{n_{BSA}}{\mathcal{P} + \frac{n_W}{|p|}} = \dfrac{n_{BSA}}{\frac{n_W}{|p|} + \frac{\Delta n}{R}} = \dfrac{n_{BSA}}{\Delta n + \frac{n_W R}{|p|}} R$

the laser focal spot snap from X_{eff} to X_{scan}, making a jump of $\Delta X \cong M \cdot \frac{\Omega}{2}$, where Ω is the width of the microstructure along the scanning axis.
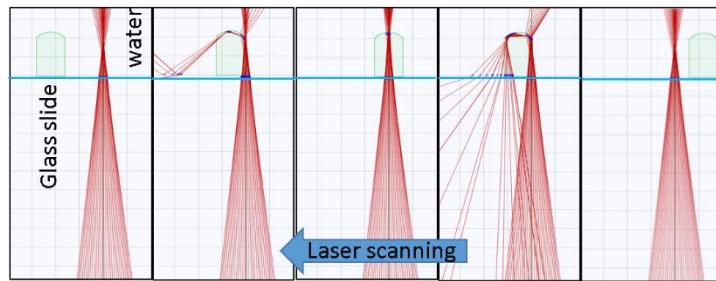

Figure 4. Refraction of the laser beam by the top-curved-surface during the scanning. Five different positions of the laser beam are depicted during the scanning of a printed structure and $R \cong 6\mu m$.

Top-case: In this condition, different behaviors was observed, depending on the curvature radius of the top surface of the microstructure. In the situation where the radius of curvature of the top-surface was sufficiently small, $R \cong 6\mu m$, the light is internally reflected in the microstructures when the laser is scanned in the most marginal region of the microstructure. Figure 3.

Appendix-II

Fluorescence Correlation Spectroscopy (FCS)

FCS is a correlation analysis method based on temporal fluctuations of fluorescence intensity of a sub-femtolitre sample volume for detecting characteristics like diffusion behavior and molecular concentrations. In the present study, FCS analysis was adapted to measure GNPs concentration in the stock solutions and as-prepared inks, in addition to the nanoparticle's proximate size evaluations.

Rhodamine 6G (Rhd6G) was used as the reference standard with diffusion coefficient of $D = 330\ \mu m^2/s$ at room temperature conditions. All the FCS related measurements were done on an inverted Nikon microscope using a Ti:Sapph as the laser source and Water-immersion objective (60X, N.A 1.2). The laser spot size after the objective (focal plane) was $\omega_0^2 = 0.19 \pm 0.02 \mu m^2$ that corresponds to $\omega_0 = 0.44 \pm 0.02 \mu m$. The correlation functions of the GNS are well-fitted by a two components diffusion with a triplet component with a decay of about 5µs, Figure 1.
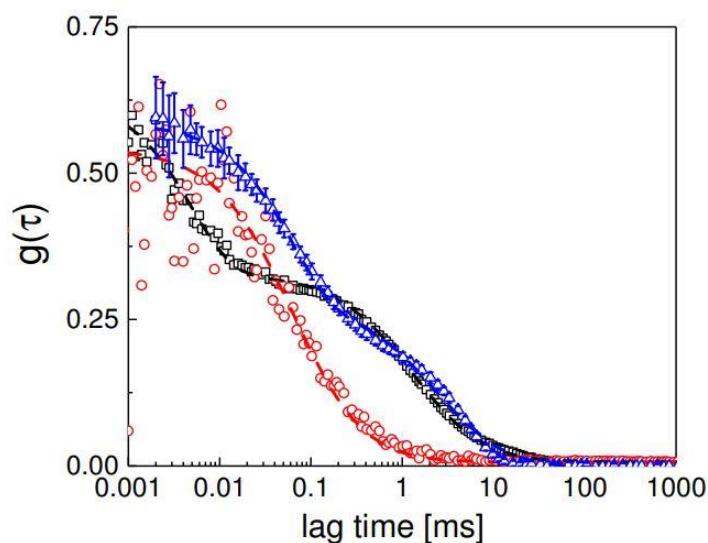

Figure 1. FCS functions collected from GNS solution (dilution 1:3, open black squares), GBNPs solution (dilution 1:10, open blue triangles), and 50nM Rhd6G solution in ethanol (red circles, data multiplied 50x) recorded with water-immersion objective.

For the water-immersion objective the overall value of the temporal auto-correlation function[1] $G(\tau)$ at time $\tau = 0$ was measured as $G(0) = 0.32 \pm 0.02$ that correspond to an average number $<N> = 0.24 \pm 0.02$ molecules. The data were taken with excitation wavelength at 800nm that

---

[1] $G(\tau) = \frac{<\delta I(t)\delta I(t+\tau)>}{<I(t)>^2} = \frac{<I(t)I(t+\tau)>}{<I(t)>^2} - 1$, where $\delta I(t) = I(t) - <I(t)>$ is the deviation from the mean intensity $I(t)$. The correlation at $\tau = 0$ is related to the average number of molecules in the focal volume.

resulted in a excitation volume of $0.74 \pm 0.07\mu m^3$ (from $V_{exc} = \frac{\pi\omega_0^4}{\lambda}$). From this behavior the concentration $C = \frac{<N>}{V_{exc}}$ of GNSs in the stock solution was evaluated around $C = 0.53 \pm 0.1$nM or 0.4 ± 0.1 particle per each μm^3 volume. These measurement then was completed by the calculation of the GNSs diffusion coefficient $D = 16 \pm 2$ μm^2/s that corresponds to a size (diameter) of $=26.5 \pm 3$nm.

In the case of GNSs, the shape is a planar, symmetric penta-twinned star as can be derived by the high resolution TEM images reported in [Pallavicini, 2013[2]] (in particular Fig.2C, D, E, herein). The arm's length is $L = 54 \pm 3\ nm$ and the length of the pentagon core side is $S = 12.6 \pm 1.3$ nm. The volume of this structure can be approximated by $V_{GNS} = S\frac{S}{2}(L + 0.688\,S) = 4700 \pm 700\ nm^3$. Then the number of gold atoms per nanoparticle can be estimated as $N_{Au} \cong V_{GNS}/V_{au}$. Being the gold atom volume approximately given by $V_{au} \cong 0.018\ nm^3$, the estimation gives $N_{Au} \cong 2.5 \times 10^5$ and a nanoparticle mass of $M_{GNS} \cong 50 \times 10^6\ uma$ that reveals the mass concentration of nanoparticles in suspension of $2.7 \times 10^{-5}\ g/mL$, or 0.003 % w/w. It is remarkable that with such low concentration of gold in the hydrogels the experiment can reach measurable photo-thermal effects.

For the GBNPs case, the fitting of the FCS auto-correlation function was collected from a ten times diluted stock, Figure 1. This dilution gave an intercept value of auto-correlation function $G(\tau)$ at $\tau = 0$ around $G(0) = 0.28 \pm 0.009$ in addition of a diffusion coefficient of $D = 10.8 \pm 0.4$ μm^2/s. In a short lag time measurements, the concentration of GBNPs evaluated as $= 6 \pm 2$nM or 3.6 ± 1 particles per each μm^3 volume that can be corresponded with particles of size (diameter) $=39.4 \pm 4$nm.

Specific absorption rate (SAR):

The rate of absorbed energy or the amount of absorbed non-ionized radiation power by unit mass of a sample defines as the SAR. In another word, the SAR is the rate of heat dissipation per unit of mass of photothermal nanoparticles.

During this study, in the approach of characterizing the photothermal effect arisen from GNS and GBNPs, as an alternative way, SAR measurements were done by mean of FCS analysis method. In order to evaluate the individual mass of the sample that displays the photothermal effect different concentrations of the stock solutions of GNSs and GBNPs were taken into account. For the GBNPs case, the overall shape can be approximately considered as a sphere

---

[2] Pallavicini, P; Dona, A.; Casu, A.; et al. Triton X-100 for three-plasmon gold nanostars with two photothermally active NIR (near IR) and SWIR (short-wavelength IR) channels. Chem. Commun. (2013) 49: 6265-6267

with many protrusions whose radius is the hydrodynamic radius, $R_H = 19.5 \pm 2nm$, and volume $V_{GBNP} = 31040 \pm 9000nm^3$ [1]. In the case of GNSs, the shape is planar like a symmetric pentawinned star. The arm's length can be estimated as $L = 54 \pm 3nm$ and the length of the pentagon core side is $S = 12.6 \pm 1.3nm$. From these data, the volume of the particle can be evaluated around $V_{GNS} = 4700 \pm 800nm^3$ [2]. The SAR for these two types of gold nanoparticles can be approximated as below [3]:

$$SAR = \frac{\mathcal{C}}{m_{NP}} \frac{dT}{dt} \qquad (\text{II-1})$$

Here, $\mathcal{C}$ is the solution heat capacity (here is assumed to be like the heat capacity of water). This equation can be re-written using the nanoparticles volume fraction φ that builds up from total number of irradiated nanoparticles/volume $N_{NP} = V n_{NP}$ ($V \cong 0.006cm^3$) and the related Mass under the same irradiation M_{NP} (here $\cong 19.3 \frac{gr}{cm^3} V$):

$$SAR \cong \mathcal{C} \frac{\Delta T}{\tau N_{NP} M_{NP}} \qquad (\text{II=2})$$

Table 1. Temperature increase ΔT measured on the bulk solutions of the gold nanoparticles under irradiation of a Ti:sapph laser.

	GNS	GBNP
τ[s]	1.1±0.1	1.5±0.1
<50mW>	12°C	9°C
<160mW>	21°C	18°C
M_{NP} [gr]	9.0x10⁻¹⁷	1.6x10⁻¹⁵
V [nm³]	4700±800	82400±4000
$n_{NP}[\frac{NP}{\mu m^3}]$	0.9±0.1	3.6±0.1

From the data listed in Table 1, the SAR estimations for GNSs and GBNPs under laser average power of $<P> = 160mW$ are:

$$SAR_{GNS} \cong 16kW/gr$$

$$SAR_{GBNP} \cong 0.8kW/gr$$

These calculations show the efficiency of photothermal effect of GNSs (approximately 20 times higher than GBNPs).